Development of Efficient Techniques for Fog Removal from Digital Images

THESIS SUBMITTED

FOR THE AWARD OF DEGREE OF

Doctor of Philosophy

BY

Isha Kansal

(Registration No. 901411006)

UNDER THE GUIDANCE OF

Dr. Singara Singh Kasana

Associate Professor

Computer Science and Engineering Department

Thapar Institute of Enginering and Technology

Patiala -147004, INDIA

June, 2020

Declaration

I hereby declare that the work being presented in this thesis entitled "Development of Efficient Techniques for Fog Removal from Digital Images", in fulfillment of the requirements for the award of degree of **DOCTOR OF PHILOSOPHY** submitted in Computer Science and Engineering Department, Thapar Institute of Engineering and Technology, Patiala, is an authentic record of my own work carried out under the supervision of Dr. Singara Singh Kasana, Associate Professor, Department of Computer Science and Engineering, Thapar Institute of Engineering and Technology, Patiala and refers other researcher works which are duly listed in the reference section. The matter presented in this thesis has not been submitted for the award of any other degree of this or any other University.

Isha Kansal

Registration No. 901411006

This is to certify that the above statement made by the candidate is correct and true to the best of my knowledge and belief.

Dr. Singara Singh Kasana

Associate Professor

Department of Computer Science and Engineering

Thapar Institute of Engineering and Technology

Patiala-147004, Punjab, India

Supervisor.

Acknowledgments

I owe to the grace of almighty, whose divine light provided me the perseverance, guidance enormous patience, inspiration, faith and strength to carry out this research work. I would like to express earnest gratitude to my supervisor, **Dr. Singara Singh Kasana**, Associate Professor, Computer Science and Engineering Department, Thapar Institute of Engineering and Technology, Patiala for his invaluable guidance and simulation throughout this research work, giving me constructive comments and support. I am extremely indebted to him for providing time to listen and give his valuable suggestions.

I express my sincere thanks to **Dr. Maninder Singh**, Head, Computer Science and Engineering Department, Thapar Institute of Engineering and Technology, Patiala for his support and suggestions. I am grateful to the Doctoral committee comprising **Dr. Sharad Saxena**, Associate Professor, Computer Science and Engineering Department, **Dr. Jhilik Bhattacharya**, Assistant Professor, Computer Science and Engineering Department and **Dr. Sanjay Sharma**, Professor, Deprtment of Electronics and Communication Engineering for monitoring the progress and providing valuable suggestions for the improvement of this work. I thank all the staff members of Computer Science and Engineering Department, Thapar Institute of Engineering and Technology for their support and cooperation.

Words are inadequate in paying regards to my father **Sh. Binder Pal Singla**, mother **Smt. Meena Singla**, brother **Achin Singla**, grand mother in law late **Smt. Kamla Devi**, father in law **Sh. Manmohan Kansal**, mother in law **Smt. Raj Rani Kansal**, sister in law **Mrs. Romila Gupta** and my friends **Mrs. Preeti Sharma** and **Mrs. Divya Seth** for their blessings, continuous encouragement and patience.

I also express deep gratitude to my new born child whose indirect support has been an invaluable source of encouragement to me.

It is impossible for me to quantify and express in words the constant help and moral support of my dear husband **Mr. Naveen Kansal**. His support and advice are pillars of strength not only in this work but at every stage of my life. I would like to express thanks to all who made their contribution directly or indirectly during this journey of research work to make my Ph. D., a successful event.

Isha Kansal

Isha Kansal

Abstract

With the increase in industrial production and human activities, the concentration of atmospheric particulate matter is substantial increased, leading to occurrence of fog and haze phenomenon. Due to these phenomenon, the visibility of scene gets reduced which is a major problem for many computer vision based applications. Hence, the scenes captured by computer vision systems called as images may suffer from poor visibility and low contrast. These make detection, tracking and recognition of objects within the images more difficult. Therefore visibility, contrast and features enhancement of images and videos captured in such a weather is an inevitable process called as fog removal or de-fogging process.

In the past decade, many de-fogging techniques have emerged out of which the model based single image de-fogging techniques are visually appealing and produce qualitatively good results. One of the well known model based de-fogging technique is Dark Channel Prior (DCP). Although, it works well on various image types but it has some limitations including longer execution time, non uniform illumination and dullness in de-fogged images. Since DCP may fail for non sky areas in the image, the next de-fogging technique under consideration is Color Attenuation Prior (CAP). DCP works on RGB model whereas CAP works on HSV. CAP uses a linear model for depth map estimation and learns the parameters of this model with a supervised learning method. Although, CAP technique performs well on different type of foggy images but it has some limitations too. CAP uses Guided filter for refining initial depth map which is a well known smoothing filter but it may not work well for fine edge details. Also, the images obtained by CAP technique suffer from dullness and higher illumination variations due to consideration of homogeneous environment and a constant value of atmospheric light. Generally, the image de-fogging techniques are based upon single window based depth map which may lead to produce color and edge distortion problems due to a constant window size. These limitations have been dealt in the proposed work as described below.

In this research work, three different restoration based image de-fogging techniques have been proposed based upon DCP and CAP approaches. The first image de-fogging technique is based on the atmospheric scattering model and DCP. To reduce the execution time of a DCP based de-fogging technique, a novel approach to sub-sample the image is proposed which preserves local minimums of the image. The technique estimates dark channel at significantly faster rate than that of existing dark channel while producing better visual de-fogging results. To reduce the effect of non uniform illumination in the environment, the global atmospheric light is calculated by

ignoring pixels of bright light sources by applying 3σ rule on luminance channel Y of YUV color space. This improves the over darkness problem in the final de-fogged images. To make the de-fogging results look uniformly bright, post processing is applied on the de-fogged images. In the next technique, to estimate the transmission map, fast Gradient Domain Guided image Filtering ($GDGF$) is applied on CAP based initial depth map. The edge attentive restraints of $GDGF$ make edges to be conserved better in the de-fogged images. The illumination variations occurred during CAP based de-fogging are reduced in the proposed work by using Lambert's law of illumination reflection, which helps to compensate non uniform illumination, causes simultaneous dynamic range modification, color consistency, and lightness rendition without producing any artifacts in de-fogged images. The third de-fogging technique is based upon fusion of dark channels with two different windows. Existing fusion based de-fogging techniques use Discrete Wavelet Transform (DWT) which prevents repetitions and allows to use the same filter pairs in different scales, but it has two main limitations including the shift invariance and low directional selectivity. The fusion in this work is performed by using DCP and Dual Tree Complex Wavelet Transform ($DTCWT$). $DTCWT$ overcomes the above two limitations of DWT which enhances the edge details in the final recovered image and maintains the color and naturalness in the de-fogged images. A combined color channel transmission map is used to identify under exposed (low contrast) regions in the de-fogged image and an adaptive technique is used to enhance such regions without making any color distortion.

Since the utility of a de-fogging process lies in real time processing, the minimum preserving sub-sampling based de-fogging technique is further extended to foggy videos as this technique obtains acceptable results for almost all image types and has low computational time. For video de-fogging, a scene change detection algorithm is used to simultaneously manage the temporal coherence, spatial coherence and the computational cost. Experimental results show that the proposed video de-fogging technique obtains satisfactory results in maintaining spatial as well as temporal coherence.

Contents

List of Publications

- Isha Kansal and Singara Singh Kasana, "Weighted image de-fogging using luminance dark prior", Journal of Modern Optics, Vol. 64, No. 19, pp. 2023-2034, 2017, Impact Factor = 1.269.
- Isha Kansal and Singara Singh Kasana, "Minimum Preserving subsampling based fast image de-fogging", Journal of Modern Optics, Vol. 65, No. 18, pp. 2103–2123, 2018, Impact Factor = 1.269.
- Isha Kansal and Singara Singh Kasana, "Fusion based Image De-fogging using Dual Tree Complex Wavelet Transform", International Journal of Wavelets, Multiresolution and Information Processing, Vol. 16, No. 6, pp. 1850054 (1-27), 2018, Impact Factor = 0.540.
- Isha Kansal and Singara Singh Kasana, "Improved De-fogging Technique based upon Colour Attenuation Prior", Multimedia Tools and Applications, Vol. 79, pp. 12069-12091, 2020, Impact Factor=2.101.

List of Abbreviations

BPDFHE	Brightness Preserving Dynamic Fuzzy Histogram Equalization
CAP	Color Attenuation Prior
CI	Colorfulness Index
CIE	Color Information Entropy
CLAHE	Contrast Limited Adaptive Histogram Equalization
CNI	Color Naturalness Index
DCP	Dark Channel Prior
DOG	Difference of Gaussian
DTCWT	Dual Tree Complex Wavelet Transform
DWT	Discrete Wavelet Transform
FADE	Fog Aware Density Evaluator
FMRF	Factorial Markov Random Field
FRF	Fog Reduction Factor
FRIDA	Foggy Road Image Database
GDGF	Gradient Domain Guided Filter
GF	Guided Filter
GHE	Global Histogram Equalization
HE	Histogram Equalization
HH	High High
HL	High Low
HP	High Pass Component

LH	Low High
LHE	Local Histogram Equalization
LL	Low Low
LP	Low Pass Component
MRF	Markov Random Field
MSR	Multi Scale Retinex
MSRCR	Multi Scale Retinex with Color Restoration
NIR	Near Infrared
POSHE	Partially Overlapped Subblock histogram Equalization
SCD	Scene Change Detection
SSR	Single Scale Retinex
RGB	Red Green Blue
RMSE	Root Mean Square Error
RF	Random Forest
VCM	Visual Contrast Measurement
VL	Visible Light
WLS	Weighted Least Square

List of Symbols and Notations

$a_x,\ b_x$	Constants of a Guided Filter
A	Airlight Component of Fog Image Degradation Model
C_n^d	Normalized Combined Color Channel darkness parameter
d	Depth Map of a Foggy Image
G	Gaussian Function
I	Foggy Image
I^{dark}	Dark Channel of a Foggy Image
I_{ds}	Minimum Preserving Down Sampled Image corresponding to I
I_{ds}^{dark}	Dark Channel Image Corresponding to I_{ds}
I_g	Guidance Image used in Guided Filter
I^{min}	Minimum Color Channel of a Foggy Image
k	Normality Parameter
l	Surface Shading Function
L	Luminance Component
L_A	Global Atmospheric Light
L_0	De-fogged Image
M	Rows of a given Image
N	Columns of a given Image
p	Degree of Polarization
p'	Restoration Degree of Tarel's Technique
r	Average Gradient

Rf	Reflection Component
s_b	Number of blocks
S	Saturation Component
t	Transmission Map
t'	Refined Transmission Map
V	Brightness Component
β	Medium Scattering Coefficient
ϵ	Regularization Parameter of Guided Filter
ϵ_0	Error in Linear Model of CAP
ω	Square Window in Guided Filter
ω'	Constant of Dark channel based De-fogging
Ω	Square Window
Π	Square Window of Guided Filter
ρ	Scene Albedo
σ	Variance
σ_G	Gaussian Parameter
$\theta_0,\ \theta_1,\ \theta_2$	Constants of CAP Model

List of Figures

List of Tables

Chapter 1

Introduction

1.1 Image De-fogging

Intelligent image and video surveillance based applications have been widely used in todays world due to their accuracy and less human intervention. There has been a growing demand on vision-based smart applications such as video indexing [7], face recognition [11], object tracking [12], people re-identification [13], behavior analysis [75] *etc*. These intelligent applications assist human beings to monitor specific vision based fields in more persuasive and efficient ways. However, these applications always face some fundamental problems due to changing backgrounds and extreme weather. In these applications, generally the segmentation of objects present in an image is required. This segmentation becomes difficult and unreliable in foggy weather conditions. Also, for the images taken in weathers, such as foggy weather, not only the visual quality is affected, but the accuracy of vision-based techniques is also influenced. The atmosphere contains suspended particles and water droplets which adversely affects the quality and visibility of outdoor images due to absorption and scattering caused by those particles. The light reflected from an object is being partly absorbed and scattered before it reaches to the camera. Farther is the object from camera, more light is being absorbed and scattered. The images and videos taken in foggy conditions are usually degraded and always have low contrast and poor color fidelity. These degraded videos not only produce poor visualizations, but also make further vision-based analysis, such as foreground/background segmentation, tracking and behavior analysis *etc.* more difficult.

Unlike other traditional image degradation, fog is a natural, depth-dependent perturbation that spans non-uniformly over the whole image. The degradation and the loss of information increases with increasing depth, as the amount of fog between the imaged surface and the sensor increases. Hazy and foggy images have also different prevailing colors, which depend on the density of the scattering particles and the ambient light. Due to recent progress in vision based computer applications, it has become possible to improvise the images taken in an outdoor environment. Foggy images can get benefit from such computer vision based techniques referred to as de-fogging techniques. Such techniques are based upon established theories from aerology and other disciplinarians.

De-fogging techniques are used to improve the visual quality of the images and videos captured in foggy climate. The intend is to produce better visualization along with improving correctness of the higher level video analysis. It is possible to improve the visibility of foggy scenes in terms of range, color and feature separation in digital images. In this thesis, the term de-fogging means to recover the fog degraded scene image in terms of color, contrast, naturalness and visibility which can be seen in Figure 1.1. A de-fogging technique can greatly improve the image visibility for the better scene information understanding. It allows the observer to get a much higher situational awareness. Such visibility improvements may lead to a smoother and faster work flow in areas where operators need to observe a wide area under every possible weather conditions at day and night, such as an air traffic controller at an airfield, possibly at a tower or a remote position, respectively. The term de-hazing also

(a) Foggy Image (b) De-fogged Image

Figure 1.1: The effect of image de-fogging

represents this work since the effects of haze and fog are similar to some degree. They work upon the same model and the transition between these two phenomena is gradual. The research in de-fogging field aims at improving visibility of the image scene and recovering colors in such a way that the image looks like it has been taken in clear weather conditions. These improved images can then be used by Computer and human vision based processes for different applications *e.g.* object detection and long range video surveillance *etc.*

In recent years, much work has been done on de-fogging techniques by utilizing different kinds of computer hardware. This work is a great source of motivation for the betterment of research in de-fogging area. Although, this work has provided the researchers a number of de-fogging techniques for various types of foggy images taken during different environments and times of day. These techniques still suffer from poor vision in heavy fog regions. Since, the main utility of image de-fogging techniques is in real time applications, due to their high time complexity, they are seldom applied in surveillance videos. In such type of applications, there is a need to have faster and effective de-fogging techniques. So there is still a scope of improvement in the de-fogging field by incorporating other challenges which may come in the future.

The demand for image de-fogging techniques comes from the fact that environment contains suspended particles which degrades the visibility of the scene and hence images. Even in the neat air, the range of vision is between 277-348 km [44] not including the earth's curvature. Yet, the real range of vision is smaller than this an-

alytical value. For extremely clear air, the vision range is rated between 50m-50km by the international visibility code for meteorology. The exact codes are given in Table 1.1 [20].

Table 1.1: International Visibility Code with Meteorological Range

Code No.	**Weather Condition**	**Meteorological Range**	**Scattering coefficient (β)**
0	Dense Fog	50m	> 78.2
1	Thick Fog	50m-200m	78.2 - 19.6
2	Moderate Fog	200m-500m	19.6-7.82
3	Light Fog	500m-1000m	7.82 - 3.91
4	Thin Fog	1lm-2km	3.91 - 1.96
5	Haze	2km-4km	1.96 - 0.954
6	Light Haze	4km-10km	0.954 - 0.391
7	Clear	10km-20km	0.391 - 0.196
8	Very Clear	20km-50km	0.196 - 0.078
9	Exceptionally Clear	$>$50km	0.078
-	Pure Air	277km	0.0141

In Table 1.1, β represents the medium scattering coefficient which is the most important parameter to describe visual range. These codes were found to reflect a convenient scale for visual ranges in the daily work of meteorologists. The term visibility in this context is synonymous to visual range, which is a subjective measurement and varies from person to person. Visual range is defined as the range to where a reference object is just discriminable from the background.

In the beginning of the 19^{th} century, scientists like Mie and Koschmieder built the theories that are still used in the field of meteorology and computer vision. Mie expanded the theory of scattering of Rayleigh by examining larger particles such as haze aerosols [83]. It proved to be a great influence in scattering and extinction of light in the atmosphere. Koschmieder took an essential step by studying the scattering theories of Rayleigh. He developed an holistic theory of visibility for horizontal visual ranges through the atmosphere. Based upon environmental illumination, the composition of air in the scene of interest, this theory describes the visibility of a distant object. Much of the research on visibility theories was done during the first and second world wars. Visibility range in various altitudes of the atmosphere, as well as the development of chemical warfare methods that were intended to reduce visibility for hostile airplane pilots were the subjects of meteorological research at that time. Nevertheless, the work from that time is the basis for what we know about optics of the atmosphere today.

1.2 Basics of the Atmosphere

When the light travels through a medium, it interacts with the particles present in that medium and generally gets altered. The mechanisms including scattering, absorption and reflection may take place depending upon properties of the medium. Because of such mechanisms, it is believed that, though a particular medium, light can't travel undistorted ceaselessly. To explain, how the light gets altered by the atmospheric particles, the constitution of atmosphere needs to be understood. In this section, the broader overview of the atmospheric composition is given. Here, in this section, the atmospheric conditions generated in foggy weather are considered.

1.2.1 Composition of Air

Visibility generally depends upon the type of atmospheric particles, their distribution and size. In the normal case, atmosphere only contains the pure air which consists of molecules with $10^4 \mu m$ radius and 10^{19} per cm^3 concentration. The air in the atmosphere is considered useful in breathing and other plant activities such as photosynthesis. The dry air mainly consists of nitrogen which is 78.09%. The other main constituent of air is oxygen which is 20.95%. The other gases are argon, which is 0.93%, carbon dioxide, 0.033%, *etc*. Apart from these gases, water vapors are also present in the air. Although, the composition of ozone and water vapors in the air are very less, but due to their good absorption of ultraviolet and infrared rays, they play a valuable role in the atmospheric optics [77].

The atmosphere acts as the earth's envelope which is hundreds of kilometers thick. The optical properties, therefore vary with the altitude. So, in this thesis, the altitude of interest is restricted to Troposphere *i.e.*, the atmospheric layer exactly above the ground which is needed for the application of image de-fogging. The phenomenon of fog occurs due to scattering and absorption of light by the particles present in the atmosphere. All types of particles which cause atmospheric scattering are shown in Table 1.2. Haze particle, fog droplet and cloud droplets are the strong light scatterers. The larger sized particles scatter light more effectively which are mainly fog/haze particles and water droplets.

Table 1.2: Particles involved in Atmospheric Scattering

Type	**Size** (μm)	**Concentration** (cm^{-3})
Air Molecule	10^{-4}	10^{19}
Aitken nucleus	$10^{-3} - 10^{-2}$	$10^2 - 10^4$
Haze particle	$10^{-2} - 1$	$10 - 10^3$
Fog droplet	$1 - 10$	$10 - 100$
Cloud Droplet	$1 - 10$	$10 - 300$
Raindrop	$10^2 - 10^4$	$10^{-5} - 10^{-2}$

1.2.2 Optical Model of Light Scattering

Haze is a common atmospheric process emerging from the sources of air pollution such as dust, smoke and other atmospheric particles which obscure the transparency of sky. Fog (or mist) is the other phenomenon which is caused by water or ice droplets hanging in the air close to the earth's surface. From Figure 1.2 (a) it is shown that,

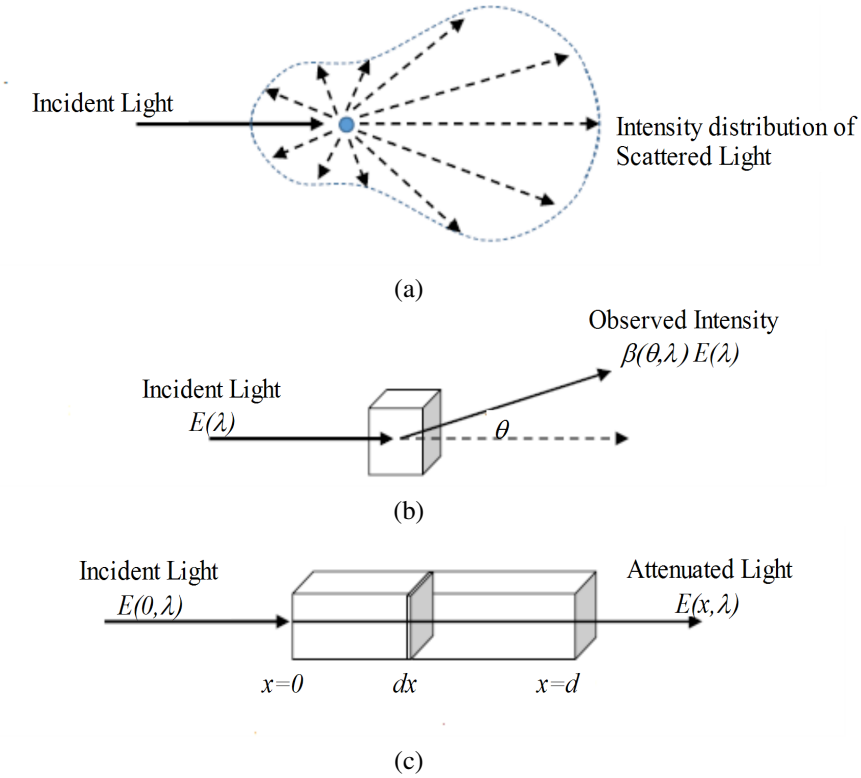

Figure 1.2: (a) Single particle scattering, (b) Unit volume scattering and (c) Light attenuation over distance raised by scattering [71].

when a light ray strikes on an atmospheric particle, it scatters that light ray to all the directions having weightiness relying upon on its wavelength (λ), shape and the size. The scattered rays move away from the striking particles are also called as outbound rays whereas the rays striking a particle from all the directions are inbound rays. The analytical connection between inbound light E_l and outbound light I can be shown in (1.1) and Figure 1.2 (b) by considering each particle as an independent entity.

$$I(\theta, \lambda) = E_l(\lambda) \times \beta(\theta, \lambda) \tag{1.1}$$

$\beta(\theta, \lambda)$ is called the angular scattering coefficient and

If it is being assumed that a particle medium consisting of a hunk having dx as its thickness and a parallel ray of light passing through each sheet as shown in Figure 1.2 (c), then the irradiance change at x can be represented as:

$$\frac{dE_l(x, \lambda)}{E_l(x, \lambda)} = -\beta(\lambda) \times dx \tag{1.2}$$

By performing integration of (1.2) from $x = 0$ to $x = d$, and for non parallel light rays, the equation becomes:

$$E_l(d, \lambda) = \frac{I_0(\lambda) \times e^{-\beta(\lambda) \times d}}{d^2} \tag{1.3}$$

I_0 is intensity of the source.

I_0 is assumed to be a point source [77]. For overcast sky illumination, (1.3) can be written as:

$$E_l(d, \lambda) = \frac{g \times L_A(\lambda) \times \rho(\lambda) \times e^{-\beta(\lambda) \times d}}{d^2} \tag{1.4}$$

L_A is intensity of the light at horizon,

ρ is the scene point reflection and

g is the camera gain. Apart from the light reflected by the objects or from any other source, there is also an

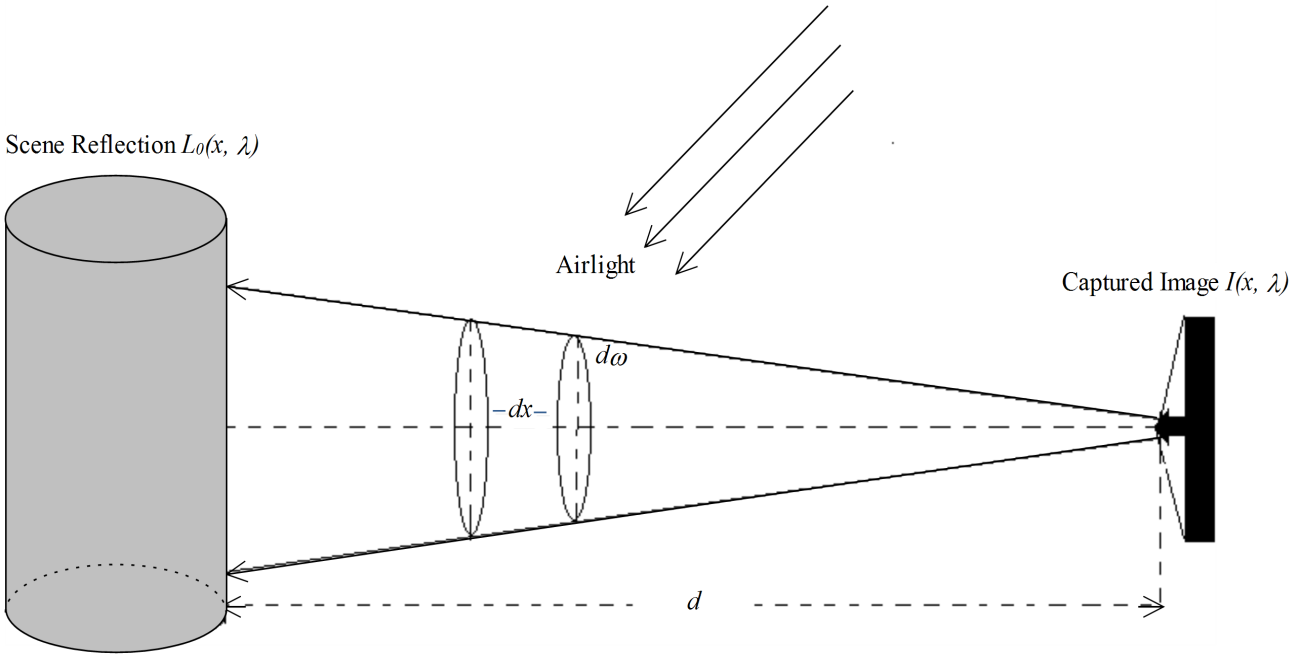

Figure 1.3: Imagery Model

atmospheric lightening scattered towards the camera by environmental particles. This lightening is generally due to lightening of the Sun, sky and the atmospheric light reflected from the ground. This type of scattered light observed during hazy environment is also referred to as airlight as shown in Figure 1.3. Following (**??**) and (1.2), we have:

$$dI(x, \lambda) = \kappa \times \beta(\lambda) \times dV \tag{1.5}$$

$dV = d\omega \times x^2$ is a volume in the cone of perspective,

$\kappa \times \beta(\lambda)$ represents the total scattering coefficient

κ is a constant. The light source dI passes through small particles and the outgoing light is represented by using:

$$dE(x,\lambda) = \frac{dI(x,\lambda) \times e^{-\beta(\lambda)\times d}}{x^2} \tag{1.6}$$

where x^2 is due to the inverse square law of non parallel light rays. So, total L at d from camera can be estimated by integrating $dL = \frac{dE}{d\omega}$ as:

$$L(d,\lambda) = L_A \times (1 - e^{-\beta(\lambda)\times d}) \tag{1.7}$$

By combining the direct transmission (1.4) and airlight (1.7) [83], the light scattered by the atmospheric particles which is captured by the camera can be represented as:

$$I(x) = L \times \rho(x) \times e^{-\beta\times d(x)} + L_A \times (1 - e^{-\beta\times d(x)}) \tag{1.8}$$

$I(x)$ represents the intensity of an image at location x. L_A is the global atmospheric light assumed to be independent from x. The term L represents the combined effect of global atmospheric light, camera gain and d, and is represented as: $L = L_A \times \frac{g}{d^2}$. β denotes the medium scattering coefficient. $L \times \rho$ is the intensity of an object in a clear atmosphere. d represents the distance between an observer and the object. In this thesis, the reflection of clear day scene is represented as:

$$L_0(x) = L \times \rho(x) \tag{1.9}$$

L_0 estimation is the goal of a de-fogging technique, as it represents the value of scene point not affected by the particles present in the medium. The airlight $A(x)$ and the transmission $t(x)$ at x are given by:

$$A(x) = L_A \times (1 - e^{-\beta\times d(x)}), \qquad t(x) = e^{-\beta\times d(x)} \tag{1.10}$$

1.2.3 Optical Scattering Model in relation to Foggy Image Recovery

The model is based upon the assumption that atmosphere is homogeneous and the fog particles are uniformly distributed. The model can also be represented as:

$$I(x) = L_0(x) \times t(x) + L_A \times (1 - t(x)) \tag{1.11}$$

t is called as transmission map or transparency of the fog.

$t(x)$ is a scalar value in the range [0, 1]. $t(x) = 0$ represents completely foggy pixel, $t(x) = 1$ represents completely clear pixel and $0 < t(x) < 1$ represents partially foggy pixel. The vision of an object on a clear day is based on air which acts as the transparent medium through which the light reflected by the object is perceived by the observer without any alteration. In the hazy or foggy environment, small droplets of water are suspended

in the atmosphere. These particles present in the air cause the image point to be diminished and whitish due to scattering of light present in the atmosphere and the net radiance perceived by the observer is called as the direct transmission part as shown in Figure 1.4. Due to the distance from the camera to the scene point, the radiance of the actual scene point gets reduced. In addition to this, the water particles also become light source as the natural light present in the atmosphere is scattered by them. This scattered light is perceived by the observer in addition to direct transmission of the scene point and causes the actual scene point to be more bright and whitish which is called as airlight part as shown in Figure 1.4. These two parts *i.e.* transmission and airlight simultaneously reflects the foggy image.

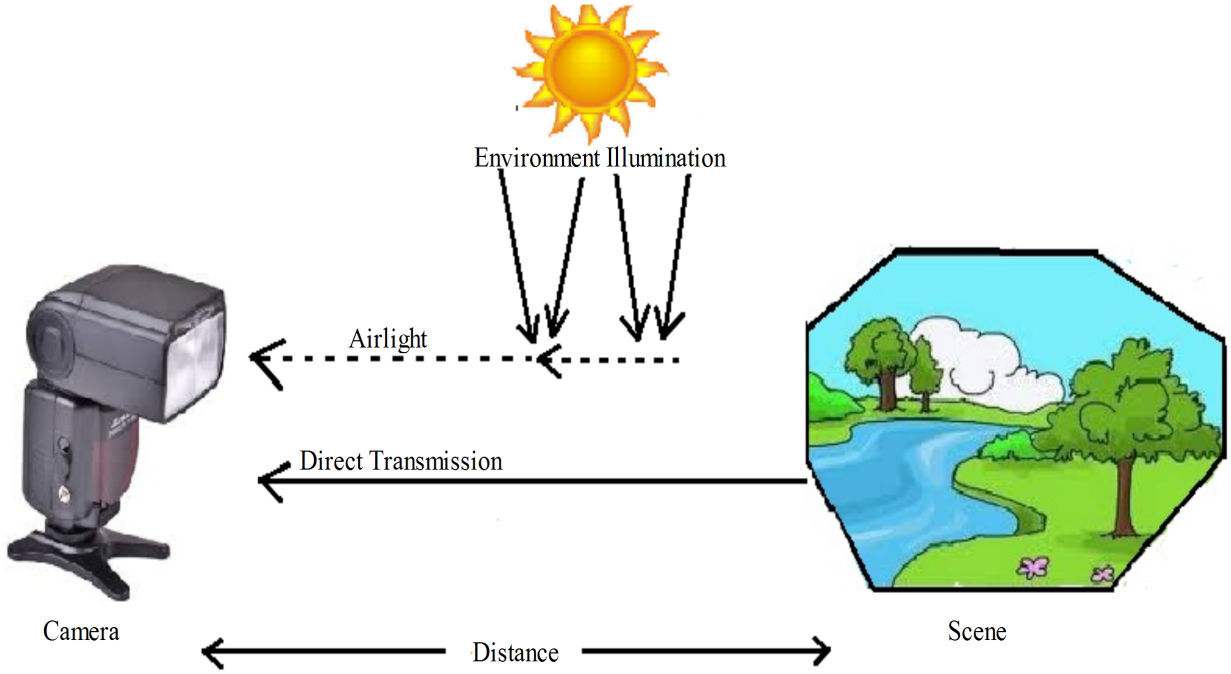

Figure 1.4: Scattering of Atmospheric Light

1.3 Image De-fogging Techniques

In this Chapter, image de-fogging techniques are broadly classified into two categories. One is image enhancement based de-fogging techniques and another is image restoration based de-fogging techniques. Image de-fogging techniques belonging to first category are based upon image enhancement. They do not follow the physical fog image degradation model (1.11) for foggy image recovery. The techniques based upon image enhancement include([2], [89], [91], [101], [130]). The techniques belonging to this category do not consider the variation of fog with scene depth and hence obtains unreliable de-fogging results.

Techniques belonging to second category are based upon physical model ([8], [23], [29], [42], [66], [80], [85], [114]). These techniques find the parameters of the physical model (1.11) which include the transmission and atmospheric light. Transmission is inversely related to scene depth whereas atmospheric light depends upon scene

brightness. The de-fogged images can be restored by putting the values of parameters in the physical model (1.11). The images obtained by techniques of this category look natural and clear. They achieve good visibility and also maintain better color restoration. Different image enhancement and restoration based de-fogging techniques are used to improve the visibility and contrast of a given foggy image, as explained in further sub-sections.

1.4 Image Enhancement based De-fogging Techniques

In this section, various fog removal techniques are discussed which are based upon several image enhancement techniques. These techniques aim to improve the color, contrast and brightness of a degraded image and are widely used in the field of image de-fogging, underwater image enhancement and medical image enhancement.

1.4.1 Techniques based upon Retinex Image Processing

The term Retinex is formed from two words "retina" and "cortex", which signifies human visual perception. The theory of Retinex has been widely used in the field of night image enhancement, image dehazing, image de-fogging, dark image enhancement and non uniform illumination image enhancement *etc.* ([49], [98], [99], [135]). Edwin Land [67] first proposed the theory of Retinex based on color constancy. According to the Retinex theory, an image is made up of two components, *i.e.* the incident (L) and the reflection (R) component. The luminance information of an image is revealed by the incident component which is also called as the luminance image. The inner information of an image is given by the reflection component which is also called as the reflection image. In Figure 1.5, the Retinex image formation model is shown. According to the Retinex theory, an image pixel $I(x, y)$ is represented by:

$$I(x, y) = L(x, y) \times R(x, y) \tag{1.12}$$

Rf is the reflection component,

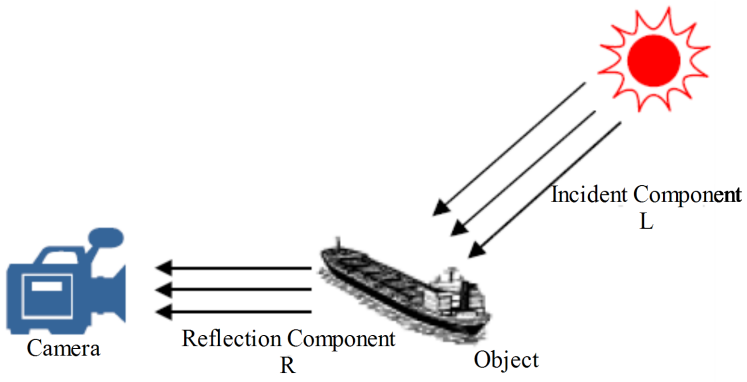

Figure 1.5: Retinex Image formation Model

L is the incident component and

$(x,\ y)$ are coordinates of an image pixel.

An image I is the pixel by pixel product of the luminance component and the scene reflectance according to (1.12). The Retinex technique deals with problem of separating the two quantities: first estimating the illumination information and then obtaining the reflectance by division. For solving the above model, natural logarithm (log) is applied to (1.12) on both sides.

$$log(I(x,y)) = log(L(x,y)) + log(Rf(x,y)) \tag{1.13}$$

If the luminance component L is found, the reflection component Rf can be obtained by using (1.12). Therefore, the luminance component mainly determines the effectiveness of an image de-fogging technique. In early studies, to estimate the luminance component, the random path-based technique [68], the passion equation based iteration technique, and the multiple-scale technique based on the Difference-of-Gaussian (DOG) operator were proposed.

1.4.2 Image De-fogging Techniques based upon Traditional Contrast Enhancement

Image enhancement techniques have been widely used in many applications of image processing where the subjective quality of images is important for human interpretation. Contrast is an important factor in any subjective evaluation of image quality. Foggy images are generally considered as low contrast images. The image de-fogging techniques based upon the traditional image contrast enhancement applied in the field of image de-fogging are discussed in this section. These techniques include intensity transforms, homomorphic filtering, high-boost filtering, and wavelet transform *etc.*

1.4.2.1 Intensity Transform based Image De-fogging

The histogram of a fog degraded image is generally distributed towards center as most of its pixels have larger intensity values. Therefore, the foggy images are considered as low contrast images. Intensity transforms are a simple and effective way to enhance such images by redistributing their histograms [31]. The typical intensity transform techniques include power-law gamma transformation, piecewise-linear transformation and Histogram Equalization (HE).

1.4.2.2 Wavelet Transformation based Image De-fogging

Discrete Wavelet Transform (DWT) is the most popular transformation technique adopted for image enhancement. The advantage of DWT is that, it acquires both frequency and time information. It decomposes a signal into four different sub-bands namely Low-Low (LL), Low-High (LH), High-Low (HL) and High-High (HH). The LL sub-band contains the coarse approximation of the source image and three high pass sub-bands express image details across different directions *i.e.* HL for horizontal details, LH for vertical details and HH for diagonal details of an image. The techniques based upon wavelet transform enhance a fog degraded image by raising the high frequency component while reducing its low frequency component [21]. By using wavelet transform,

better enhanced images can be obtained. The noise can also be reduced in the high frequency sub-bands.

1.4.2.3 Miscellaneous Techniques

Generally, the high-frequency components of an image are associated with the image edge details and the low-frequency components represent the smooth area of an image. In the physical degradation model, airlight is the main low-frequency component. The edge information of a foggy image is usually degraded due to fog. Generally, due to fog, the high-frequency components of an image are decreased while the low-frequency components are increased. Therefore, if the high-frequency components of a foggy image are increased while the low-frequency components are weakened, its visibility can be enhanced. This type of techniques include Homomorphic filtering, High-boost filtering and fusion based de-fogging.

1.5 Restoration based Image De-fogging Techniques

McCartney proposed the physical model of atmospheric scattering by using Mie scattering theory. This model is composed of two different components *i.e.* the airlight and direct transmission model. The direct transmission component signifies that the light from an object is attenuated due to atmospheric scattering. Due to this, the degradation of edge details and texture information of an object in an image occurs. In the airlight component, some of the sunlight and diffused sky light is also scattered by the atmosphere and gets transmitted to the camera. Such lights are not the lights from the actual scene objects and these can be considered as the fog component of an image. Its influence is similar to that of a veiling light which hides the objects in the image and makes them look whitish. In a clear image, the direct transmission component plays a major role in the imaging model because of insignificant scattering of atmospheric light. As the concentration of fog increases, the direct transmission component's effect is decreased whereas the the airlight component's effect gets increased and in turn reduces the visibility of an image. The airlight component is the main reason which causes the image acquired in foggy weather to look like a low contrast and poor visibility image. In the following subsections, the restoration based de-fogging techniques are further classified as multiple image based de-fogging techniques and single image based de-fogging techniques [127].

1.5.1 Multiple Images based De-fogging Techniques

In general, multiple images of the same scene always contain more information than that of a single image as one image may compensate some detailed knowledge that another one missed. In such type of image de-fogging techniques, two or more images of the same scene are captured through camera. The information from multiple images is then utilized to de-fog a given image. The multiple image based de-fogging techniques are further divided into two categories. The techniques belonging to first category use multiple foggy images captured under the same weather condition. Whereas, the techniques of second category use multiple images of the same scene

captured in different weather conditions.

1.5.1.1 Multiple Images of same Weather based De-fogging

Since the airlight scattered by atmospheric particles is partially polarized, some image de-fogging techniques were proposed which used multiple polarization images. Treibitz *et al.* [116] demonstrated the fact that by using the two polarization images of the same scene reduces the noise in the results of image restoration. The polarization filter is used in different orientations to obtain the images of the same scene with different brightnesses levels. To estimate the parameters of physical image restoration model (1.11), such type of techniques make use of at least two polarization images and then obtain a fog free image by inversely solving the physical model for image restoration. Schechner *et al.* [106] proposed an image restoration technique by using two polarization images of the same scene. Those two images are taken at parallel and perpendicular orientations respectively. The image de-fogging techniques based upon polarization images assume that the direct transmission component is not affected by the degree of orientation. The polarization images are obtained by using:

$$I^{\perp} = \frac{F(x)}{2} + A^{\perp}(x) \tag{1.14}$$

$$I^{\parallel} = \frac{F(x)}{2} + A^{\parallel}(x) \tag{1.15}$$

$F(x) = L_0(x) \times t(x)$ represents the component of direct transmission,
$A^{\perp}$ and $A^{\parallel}$ are the respective airlights of the parallel and perpendicular polarization images and are:

$$A^{\perp}(x) = L_A^{\perp} \times (1 - t(x)) \tag{1.16}$$

$$A^{\parallel}(x) = L_A^{\parallel} \times (1 - t(x)) \tag{1.17}$$

Here $L_A^{\perp}$ and $L_A^{\parallel}$ are the atmospheric light values of the two parallel and perpendicular polarization images and can be estimated from the sky area. The degree of polarization (p) is

$$p \equiv \frac{A^{\perp} - A^{\parallel}}{A^{\perp} + A^{\parallel}} \tag{1.18}$$

In the polarization based de-fogging, atmospheric light L_A of each polarization image is the key parameter for estimating restored image L_0. The degree of polarization can be estimated by two atmospheric light values of the polarization images as

$$\hat{p} = \frac{L_A^{\perp} - L_A^{\parallel}}{L_A^{\perp} + L_A^{\parallel}} \tag{1.19}$$

Then the airlight and transmission can be estimated using:

$$A(x) = \frac{A^{\perp}(x) - A^{\parallel}(x)}{\hat{p}} \tag{1.20}$$

$$t(x) = 1 - \frac{A(x)}{L_A^{\perp} + L_A^{\parallel}} \tag{1.21}$$

Therefore, the de-fogged image can be retrieved by using the transmission map t and airlight $A(x)$ by inversely solving the physical restoration model (1.11).

1.5.1.2 Multiple Images of different Weather based De-fogging

In multiple images of different weather based image de-fogging techniques, the de-fogging is done by using two or more than two images of a scene captured during different weather conditions. Narasimhan *et al.* studied the effect of using multiple images captured under different weather conditions ([81], [82], [83], [84], [85], [86]) for carrying out the process of image de-fogging.

1.5.2 Single Image based De-fogging Techniques

In this section, the techniques which acquire the information from a single foggy image to carry out the image de-fogging process have been discussed. As compared to image de-fogging techniques which use multiple images, single image de-fogging techniques are proved to be more advantages as they are more automated and require least human intervention. As discussed in previous sections, transmission t and atmospheric light value L_A are the key parameters to solve the physical image degradation model (1.11). The techniques discussed in this section calculate these two parameters based upon different conditions/assumptions and hence obtain de-fogged images by inversely solving physical model. Various de-fogging techniques belonging to this category are described as follows.

1.5.2.1 Surface Shading based Image De-fogging

On the basis of an assumption that surface shading and transmission are locally uncorrelated, Fattal [23] proposed a technique for obtaining transmission and global atmospheric light as:

$$l^{-1}(x) = \frac{1 - \frac{I_A(x)}{||L_A||}}{I_{R'}(x)} + \frac{\eta}{||L_A||} \tag{1.22}$$

$$t(x) = 1 - I_A(x) - \eta \times \frac{I_{R'}(x)}{L_A} \tag{1.23}$$

$l(x)$ represents the function for surface shading and

$t(x)$ is the function for transmission.

I_A and $I_{R'}$ are estimated as follows:

$$I_A(x) = \frac{\langle I(x), L_A \rangle}{||L_A||}, \quad I_{R'}(x) = \sqrt{||I(x)||^2 - I_A^2(x)} \tag{1.24}$$

Here $\langle , \rangle$ denotes the standard $3D$ dot product in the RGB color space. Fattal found L_A from the sky region, η by using the assumption that surface shading and transmission are statistically uncorrelated over a certain area χ, which implies that $Cv_\chi(l^{-1}, t) = 0$. Function Cv_χ is the sample covariance. Therefore, η can be estimated by using $Cv_\chi(l^{-1}, t) = 0$:

$$\eta(x) = \frac{Cv_\chi(I_A(x), h(x))}{Cv_\chi(I_{R'}(x), h(x))}, \quad h(x) = \frac{||L_A|| - I_A(x)}{I_{R'}(x)} \tag{1.25}$$

After finding the values of $t(x)$ and L_A, the estimation of the scene reflection, $R(x)$ can be eventually obtained.

1.5.2.2 Local Contrast Maximization based Image De-fogging

Tan *et al.* [112] proposed single image de-fogging technique based upon two observations. First, the clear day images generally have higher contrast than that of foggy day images. Second, the airlight changes smoothly in a small local area. Tan's technique finds L_A from the brightest pixels of a foggy image. The image I is normalized to $\tilde{I}$ by dividing it with element wise chromaticity of L_A. The visibility enhancement problem can be solved if we know the scalar value of the airlight A for every pixel:

$$e^{-\beta \times d(x)} = \frac{\sum_c L_A^c - A(x)}{\sum_c L_A^c} \tag{1.26}$$

$$\tilde{R}(x) = \left(\tilde{I}(x) - A(x) \times \begin{bmatrix} 1 \\ 1 \\ 1 \end{bmatrix} \right) e^{\beta \times d(x)}, \tag{1.27}$$

c denotes one of the RGB channels and

$\tilde{R}$ is normalized component corresponding to R.

The values of A range from 0 to $\sum_c L_A^c$. The main concept behind this de-fogging technique is to obtain $A(x)$ in order to maximize local contrast $Contrast$ of $\tilde{R}(x)$ as:

$$Contrast(\tilde{R}(x)) = \sum_{x,c}^{S} | \bigtriangledown \tilde{R}_c(x)| \tag{1.28}$$

S is a square window of size 5×5.

Tan [112] casted this propblem into a Markov Random Field (MRF) framework and estimated the airlight values for the entire input image. This technique obtains good results for color, gray and thick foggy images

1.5.2.3 *DCP* based Image De-fogging

He *et al.* [33] proposed an image de-fogging technique called as Dark Channel Prior (DCP) technique which has been proved very effective in restoring outdoor foggy images. He *et al.* examined large amount of clear day outdoor images and found that in most areas of a clear outdoor image (except for the sky area and white area), there is a channel of pixels with the minimum value of zero. This channel is called as dark channel which is calculated for any given image L_0 as:

$$L_0^{dark}(x) = min_{c \in R,G,B}(min_{y \in \Omega(x)} L_0^c(y)) \tag{1.29}$$

where Ω denotes a square window centered at pixel x and
$R,\ G\ and\ B$ are the red, green, and blue components of an image respectively.

According to the DCP theory, for a clear day image, except for the sky and white areas, $L_0^{dark} \approxeq 0$. This theory was used to estimate the transmission map t for image restoration by applying the following min operation in the local area on (1.11) as:

$$min_{c \in \{R,G,B\}}((min_{y \in \Omega(x)}(\frac{I^c(x)}{L_A})) = min_{c \in \{R,G,B\}}((min_{y \in \Omega(x)}(\frac{L_0^c(x)}{L_A})) \times t(x) + (1 - t(x)) \tag{1.30}$$

In terms of (1.29) and (1.30), coarse transmission $\tilde{t}$ is

$$\tilde{t}(x) = 1 - \omega' \times min_{y \in \Omega(x)}(min_{c \in \{R,G,B\}}(\frac{I^c(x)}{L_A})) \tag{1.31}$$

or

$$\tilde{t}(x) = 1 - \omega' \times (\frac{I^c(x)}{L_A})^{dark}$$

Since the minimum filtering operation is applied in the local area of a foggy image, the dark channel image contains block or halo artifacts. This will make the restored image L_0 contain block artifacts as well. In order to solve this problem, the original DCP de-fogging technique used a soft matting operation to optimize and smoothen the coarse transmission map to obtain t. The atmospheric light value L_A was also obtained by using the theory of DCP. He *et al.* [33] selected top 0.1% brightest pixels from dark channel and then chose the pixel with the highest intensity in the original foggy image as atmospheric light L_A. Finally, the de-fogged image L_0 is obtained as:

$$L_0^c(x) = L_A^c + \frac{I^c(x) - L_A^c}{max(t(x), t_0)} \tag{1.32}$$

here t denotes the optimized transmission map obtained after applying soft matting,
t_0 is a small constant, *i.e.* $0 < t_0 < 1$ used to prevent the denominator to become zero.

1.5.2.4 Bayesian Image De-fogging

Kratz and Nishino [65], [88] proposed a single image Bayesian de-fogging technique on the basis of the fact that scene albedo ρ and depth d are two statistically autonomous components. The image is factorized into the scene albedo and depth as

$$ln(1 - \frac{I(x)}{L_A}) = ln(\rho(x) - 1) - \beta \times d(x) \tag{1.33}$$

$\hat{I}(x) = ln(1 - \frac{I(x)}{L_A}),\ C(x) = ln(\rho(x) - 1)$ and
$D(x) = -\beta \times d(x)$
$C(x)$ and $D(x)$ can be seen as the scene albedo and depth respectively.

Then a Factorial Markov Random Field ($FMRF$) was applied to model the dependence between these two items and the input image

$$P(C, D|\hat{I}) \propto P(\hat{I}|C, D) \times P(C) \times P(D) \tag{1.34}$$

Here P denotes the posterior probability. The image coordinates are dropped because the probabilities are computed over the entire image. C and D are estimated by maximizing (1.34). The de-fogged image is then found by inversely solving the physical image degradation model (1.11).

1.5.2.5 Machine Learning based Image De-fogging

In recent years, machine learning based field has emerged with promising performance in image processing applications. Some of the researchers have combined physical degradation model with machine learning models to find the parameters of degradation model for image de-fogging. In such techniques, author collects a large number of outdoor fog-free colored images, carries out fogging simulation and obtains the vector feature library of foggy images through training and evaluation. Tang *et al.* [113] proposed a novel transmission estimation technique using a learning-based approach. For image patches, Random Forest Model was used to learn the regression model which finds the relation between haze-relevant characteristics and their true transmission. The unknown foggy image is initially divided into small patches and fog relevant features are extracted. The learned Random Forest (RF) model is then used to find the transmission of each image patch. Finally, the coarse transmission map for a complete foggy image is found by combining the transmission of each image patch.

Zhu *et al.* [136] found the fact that saturation and brightness of a foggy image change strongly with changing fog concentration. In general, the concentration of fog increases with increasing scene depth. By assuming that the scene depth is positively correlated with fog concentration, Zhu *et al.* proposed a linear model to estimate the parameters of a fog degradation model for foggy image recovery. Consider the equation:

$$d(x) = \theta_0 + \theta_1 \times V(x) + \theta_2 \times S(x) + \epsilon_0(x) \tag{1.35}$$

Here x represents the image coordinates, d denotes the image scene depth at x, V represents the scene brightness

and S denotes the saturation, θ_0, θ_1 and θ_2 are the linear coefficients, $\epsilon_0(x)$ denotes the random error of this model (1.35). This model is called as Color Attenuation Prior (CAP). One of the main importance of this model is its edge preservation nature. According to Zhu *et al.* [136], ϵ_0 tends to be very low and hence the CAP model preserves the gradient of image. To accurately learn $\theta_0,\ \theta_1\ and\ \theta_2$ coefficients, training data is required. This training data consists of foggy images and their associated ground truth depths. But it is hard to obtain the real depth maps. Therefore, inspired from Tang *et al.'s* technique, synthetic depth maps and foggy images are generated from clear images taken from Google and Flicker. For training the linear model, 500 training samples having 120 million scene points were collected. Having 517 epochs, the best learning results are obtained for $\theta_0 = 0.121779$, $\theta_1 = 0.959710$, $\theta_2 = -0.780245$ and $\sigma^2 = 0.041337$. These parameters are then used for estimating depth map by using (1.35). This depth estimated may fail for some cases like white objects. For such objects, the brightness values are usually high and the saturation values are low. Therefore, it will consider white objects as the distant objects. So, the raw depth map d_r is obtained by applying local minimum operation on initial depth map as:

$$d_r(x) = min_{y \in \Omega(x)} d(y), \tag{1.36}$$

Here $\Omega(x)$ denotes the square window centered at x. y is the minimum value pixel in the local window $\Omega(x)$. d_r is the window based depth map. However, due to patch wise local minimum operations, this depth map generates halo artifacts. To remove these halo artifacts, Zhu *et al.* applied guided filter to estimate final depth map d.

After estimating the scene depth map d, the global atmospheric light L_A, the transmission map t is estimated according to (1.11). Finally, the scene radiance L_0 is recovered by using (1.11) as

$$L_0^c(x) = L_A^c + \frac{I^c(x) - L_A^c}{min\{max\{e^{-\beta \times d_{ref}(x)}, 0.1\}, 0.9\}} \tag{1.37}$$

The values for t are restricted between 0.1 and 0.9. A small value of β generates smaller transmission values and hence final de-fogging results look still foggy in the distant regions. Whereas, a large β causes overestimation of the transmission. Therefore, Zhu *et al.* took a moderate value of $\beta = 1.0$.

1.6 Video De-fogging Techniques

A digital video is the term used to describe any sequence of time varying images. A still image is a spatial distribution of intensities that remain constant with time while a time varying image has a spatial intensity distribution that varies with time. Video de-fogging covers most of the image de-fogging techniques, but also includes some extra steps due to the temporal nature of video data. In most real-world applications, such as for scene surveillance and visual systems of an unmanned plane or vehicle, the real-time visibility of the video acquired by the visual system needs to be enhanced. In contrast to various image de-fogging techniques, only a few techniques were proposed for enhancing the visibility of a video sequence in a foggy weather. In addition, most video de-fogging techniques

were proposed for video surveillance with the same background image. But, many techniques were proposed for video enhancement and video denoising. Although, the image de-fogging techniques have good performance in the visibility enhancement of fog degraded images, but in some real-world applications, such as scene surveillance and visual systems of an unmanned plane or vehicle, the real time visibility of the video acquired by the visual system needs to be enhanced. In these situations, such a technique is required which enhances the quality of the scene along with providing high processing speed. Video de-fogging techniques can be divided into following three categories as shown below:

(i) **Frame based Video De-fogging:** The first category is the frame based video de-fogging techniques which performs the single image de-fogging individually on each frame of a video. The parameters of restoration model (1.11) are estimated for each foggy video frame and the corresponding de-fogged frame is then obtained. This process takes long execution time which is not good in real time processing. Also, frame by frame processing often results in increased visual flicker among adjacent video frames which degrades the overall visual quality of a video.

(ii) **Fusion based Video De-fogging:** The second category is the fusion based video de-fogging techniques which are based upon the fusion of enhanced background and foreground images of each video frame. Fusion-based de-fogging techniques first extract the background and foreground of each frame. Then the single image de-fogging is used to separately enhance the background and foreground image. Finally, video de-fogging can be realized by fusing the enhanced background and foreground images of each frame.

(iii) **Universal Component based Video De-fogging:** The third category of the video de-fogging techniques are the universal component-based de-fogging techniques which are based on the estimation of a universal component that can be used in all video frames. Universal component-based video de-fogging techniques try to estimate a universal component which represents the fog distribution and apply it to subsequent frames of the video. These video de-fogging techniques are reasonable and able to improve the efficiency.

1.7 Quality Parameters

(i) **Average Gradient:** Average Gradient (r) utilizes the gradients of visible edges in the de-fogged image to depict the restoration degree of edge and texture information of the image [38]. r is described as follows:

$$r = e^{[\frac{1}{n_I}\sum_{i\in\phi_I} log(r_i)]} \tag{1.38}$$

here $r_i = \frac{\delta I}{\delta L_0}$,

δI and δL_0 are the gradients of foggy and the de-fogged images respectively.

Larger value of r indicates that the corresponding de-fogging technique has improved the capacity of edge preservation.

(ii) **Color Naturalness Index:** Color Naturalness Index (CNI) is the degree of correspondence between human perception and reality world, and its value lies between [0, 1] [41]. Higher value of CNI indicates that a de-fogged image is more natural. To find CNI for a given RGB image, first, its luminance (L), hue (H) and saturation (S) components are computed. Then, L and S are limited by using a threshold. Next, a pixel will be classified into the three classes, namely, skin, sky and grass based on the hue values. In particular, the hue values of 25-70, 95-135 and 185-260 are for skin, grass and sky pixels respectively. Let $nskin$, $ngrass$ and $nsky$ be numbers of pixels, for the above three classes. For each class, the averaged values and standard deviation of the saturation are estimated. The $S_{average}$ skin, $S_{average}$ grass and $S_{average}$ sky are the averaged saturation values for skin, grass and sky pixels respectively. By assuming the normal distribution, the local naturalness index for skin, grass and sky are computed as:

$$N_{skin} = exp[-\frac{1}{2}(\frac{S_{average_{skin}} - 0.76}{0.52})^2] \tag{1.39}$$

$$N_{grass} = exp[-\frac{1}{2}(\frac{S_{average_{grass}} - 0.81}{0.53})^2] \tag{1.40}$$

$$N_{sky} = exp[-\frac{1}{2}(\frac{S_{average_{sky}} - 0.30}{0.13})^2] \tag{1.41}$$

Finally, the global CNI value is obtained as

$$CNI = \frac{n_{skin} \times N_{skin} + n_{grass} \times N_{grass} + n_{sky} \times N_{sky}}{n_{skin} + n_{grass} + n_{sky}} \tag{1.42}$$

(iii) **Fog Reduction Factor:** Fog Reduction Factor (FRF) represents the difference between fog density value of a foggy image (I) and the de-fogged image (L_0). Fog density is measured using Fog Aware Density Evaluator ($FADE$) [18] and it represents the density of fog in an image. This fog density is estimated on the basis of natural scene statistics like local mean, contrast, sharpness, image entropy, dark channel, color saturation and colorfulness value. Larger value of the parameter FRF indicates better performance of a de-fogging technique. FRF is calculated as

$$FRF = FADE(I) - FADE(L_0) \tag{1.43}$$

(iv) **Visual Contrast Measurement:** Visual Contrast Measurement (VCM) quantifies the visibility strength of a given image [52] and is calculated by

$$VCM = 100 \times \frac{K_v}{K_t} \tag{1.44}$$

Here K_t is the total number of local areas and K_v represents the number of local areas having standard deviation larger than that of a given threshold. $OTSU$ threshold image segmentation algorithm [90] has

been used to calculate the threshold. VCM uses the local standard deviations and denotes an image contrast to measure the visibility. In general, higher value of VCM represents a clearer image.

(v) **CI:** Colorfulness Index (CI) is used to evaluate the color quality of a de-fogged image [9]. The colorfulness index uses a simple opponent color space as:

$$rg(x) = R(x) - G(x), \quad yb(x) = \frac{1}{2}(R(x) + G(x) - B(x)) \tag{1.45}$$

CI for an image is given by:

$$CI = \sigma_{rgyb} + 0.3 \times \mu_{rgyb}, \quad \sigma_{rgyb} = \sqrt{\sigma_{rg}^2 + \sigma_{yb}^2}, \quad \sqrt{\mu_{rg}^2 + \mu_{yb}^2} \tag{1.46}$$

σ is the standard deviation and μ is the mean of the pixels included in the image. An increased value of CI signifies a greater visibility which is larger in de-fogged images as compared to foggy ones and thus indicates better performance of a de-fogging technique.

(vi) **Color Information Entropy:** Color Information Entropy (CIE) is a statistical measure of randomness used to characterize the texture of an input image by using the histogram of an image of all R, G and B color channels [9]. CIE represents the amount of information in a color image. Its maximum value is attained when an image is clearer. In case of a foggy image, the value is smaller. CIE is mathematically defined as:

$$CIE = -\sum_{k=0}^{L-1} P_k \times log_2(P_k) \tag{1.47}$$

Here L is the number of gray levels, P_k is the probability associated with gray level k. Since a foggy image contains less texture information as compared to a de-fogged image and hence the CIE value will be greater for a de-fogged image comparatively.

(vii) **Execution Time:** Execution Time (t) is the total time taken by a technique required to produce a final de-fogged image (L_0) from a foggy image (I). The image de-fogging techniques are mostly used in real time applications such as video surveillance systems and intelligent vehicles *etc.* Therefore, the execution time taken by a de-fogging technique is a considerable issue. A de-fogging technique is considered better overall if it provides good visual results in lesser amount of time. The execution time of a given de-fogging technique is measured in seconds in this thesis.

1.8 Aim of the Work

The images captured by the computer vision systems in the foggy or hazy weather may suffer from poor visibility, low contrast, dimmed brightness, low luminance and distorted color. These make detection of objects within the image scene more difficult. Therefore, fog removal is a challenging task due to the inherent ambiguity between the

fog and the underlying scene. Model based single image de-fogging techniques are physically sound and produce qualitatively good results, however, more attentions to de-fogging quality rather than the applicability leads to for real-time applications they may not always be fast enough, besides, there exist limitations such as color-bias and unable to deal with the sky area, *etc*. Therefore, aim of the work is to review various existing image and video de-fogging techniques and analyze their shortcomings. The another main intend is to develop efficient image and video de-fogging techniques which can work in different kinds of environments with varying amount of fog and overcome the problems of existing de-fogging techniques.

1.9 Contribution of the Thesis

This thesis provides the introduction to foggy images, their formation and the particles involved in the formation process. Then the thesis introduces fog image degradation model and highlights various existing de-fogging techniques and their related issues. In order to solve those issues, in this thesis various de-fogging techniques have been proposed. The main contribution of the thesis are:

In this thesis, a novel approach to subsample the image is proposed, which preserves the value of local minimum in a patch. The subsampled image is further used to construct the dark channel for transmission estimation. The proposed technique is approximately 15 times faster DCP technique while producing better quality de-fogging results. The initial dark channel based transmission is refined with the help of fast guided filter instead of guided filter to further improve the computational efficiency. Global atmospheric light value is found from the dark channel image of top 25% rows by filtering the pixels belonging to bright light sources *e.g* train headlights, street lights *etc*. The de-fogged image is generally recovered by using single atmospheric light and due to dark channel based de-fogging, the de-fogging results may suffer from over darkness problem. Therefore to avoid over darkness, a post processing is performed on the de-fogging results with the concept of combined color channel transmission effect.

The next de-fogging technique is based upon CAP theory. CAP technique is based on local linear model and applies machine learning to find the parameters of linear model. The initial depth map is obtained by CAP model in the proposed technique and is refined with the help of fast gradient domain guided image filter which preserves edges better than that of existing CAP technique and also improves its computational efficiency. To avoid dullness problem in the de-fogged images obtained by CAP technique, non uniform illumination compensation is performed on the resultant images using the concept of Lambert beer's law and bright channel prior.

Third technique is developed on the basis of DCP theory and Dual Tree Complex Wavelet Transform ($DTCWT$). Transmission map is obtained by fusing wavelet sub-bands of dark channels with two different patch sizes. Due to use of multiple patches of dark channel, the color and edge distortion can be avoided. The wavelet used for fusion is $DTCWT$ which ensures the perfect reconstruction of image details in the transmission map due to its shift invariance property. This technique improves the image edge details and hence obtains high contrast de-fogged

images.

Further, the minimum preserving subsampling based image de-fogging technique is extended to foggy videos. First video frame is extracted and considered as a reference frame. Global atmospheric light and transmission are obtained by using the reference frame and the same frame is recovered by using fog degradation model. For further frames, the histogram based correlation is checked between upcoming and the reference frames. If they are correlated, the previous values of atmospheric light and transmission are used to de-fog upcoming frames, otherwise, both the parameters are estimated for the upcoming frame and then the reference frame is updated. This maintains the spatial and temporal coherence in the videos and also improves the computational complexity.

1.10 Significance of the Proposed Image and Video De-fogging Techniques

De-fogging plays an essential role in many vision based applications. In this thesis, image/video de-fogging techniques have been proposed which overcome the problems in existing de-fogging techniques. Existing techniques generally consider the atmospheric light- a global constant for entire image or a video frame whereas in the case of image which contains one or more light sources other than the natural light present in the atmosphere, the concept of global atmospheric light does not work well and de-fogged image is not of a good visual quality. In the proposed work, the portions of an image containing bright light sources have been filtered prior to atmospheric light estimation. Due to this, the over darkness problem in the de-fogged image can be avoided. The post processing step of the proposed de-fogging techniques improve the de-fogging performance in the case of evening time foggy images also. The computational cost of de-fogging is significantly reduced in the proposed work by applying minimum/maximum preserving subsampling for depth map estimation.

The proposed minimum preserving subsampling based image de-fogging technique is extended to video de-fogging in such a way that it maintains the spatial and temporal coherence in the resulting videos and further improves the computational complexity. Therefore this technique can be applied in real time applications.

.

Chapter 2

Literature Survey

2.1 Introduction to Image De-fogging Techniques

This Chapter provides the comprehensive survey of work done in the area of image/video de-fogging and highlights various existing techniques. Existing image de-fogging techniques are broadly classified into two categories as shown in Figure 2.1. One is image enhancement based de-fogging techniques and another is image restoration based de-fogging techniques. Techniques belonging to first category are based upon image enhancement ([2], [89], [91], [101], [130]). They do not follow the physical fog image degradation model for foggy image recovery. The other category is based upon physical model ([8], [23], [29], [42], [66], [80], [85], [114]). Finally, the gaps in the literature survey, objectives of the thesis and methodology used for proposed image/video de-fogging have been summarized.

2.2 Image Enhancement based De-fogging Techniques

Image enhancement techniques mainly aim to improve interpretability or perception of information in images for human viewers and provide better input for other automated image processing techniques. They are widely used in the field of underwater image enhancement, medical image enhancement and image de-fogging *etc*. The principal objective of image enhancement is to modify attributes of an image to make it more suitable for a given task and a specific observer. During this process, one or more attributes of the image are modified.0 The choice of attributes and the way they are modified are specific to a given task. The de-fogging techniques in this category are further divided into retinex and contrast enhancement based de-fogging techniques as explained in the following subsections.

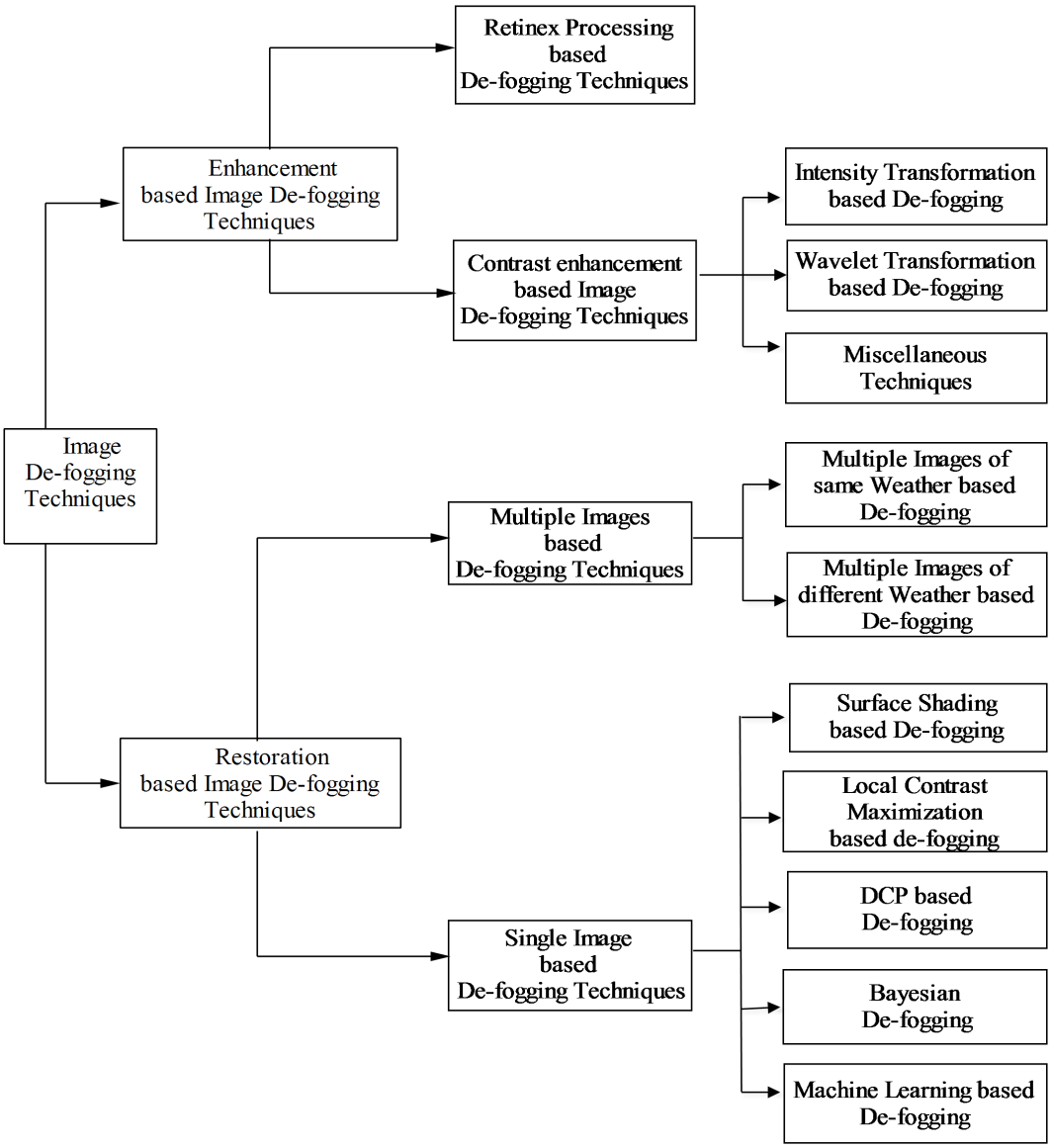

Figure 2.1: The categories of image de-fogging techniques

2.2.1 Techniques based upon Retinex Image Processing

Edwin Land [67] first proposed the theory of Retinex based on color constancy, according to which an image is made up of two components, *i.e.* incident (luminance) and reflection components. A de-fogging technique based upon Retinex theory obtains the reflection image by solving the Retinex model. If the luminance component L is found in such type of techniques, the reflection component R can be obtained by using (1.12). Therefore, the estimation of luminance component mainly determines the effectiveness of an image de-fogging technique. In early studies, to estimate the luminance component, the random path based technique [68], the passion equation based iteration technique, and the multiple-scale technique based on the DOG operator were proposed. Hurlbert *et al.* [45] summarized the above estimation techniques of the incident component. McCann *et al.* [76] proposed two Retinex techniques based on multi resolution pyramid which include the McCann99 Retinex and the Frankle-

McCann Retinex techniques.

For image enhancement, the goal of Retinex technique is the simultaneous accomplishment of the dynamic range compression, color constancy and color/lightness rendition [50]. The above stated techniques are very complex and do not achieve good performance in color constancy. Since the Gaussian function has good performance over a wide range of space constants, Jobson *et al.* [50], [48] proposed a technique to use the Gaussian function for estimating the luminance component. This technique is also called as single Scale Retinex (SSR) technique, in which the incident or luminance component is estimated as:

$$L(x,y) = I(x,y) * G(x,y) \tag{2.1}$$

$*$ represents the convolution operation,
$G(x,y)$ is a Gaussian function which can be expressed as $G(x,y) = k \times e^{-\frac{x^2+y^2}{\sigma_G^2}}$,
σ_G is the scaling parameter of the Gaussian function and
k is a normalizing factor which is used to ensure $\int\int G(x,y)d(x)d(y) = 1$.

For a RGB image, the reflection image is achieved by using

$$r_i(x,y) = log(I_i(x,y)) - log(I_i(x,y) * G(x,y)) \tag{2.2}$$

here $r_i(x,y) = log(Rf(x,y)),\ i \in R,G,B$ is one of three channels of a RGB image.

In the SSR technique, the image enhancement effect is decided by the scaling parameter σ_G. A larger value of σ_G preserves good color/lightness rendition in the recovered image, but the restored image details are not good. Otherwise, the opposite effect is obtained. In short, SSR technique cannot simultaneously attain dynamic range compression and color/lightness rendition. In order to overcome this shortcoming, Multiscale Retinex (MSR) and Multiscale Retinex with color restoration ($MSRCR$) techniques were proposed ([49], [50], [51], [97]). In MSR technique, three normalized Gaussian filters with different scales in each channel are applied. It is basically the weighted sum of the outputs of three SSR techniques having different scales as

$$r_i(x,y) = \sum_{j=1}^{3} Wt_j[log(I_i(x,y)) - log(I_i(x,y) * G_j(x,y)] \tag{2.3}$$

Wt_j denotes the weight of each scale.

All the three weights in MSR technique are equal to $\frac{1}{3}$. For most images, three scales of Gaussian function are fixed to $15,\ 80$ and 250 [51]. Finally, a gain/offset algorithm is used to adjust the obtained reflection image into the display domain *i.e.* [0, 255]. MSR technique achieves the advantages of image detail enhancement, small scale dynamic range compression and big scale color balance. On the other hand, MSR technique does not attain

a good color restoration effect. For solving this issue, $MSRCR$ technique added a color restoration step as

$$r_i(x,y) = Cf_i(x,y) \times \sum_{j=1}^{3} Wt_j[logI_i(x,y) - log(I_i(x,y) * G_j(x,y)] \tag{2.4}$$

Cf_i is the color restoration function.

Once the reflection image is obtained by (2.4), the final output image needs to be modeled into the display domain. Moore *et al.* [54] proposed an automatic normalization based technique to handle the output of techniques based on Retinex theory. Jobson *et al.* [51] proposed a canonical gain/offset technique to transfer the output of the Retinex technique into display domain. Petro *et al.* [94] examined Retinex based techniques such as SSR, MSR, and $MSRCR$ and figured out the fact that in these techniques, color restoration function was at risk of inverting colors. Therefore, they proposed a color restoration technique which was applied to the intensity channel.

Since, the fog is a low-frequency component of a foggy image, to enhance such an image, Wang *et al.* [118] used the wavelet transform. Then the SSR technique was used to improve the brightness of a de-fogged image. Zhao *et al.* [134] used the non linear sigmoid function in place of logarithm function used in MSR technique for foggy image recovery.

To estimate the luminance component, Gaussian filtering is used in the original SSR, MSR, and $MSRCR$ techniques. Since the Gaussian filtering does not preserve edges which causes edge degradation in the enhanced images. To solve this issue, Hu *et al.* [40] estimated the luminance component by using Bilateral filter. After this, Gamma adjustment and sigmoid functions were used for further enhancement of the estimated reflection component. Yang *et al.* [122] proposed a de-fogging technique based on variable filter Retinex technique. In this technique, for each local region of a foggy image, scaling parameters were selected adaptively. This technique improves the visibility and enhances the local contrast of a foggy image greatly.

2.2.2 Image De-fogging Techniques based upon Traditional Contrast Enhancement

Contrast is an important factor in any subjective evaluation of image quality. Foggy images are generally considered as low contrast images. The image de-fogging techniques in this category include intensity transforms, homomorphic filtering, high-boost filtering and wavelet transform *etc.*

2.2.2.1 Histogram based image De-fogging

Intensity transforms are a simple and effective way to enhance foggy images by redistributing their histograms [31]. The typical intensity transform techniques include power-law gamma transformation, piecewise-linear transformation and Histogram Equalization (HE). The transform is usually applied in the last step so as to improve the brightness of the enhanced image. Gao *et al.* [26] applied it to each channel of the enhanced image obtained by the MSR technique. Ma *et al.* [135] applied it on the enhanced image obtained by the SSR technique to further improve the quality.

HE technique is of two types: Global Histogram Equalization (GHE) and Local Histogram Equalization (LHE) [58]. GHE technique is used to enhance the global contrast of a degraded image, but it ignores the contrast of the local areas. The foggy images having inhomogeneous fog cannot be improved well by using GHE. This technique generates the halo artifacts in the areas of depth discontinuities. Therefore, Jun and Rong [103] initially applied GHE to enhance the foggy image. After that, the wavelet transform was used to decrease halo artifacts and noise. Opposite to GHE, LHE techniques are used to improve local contrast of a degraded image ([57], [58], [59]). Kim [58] proposed a partially overlapped sub-block histogram equalization ($POSHE$) technique. It performs GHE initially on each sub-block of an image and then applies a weighted fusion technique to the overlapped pixels. In addition to contrast enhancement, this technique also reduces the blocking artifacts. To enhance the fog degraded images and to maintain their color fidelity, Ramya *et al.* [100] proposed a brightness preserving dynamic fuzzy histogram equalization ($BPDFHE$) technique.

The contrast limited adaptive histogram equalization ($CLAHE$) [137] was proposed to reduce the noise generated by HE. Xu *et al.* [126] applied $CLAHE$ on the intensity component of the HIS space of a foggy image. These simple techniques related to HE fails when the image contains depth variations and also in the case of inhomogeneous fog. However, for some foggy images with dense fog, the visibility of the enhanced image obtained by HE based technique is better than that of other, such as the Retinex-based techniques.

2.2.2.2 Wavelet Transformation based Image De-fogging

The techniques based upon wavelet transform enhance a fog degraded image by raising the high frequency component while reducing its low frequency component [21]. Busch *et al.* [15] proposed a de-fogging technique for a traffic control system based upon wavelet transform. Jia and Yue [47] first decomposed the luminance component of YUV space by using wavelet transform. The airlight was removed from the low frequency subbands by applying Gaussian filtering. The high pass filter was applied to enhance the image details. Finally, by using the inverse wavelet transform, the de-fogged image was obtained. Rong *et al.* [103] applied unsharp masking technique on the low frequency component of a degraded image to improve the contrast.

The de-fogging techniques based upon wavelet perform well in reducing halo artifacts and noise. But the visibility cannot be improved properly especially in the case of images containing heavy or inhomogeneous fog. This is due to the reason that the filters used in such techniques are simple. They do not consider the scene information while de-fogging.

2.2.2.3 Miscellaneous Techniques

Generally, the high-frequency components of an image are associated with the image edge details. While, the low frequency components represent the smooth area of an image. The edge information of a foggy image is usually degraded due to fog. Homomorphic filtering is a technique for image enhancement based upon the principal that high frequency components of a foggy image should be increased while the low frequency components should

be weakened. It has a model similar to the Retinex theory, but it does not need to estimate the incident component [107]. Although, this technique is simple and fast, but it fails to restore a foggy image having dense or inhomogeneous fog.

High-boost filtering is another technique which enhances a degraded image by increasing the high frequency component [31]. It is similar to Retinex technique. The mask image of high-boost filtering is similar to the reflection image of the Retinex technique. This technique fuses the mask and the degraded image to improve its high frequency component. This technique is also simple and fast but causes color distortion and noise amplification in the recovered image.

Another category is the fusion based de-fogging techniques. Schaul *et al.* [105] proposed a de-fogging technique by fusing Near Infrared (NIR) and Visible Light (VL) images. By using weighted least squares optimization framework, two original images were directly fused. This technique fails if the contrast of NIR image under dense foggy weather is less. Ancuti *et al.* [3] proposed an image de-fogging technique by fusing several images derived from the original foggy image. They initially used a semi-inverse approach to detect the foggy regions and then estimated the atmospheric value L_A in clear regions. Several images were then obtained by using

$$L_i = I - a_i \times L_A \tag{2.5}$$

Here a_i is a constant value in the range [0, 1],
$i \in [1, k]$ and k denotes the number of images used for fusion and
I is the original foggy image.

The foggy region detection operation is performed on each image L_i and the area with low hue disparity of the corresponding image L_i is selected as the final input image for fusion. The de-fogged image is then obtained by a simple weighted fusion of the input images. For some images like sea scenes, fog detection based upon this technique fails due to the difference between original and the inverse image. This means, a bad performance will be obtained if fog region detection operation fails.

Ancuti *et al.* ([4], [6]) proposed another de-fogging technique in order to solve the above problem by fusing another two input images also derived from the input image. The first input image is obtained *via* the white balance operation on the original foggy image and the second input image is obtained via a simple linear transformation which is used to enhance the contrast of a foggy image. Finally, the pixel-fusion method which uses three weight maps is selected to fuse the two input images for enhancing the visibility of the foggy image.

Ancuti *et al.* [5] also extended their fusion-based technique to underwater image enhancement. Their proposed fusion based de-fogging technique is simple and fast but fails when an image contains inhomogeneous fog. The reason is that this technique did not take into account the depth information of a foggy image.

Based on the fusion strategy, Fu *et al.* [25] exploited two input images obtained by gamma correction with different scales for sandstorm image enhancement. The fusion-based technique is novel and effective for single

image de-fogging. The second input image is used to enhance the contrast of the fused image and the first input image is used to compensate the color distortion and reduce the halo effect and noise caused by the second input image. In other words, the first image is used to restore the colors and reduce the noise. The second image is used to enhance the visibility of an image. Although these techniques are fast and simple, they cannot achieve good performance if the second input image cannot effectively enhances the visibility of a foggy image.

2.3 Restoration based Image De-fogging Techniques

Techniques belonging to this category are based upon physical model (1.11). The model based image de-fogging techniques find the parameters of the physical model which includes transmission and atmospheric light. Transmission is inversely related to the scene depth whereas atmospheric light depends upon the scene brightness. The de-fogged images can be restored by putting parameters in the physical model (1.11). The images obtained by techniques of this category look natural and clear. This type of image de-fogging techniques are further divided into two types which include multiple images based de-fogging techniques and single image based de-fogging techniques as explained in the upcoming subsections.

2.3.1 Multiple Images based De-fogging Techniques

In such type of image de-fogging techniques, two or more images of the same scene are captured through camera and utilized to de-fog the given image. This type of de-fogging techniques are further classified into two categories on the basis of the fact that whether they use multiple images of the same or different weather as explained below.

2.3.1.1 Multiple Images of same Weather based De-fogging

This type of image restoration techniques uses at least two images of same weather to estimate the parameters of the physical model and then inversely solves the physical model for image restoration. Schechner *et al.* [106] proposed an image restoration technique by using two polarization images of the same scene degraded by same weather. Those two images are taken at parallel and perpendicular orientations respectively. The image de-fogging techniques based upon polarization images assume that the direct transmission component is not affected by the degree of orientation. Since, some images do not contain the sky area, Shwartz *et al.* [110] proposed a novel technique for estimating L_A by choosing two identical features from the scene in an image. To further optimize the de-fogged image and to suppress noise amplification obtained by polarization based de-fogging technique, Treibitz *et al.* [116] proposed an adaptive regularization approach. In the polarization based de-fogging techniques, the value of L_A is estimated manually. Though the polarization based de-fogging techniques perform better than some of the existing de-fogging techniques, but based upon optical filtering process, the manual atmospheric light selection process is not favorable for automatic de-fogging. As the polarization based de-fogging technique is based upon the partial polarization of atmospheric light, when the polarization degree decreases, the effect of

polarization decreases. Also, such techniques fail in the case of dense foggy weather. For some cases like, in the case of moving camera, it is hard to obtain two polarization images of the same scene because the scene change occurs more rapidly than that of the filter rotation.

2.3.1.2 Multiple Images of different Weather based De-fogging

In this section, the existing techniques which use multiple images of different weather conditions to carry out de-fogging process, have been summarized. Narasimhan *et al.* ([81], [82], [83], [84], [85], [86], [87]) studied the effect of using multiple images captured under different weather conditions for carrying out the process of image de-fogging. They analyzed the visual effects of different weather conditions and proposed to use the physical di-chromatic atmospheric scattering model for image de-fogging. They had given a geometric framework based upon the scattering model for foggy scene understanding. The three-dimensional structure and color of the scene was determined from multiple foggy images. If in the case, color of an object present in the scene is similar as that of fog, it is unreliable to use this model for de-fogging. In order to solve this problem, a monochrome atmospheric scattering model was proposed. Narasimhan *et al*. also proposed a fast image de-fogging technique by using this model. Two or more images of a scene in different weather are utilized to find the depth discontinuities and the scene structure by calculating the change in their intensities. The contrast is enhanced by using the scene structure information. They also extended their technique for real time de-fogging, which was able to enhance the visibility of the surveillance scene.

The image de-fogging techniques described above are only suitable for images of surveillance scenes. For other applications especially for vehicle cameras, these techniques may become unreliable because multiple images of the same scene are hard to be captured simultaneously. Since, the monochrome atmospheric scattering model describes how scene intensities are affected by homogeneous weather conditions, so these techniques may not work in weather with inhomogeneous fog also.

2.3.2 Single Image based De-fogging Techniques

As compared to image de-fogging techniques which use multiple images, single image based de-fogging techniques are proved to be more advantages as they are more automated and may require least human intervention. To obtain a de-fogged image from a foggy one, this category techniques extract information from a single foggy image itself and finds the parameters of model (1.11) ([22], [32], [33], [42], [65], [69], [114]). They have received much attention in recent years. Such techniques are able to restore arbitrary foggy images taken under different type of foggy conditions. The techniques come under this category are further summarized in the upcoming subsections.

2.3.2.1 Surface Shading based Image De-fogging

Fattal [23] proposed a technique to estimate parameters of restoration model (1.11) by assuming the fact that surface shading and transmission functions for a given foggy image are locally uncorrelated. After finding the values of parameters t and L_A, the estimation of scene reflection, $R(x)$ were obtained. Fattal's technique relies on, whether the functions of shading and transmission are independent. Since this technique uses statistical property to estimate parameters for image restoration, the performance greatly depends on an input foggy image. The technique may not work well when an image contains dense fog.

2.3.2.2 Local Contrast Maximization based Image De-fogging

Tan *et al.* [112] proposed an image de-fogging technique by using a single foggy image on the basis of two observations. First, the clear day images generally have higher contrast than that of foggy day images. Second, the airlight changes smoothly in a small local area. Tan's technique finds the value of L_A by using the brightest pixels of a foggy image. Tan [112] established that the correlation between airlight and contrast is convex. He casted into a MRF framework and estimated the airlight values for the whole input image. This technique works good for color, gray and thick foggy images. Main drawback of this technique is that the halo artifacts appear around the depth edges due to the local window based operations. Other shortcoming is that when the regions in the input image have no textures, the local contrast remains constant even for the changing airlight values.

2.3.2.3 *DCP* based Image De-fogging

He *et al.* [33] examined large amount of clear day outdoor images and observed that in most areas of a clear outdoor image (except for sky and white areas), there is a channel of pixels with the minimum value close to zero. Using this observation, a statistic of a foggy image called as dark channel is calculated which helps to obtain depth map and hence the parameters (t and L_A) of model (1.11). The dark channel is a window based operation which produces square patches or blocks in a de-fogged image. Therefore, to smoothen the patches, soft matting algorithm was used for the refinement of transmission. This technique is called as DCP de-fogging technique.

The soft matting algorithm used by DCP is too complex and time consuming, so Tarel *et al.* [114] proposed a fast image de-fogging technique by using median filtering and its variant for transmission map refinement instead of using soft matting. This technique can process color or gray scale images in real time. In this technique, the normalized value atmospheric light L_A is set to $(1,\ 1,\ 1)$ using the white balance algorithm. Since, the minimum filter operation applied in DCP causes block artifacts in the transmission map, this technique only uses the minimum channel image to estimate the atmospheric veil $A(x)$ (2.6). Tarel *et al.* assumed that, for each pixel, atmospheric veil is less than the minimal component of a foggy image. The veil is assumed to be smoother in most areas except for the edge areas in an input foggy image. To improve the efficiency of a de-fogging process, while preserving the edge details and corner, this technique used the median filtering and its variant. The following

equation is used to obtain coarse atmospheric veil A, :

$$A(x) = max(min(p' \times B(x), W(x)), 0) \tag{2.6}$$

$W(x) = min_{c \in R,G,B}(I^c(x))$ is the minimal component of the original foggy image,
$B(x) = C'(x) - median_{y \in \Omega(x)}(W - C'|(y))$,
$C'(x) = median_{y \in \Omega(x)}(W(y))$,
p' denotes the restoration degree, $p' \leq 1$.

p' is usually set to a constant in the range of [0.9, 0.95] and Ω is the window of median filtering. Tarel *et al.* used median filter two times to obtain the refined atmospheric scattering veil. The de-fogged image thus can also be obtained by using (1.11). This technique is applicable to both gray scale and colorful images.

Gibson *et al.* [28] gave a scientific interpretation of the fact that DCP technique works well in the case of image de-fogging. The restoration effect becomes better if the foggy image contains more color information. But if the foggy image contains a large portion of sky, white or dense fog area, the theory of DCP becomes unreliable. Also, the soft matting algorithm applied in DCP technique for transmission map refinement is very time consuming process. It cannot be applied in real time applications.

Huang *et al.* [42] investigated the drawbacks of DCP and proposed an improved DCP technique having three modules for single image de-fogging. This technique can also work for sandstorm images. In order to improve the efficiency of DCP technique, Xie *et al.* [124] used MSR to estimate the transmission map.

Gibson *et al.* ([27], [29]) used median filtering instead of soft matting to smoothen the transmission map. In addition to this, Gibson *et al.* [27] had made the conclusion that results obtained by the de-fogging technique are better before compressing the image than that of the results obtained after compression. Using median filtering may cause the degradation of edges in the recovered image. Later on, some researchers used filters having good performance in edge preservation to replace soft matting. These filters include locally adaptive Wiener filter [30], Weighted Least Square (WLS) based edge-preserving smoothing filter [9], bilateral filter [132] and joint bilateral filter ([1], [123]) *etc.*

He *et al.* [34] then modified their DCP technique by proposing an edge preserving smoothening filter called as guided filter. This filter uses foggy image as a guidance image to refine the coarse transmission map. This technique has better edge preservation ability and is faster than that of bilateral and joint bilateral filters. After this, some improved de-fogging techniques were proposed based upon guided filter. Pei *et al.* [93] used the theory of DCP and guided filter to recover night time foggy images. Chen [24] improved DCP technique by using a pair of VL and NIR images to restore the near-infrared image. Lin and Wang [72] found the transmission map by using the image down sampling mechanism to improve the efficiency of de-fogging and then used guided filter to optimize the transmission map.

Meng *et al.* [79] proposed a de-fogging technique based upon DCP by imposing an inherent boundary con-

straint on the transmission estimation function. They used the weighted L_1-norm based contextual regularization method for transmission map optimization. In this technique, the de-fogged image is always bounded as $Q_0 \leq L_0(x) \leq Q_1$, and the coarse transmission map is estimated as

$$\tilde{t}(x) = max_{y \in \Omega(x)}\{min[max_{c \in R,G,B}(\frac{L_A^c - I^c(y)}{L_A^c - Q_0^c}, \frac{L_A^c - I^c(y)}{L_A^c - Q_1^c}), 1]\} \tag{2.7}$$

Q_0 and Q_1 are the two boundary constraints on the transmission map.

L_A is chosen as the highest intensity of each channel after carrying out minimum and maximum filtering using a moving window. For optimizing the coarse transmission map, following transmission function is used by Meng *et al.* with the weighted L_1-norm based contextual regularization

$$\frac{\lambda}{2}||t - \hat{t}||_2^2 + \sum_{j \in \omega} ||w_j \times (D_f * t)||_1 \tag{2.8}$$

λ is the regularization parameter for balancing the two terms of the objective function,
w is a weighting matrix,
D_f is a first-order differential operator,
$\times$ and $*$ are the element-wise multiplication and convolution operators respectively.

After minimizing the above described objective function, refined transmission t can be obtained. This technique has good effect on the recovery of foggy images but refined transmission map is obtained by computing number of iterations which is a time consuming process.

2.3.2.4 Bayesian Image De-fogging

Kratz and Nishino ([65], [88]) proposed a single image Bayesian de-fogging technique on the basis of the fact that scene albedo ρ and depth d are two statistically autonomous components. Wang *et al.* [119] proposed depth map estimation technique based on Bayesian theory and Markov regularization by using multi scale depth fusion. They used the Gaussian function to model the noise. Then, the true depth map was estimated by maximizing the posteriori function. The technique is very persuasive in removing blocking artifacts. But the iterations used by this technique makes it a time consuming process. Also, the parameters are required to be set manually.

2.3.2.5 Machine Learning based Image De-fogging

Tang *et al.* [113] proposed a novel transmission estimation technique by using a machine learning based approach. For image patches, RF model was used to learn the regression model which finds the relation between fog-relevant characteristics and their true transmission. The unknown foggy image is initially divided into small patches and fog-relevant features were extracted. The learned RF model was then used to find the transmission of each image patch. Finally, the coarse transmission map for a complete foggy image is found by combining the transmission of each image patch. The technique also applied guided image filtering to further refine the transmission map.

Zhu *et al.* [136] found the fact that saturation and brightness of a foggy image change strongly with changing fog concentration. In general, the concentration of fog increases with increasing scene depth. By assuming that the scene depth is positively correlated with fog concentration, Zhu *et al.* proposed a linear model by using the saturation and brightness of a foggy image to estimate the parameters of fog degradation model (1.11). Cai *et al.* [17] proposed a trainable end-to-end system called DehazeNet for transmission estimation, with specially designed feature extraction layers. Ren *et al.* [102] proposed a Multi-Scale Convolutional Neural Network ($MSCNN$) for learning the transmission map of a foggy image. It consists of a coarse scale network predicting a holistic transmission map and a fine-scale network for refining the map. However, these techniques usually take convolutional neural networks to learn a mapping from input foggy images to the transmissions or fog free images, without considering fog related priors to constrain the mapping space compared with the traditional methods. Yang and Sun [129] proposed a novel deep learning based technique that integrates fog imaging model constraints and image prior learning into a single network architecture.

2.4 Video De-fogging Techniques

Although, the image de-fogging techniques have good performance in the visibility enhancement of fog degraded images, but in some real-world applications, such as scene surveillance and visual systems of an unmanned plane or vehicle, the real time visibility of a video acquired by the visual system needs to be enhanced. In these situations, such a technique is required which enhances the quality of a scene along with providing high processing speed. Generally, the video de-fogging techniques can be divided into three categories as shown in Figure 2.2.

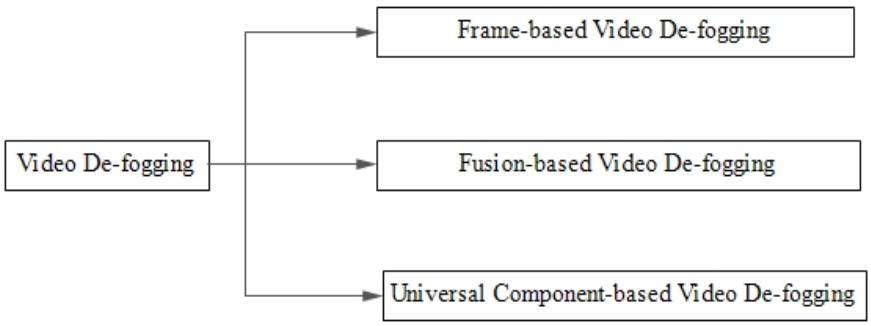

Figure 2.2: Classification of Video de-fogging techniques

2.4.1 Frame based Video De-fogging

The first category is the frame-based video de-fogging techniques which applies single image de-fogging technique on each frame of the video ([10], [27]). For improving the spatio-temporal coherence, Zhang *et al.* [133] proposed an optical flow method to optimize the depth or transmission map. Zhang *et al.* estimated transmission of each frame independently by using DCP technique. Performing single image de-fogging on each video frame is a time consuming process and may leads to color and rightness mutations. When a de-fogging technique

for still image is applied to a video sequence, flicker artifacts may occur because atmospheric values calculated independently for each frame changes frame by frame. Kim *et al.* [60] optimized contrast enhancement by minimizing a temporal coherence cost to reduce flickering artifacts. They initially converts a foggy video sequence into YUV color space. To reduce the computational complexity, this technique only processes the luminance (Y) component, without modifying the chrominance (U, V) components. Kim *et al.* [61] proposed an effective video de-fogging technique to reduce flicker artifacts by using adaptive temporal average. They proposed an approach to calculate global atmospheric light value based on adaptive temporal averaging between adjacent frames. Video de-fogging has a wide range of real time applications, but the challenges mainly come from spatio temporal coherence and computational efficiency. Cai *et al.* [16] proposed a spatio temporal optimization framework for real-time video de-fogging. It reduces blocking and flickering artifacts and achieves high quality enhanced video de-fogging results. This technique builds a MRF with an Intensity Value Prior to handle spatial consistency and temporal coherence. By maximizing the MRF likelihood function, this framework estimates the concentration of fog and preserves the information optimally. Also, to facilitate real-time applications, integral image technique is approximated to reduce the main computational burden.

2.4.2 Fusion based Video De-fogging

The second category contains fusion based video de-fogging techniques which are based upon fusion of enhanced background and foreground images of each video frame. Fusion based de-fogging techniques first extract the background and foreground of each frame. Then, the single image de-fogging technique is used to separately enhance background and foreground images. Finally, video de-fogging can be realized by fusing the enhanced background and foreground images of each frame. Fusion based de-fogging techniques restore only the background image, which allows the efficiency of the video de-fogging to be improved. Some researchers proposed to use the frame difference method to extract the background and foreground image of each frame and use the $CLAHE$ technique to enhance the background and foreground images, respectively ([100], [126]).

John *et al.* [53] also proposed a video de-fogging technique based on the separation of background and foreground of a video. They first used the single image de-fogging technique based on physical model to enhance the background image and simultaneously obtained the global lightness parameter. Then, the estimated lightness parameter was used to enhance the foreground image of each frame. Finally, the enhanced video was obtained via fusion of the enhanced background image and each enhanced foreground image.

Under the foggy weather condition, the foreground image which contains the targets, is not easy to accurately extract. Therefore, it may lead to color or brightness mutations of two adjacent frames. The reason is that single image de-fogging techniques do not take into account the correlation of color and brightness information of adjacent frames. Yoon *et al.* [131] proposed an improved DCP de-fogging technique which uses the multiphase level set formulation method to replace the soft matting algorithm to restore each frame of the video and then proposed a color correction method to solve the color mutation problem.

2.4.3 Universal Component based Video De-fogging

The third category of the video de-fogging techniques is the universal component based de-fogging. The techniques under this category are based on the estimation of a universal component that can be used in all video frames. Universal component based video de-fogging techniques try to estimate a universal component which represents the fog distribution and apply it to subsequent frames of a video. These video de-fogging techniques are reasonable and are able to improve the time efficiency.

Xie *et al.* [125] used the transmission map of background image of the scene which is the universal component for video de-fogging. Although taking the transmission of the background image as the universal component can greatly improve the efficiency of video de-fogging, some enhanced video frames especially the frames which have a large difference from the background suffer from edge degradation and halo artifacts. The universal transmission estimated from the background is not the real transmission of the subsequent video frames. Previous frames do not have the same edge or depth information with the subsequent video frames especially the frame which has many targets, so some edges of the targets get degraded.

Zhang *et al.* [127] also took the transmission of the key frame as the universal component and used the optical flow method to estimate the transmission of a non key frame to improve the efficiency.

2.5 Gaps in Literature Survey

In context to the literature survey conducted on the existing techniques of fog removal from image and videos, following gaps have been found which are listed below:

i Existing techniques of image de-fogging do not work well when pixel colors are totally over shadowed by fog ([2]- [6], [32]- [33], [49]- [51], [57]- [59]).

ii Most of the research has considered the atmospheric light- a global constant for entire image or a video frame whereas in the case of image which contains one or more light sources other than the natural light present in the atmosphere, the concept of global atmospheric light does not work well and de-fogged image is not of a good quality ([33], [108], [109], [114]).

iii Most of the techniques find the atmospheric light as the brightest pixels in the image, but this causes the pixels which are similar to the color of the atmospheric light suffers and leads to saturation of those pixels ([33], [114])).

iv Techniques of removing fog suffer from halo artifacts, *i.e.*, distortion of the scene points near the edges [114].

v Images captured during different hours of the day, especially night time foggy images have not been studied. ([2], [89], [91], [101], [130]).

vi Computational time is very high so that to apply them on video becomes a challenge because for a video, a minimum of 30 frames per second are needed to be processed ([8], [23], [29], [42], [66], [80], [85], [114]).

vii The static image de-fogging technique is applied to each frame of the foggy sequences independently. It causes flickering artifacts due to the variations of the estimated atmospheric light among frames. The small differences in the atmospheric light severely change the color tones of restored frames [72].

2.6 Objectives of the Thesis

On the basis of gaps identified in the literature survey, following objectives are proposed for this work.

i To review existing techniques of de-fogging.

ii To develop efficient technique(s) for removing fog from digital images in different kinds of environments with varying amount of fog.

iii To extend the developed technique(s) for the images de-fogging to video frames.

iv To validate and compare the proposed technique(s) with existing de-fogging techniques.

2.7 Methodology used in De-fogging

i Different type of foggy images are taken from existing databases. These images represent the different day times with varying fog and varying environmental conditions from two different databases including "Waterloo IVC Dehazed Image Database" [74] and "$LIVE$ Image De-fogging Database by Texas University" [19]. The third database taken is "$FRIDA$" [115] which is a dynamic database containing road images. Using the depth maps given in this database, the foggy images are generated having varying fog densities by changing the values of β (the atmosphere scattering coefficient).

ii By using the foggy images, the de-fogged images are obtained by using the proposed image de-fogging techniques. The implementation is performed in $MATLAB$ 2016a, with $Intel\ i5$, 1.60 GHz, $Quad-Core$ processor and $8GB\ RAM$.

iii The de-fogging results are compared with existing techniques on the basis of six quality parameters including Average Gradient, Color Naturalness Index, Fog Reduction Factor, Visual Contrast Measurement, Colorfulness Index and Color Information Entropy. The techniques are also compared with state-of-art techniques on the basis of their execution time.

iv The quality parameters and de-fogging results of existing techniques are obtained by using $MATLAB$ codes provided by the authors from ([19], [37], [39], [43], [128]) and $MATLAB$ inbuilt codes. The results are taken in $MATLAB$ 2016a, with same system configuration as described above.

v For video de-fogging technique, first video frame is extracted and considered as a reference frame. By using the information found from the reference frame, further frames are processed and then the reference frame is updated according to scene change detection.

vi The video de-fogging results are also compared with existing techniques on the basis of temporal coherence, spatial coherence and computational time. For temporal coherence, Histogram Correlation Coefficient is used. For spatial coherence, six quality parameters including Average Gradient, Color Naturalness Index, Fog Reduction Factor, Visual Contrast Measurement, Colorfulness Index and Color Information Entropy are used whereas computational time for de-fogging the complete video is used to compare the de-fogging techniques.

Chapter 3

Minimum Preserving Subsampling based Fast Image De-fogging

3.1 Introduction

DCP based techniques produce better de-fogging results in comparison to other techniques, but their main limitation is the dark channel estimation step as it takes long processing time. Due to this, these techniques are not suitable for real time applications. In this Chapter, a novel approach to subsample the image is proposed which preserves the value of local minimum in a patch to obtain the dark channel efficiently. This mechanism is significantly faster than normal dark channel while producing better de-fogging results. In order to remove the blocking artifacts produced by dark channel, transmission map is refined by using fast guided filter. In this, texture details from the guidance image are removed to produce high contrast images. The atmospheric light is calculated from top portion of the image by ignoring pixels of bright light sources inspired from Kansal *et al.* [55] which produces better quality de-fogged images and also saves computational time. To make the results look uniformly bright, adaptive post processing is performed on the de-fogging results. †

Apart from efficient dark channel estimation, other limitations of the DCP technique have been addressed in this Chapter. Since DCP estimates global atmospheric light in such a way that it can choose bright objects as candidates of atmospheric light, which may cause restored images to look over dark. Such pixels have been identified before estimating atmospheric light and hence been rejected during the process which avoids the over darkness problem. Also, results of DCP suffer from non uniform brightness due to single value of atmospheric light and hence some portions of the restored image look dull and dark. For this, post processing is performed, which enhances the under exposed regions and makes the restored images look uniform in brightness. Considering the growing usage of DCP technique in various image and video de-fogging applications, the simple speedup

†**Contents of the work presented in this Chapter have been published in *Journal of Modern Optics*, 65(18), pp. 2103-2123, 2018. (SCI Indexed)**

would improve the performance of those applications.

Koschmieder described fog degradation model (1.11) which is widely used to describe the formation of foggy images. He *et al.* [33] proposed DCP technique for model based image de-fogging by using the observation that for a clear day image, for each pixel, minimum among its *3D* square window, called as dark channel, is almost equal to zero. Using this fact, parameters of (1.11) were estimated from foggy image and then used for image de-fogging. The dark channel I^{dark} of a foggy image I is found as:

$$I^{dark}(x) = min_{y \in \Omega(x)}(min_{c \in \{R,G,B\}}(I^c(y))) \tag{3.1}$$

Here $\Omega(x)$ is the $2D$ window centered at x. Coarse transmission $\tilde{t}$ at each pixel location is found by using dark channel according to (1.31). $\tilde{t}$ produces halo artifacts in a de-fogged image, therefore transmission map is refined using soft matting to produce clear de-fogging results. To estimate global atmospheric light, DCP technique uses top 0.1% brightest pixels of dark channel. The image pixel $L_0(x)$ is recovered by using (1.32).

3.2 Proposed Minimum Preserving Subsampling based Image De-fogging Technique

This section describes the flow of the proposed minimum preserving subsampling based image de-fogging technique. In DCP based techniques, for each pixel, estimating $W \times W$ dark channel, $3 \times W^2$ operations are required. Those operations have been reduced significantly by using minimum preserving downsampling in the proposed technique. The overall dark channel construction mechanism has been explained in next sub-section. For a de-fogging process, dark channel needs to be calculated twice. One for estimating atmospheric light and another dark channel for normalized foggy image to estimate transmission map. So a cost reduction will be even more beneficial. Apart from this, while estimating atmospheric light, DCP technique could select non candidate pixels, *e.g.* bright light sources, *etc.* which have been removed for better color restoration in the proposed work. Selecting a single value of atmospheric light may also produce illumination variations in the restored image which causes some portions to look dark. To solve this issue, the post processing is applied which improves the under illumination regions without increasing the time complexity significantly. Figure 3.1 shows the flow of proposed technique.

3.2.1 Dark Channel Construction and Transmission Estimation

In DCP based existing techniques dark channel produces patch wise constant values throughout the image. In the proposed work, dark channel for a given image is constructed so as to reduce the redundant calculations along with maintaining the idea of preserving local minimum value in a patch. Figure 3.2 shows the block diagram of the proposed dark channel construction process. Initially, a $M \times N$, RGB foggy image I is divided into fixed

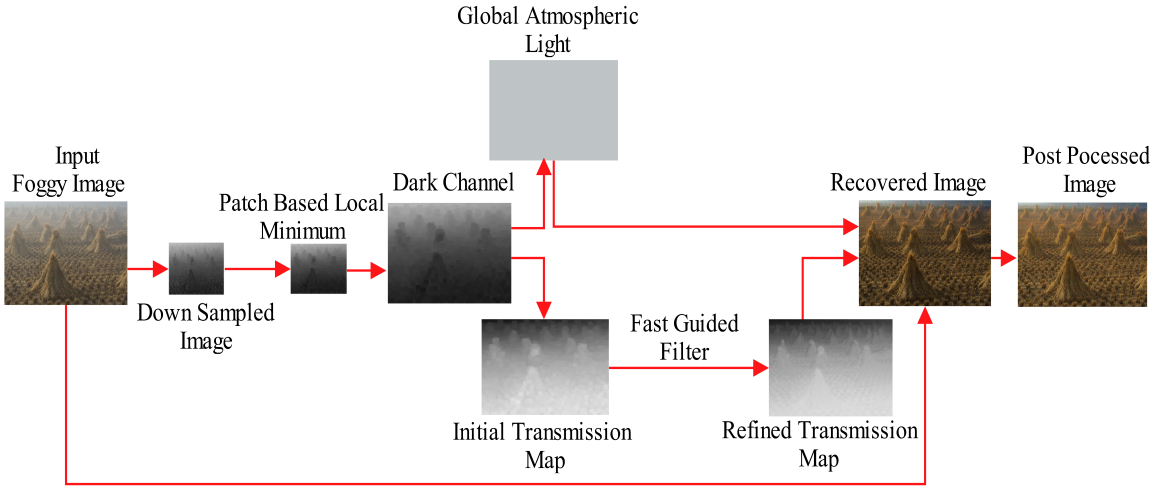

Figure 3.1: Block Diagram of the Minimum Preserving Subsampling based Image De-fogging

size non overlapping s_b blocks (B_1, B_2,.., B_i.....B_{s_b}) of size $m \times m$. Then, a $2D$ subsampled image I_{ds} with size $\frac{M}{m} \times \frac{N}{m}$ is created in such a way that each pixel in I_{ds} is obtained from each respective block B_i by taking the minimum in the respective block as

$$I_{ds}(x) = min(B_i), \quad i = 1, 2, 3, ...s\_b \tag{3.2}$$

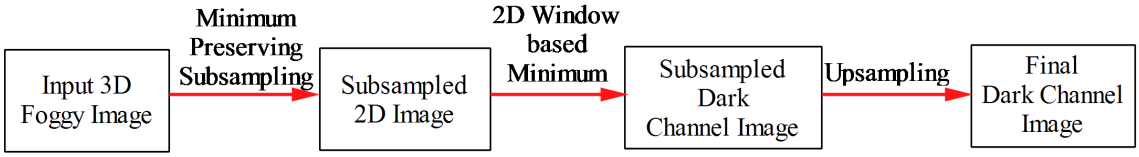

Figure 3.2: Subsampling based Dark channel construction Process

Here min specifies the mathematical operation to find the minimum intensity value in a block B_i. After obtaining I_{ds}, the subsampled dark channel image I_{ds}^{dark} is estimated, whose each pixel x is obtained by taking the minimum in a $2D$ window centered at x as

$$I_{ds}^{dark}(x) = min_{y \in \Omega(x)}(I_{ds}(y)) \tag{3.3}$$

Here Ω is the window of size $w \times w$. After this, upsampling of I_{ds}^{dark} with scaling factor, m, using nearest neighbor interpolation method is performed to obtain the final dark channel image equivalent to original dark channel (I^{dark}) with window size $(w \times m) \times (w \times m)$. In this work, nearest neighbor interpolation scheme has been used which does not put a significant time overhead as it involves the replication of pixels without performing any internal operations. Generally, for dark channel estimation, 15×15 patch is used. Therefore, to show the further details of the proposed technique, same patch size has been considered. To construct 15×15 dark channel with the proposed technique, a set of 4 possible combinations of m and w are listed in column 1 of

Table 3.1: Number of operations to construct proposed dark channel with different values of m and w.

Parameters	**Number of Operations**
$m = 15, w = 1$	$3 \times M \times N + c_1$
$m = 5, w = 3$	$3.36 \times M \times N + c_2$
$m = 3, w = 5$	$5.78 \times M \times N + c_3$
$m = 1, w = 15$	$228 \times M \times N$

Table 3.1. In second column, number of operations corresponding to parameters m and w are listed to estimate the dark channel in terms of image size ($M \times N$). c_1, c_2 and c_3 are the execution time for upsampling which do not put a significant contribution in the overall dark channel operations. For $m = 1$ and $w = 15$, dark channel is estimated by first taking the minimum value for a given pixel in RGB color channels and then the window based minimum is estimated in the respective color channel. For $m = 15$ and $w = 1$, the patches produced by proposed technique are totally non overlapping and generates a significant change in original and proposed dark channel. That is why, these cannot be considered to estimate transmission map. The dark channel estimated by using $m = 5, w = 3$ & $m = 3, w = 5$, can be considered for transmission estimation because, by using these, the dark values produced will be equal to the original dark channel inside the patches while a minute difference exists at the patch boundaries which will not produce significant difference in the overall transmission estimation. Since, for boundary pixels, original dark channel uses half of the window, therefore, while estimating proposed dark channel some preprocessing steps have to be done, which bring the respective blocks at their actual positions according to original dark channel. Transmission map is estimated with the help of dark channel by using (1.31).

Lin *et al.* [72] also used subsampling mechanism to obtain transmission map in a time efficient manner. Lin's technique subsamples the minimum color channel and obtains dark channel from the low resolution (subsampled) image and then upsamples it after smoothening and inversing to produce final transmission map. This technique does not preserve local minimum value in a patch, as shown in Figure 3.3(c) (red window) in the dark channel whereas the proposed dark channel can do the same to a larger extent as shown in Figure 3.3(d). Proposed technique obtains same dark channel values as that of original dark channel everywhere except the patch boundaries, as shown in Figure 3.4(g). In original dark channel, a patch is produced using a local minimum operation. This patch production is due to the influence of a single minimum value lying inside 15×15 window of each pixel belonging to that patch (*e.g.* pixel *j* in peach color patch in Figure 3.6. Two patches are shown in this figure, out of which one is a non-overlapping patch (the one in peach color having center at pixel *j*) and other is an overlapping patch (the one in gray color having a center at i). During the proposed dark channel, when down sampled image is created, that minimum value (j) is transferred from $5 \times 5 \times 3$ window to a single pixel in a down sampled image which can again form a 3×3 patch using 3×3 dark channel. When this window is resized 5 times, the equivalent peach color patch is generated in the proposed dark channel as shown in right hand side of Figure 3.6). It might be possible that the patch formed in the proposed dark channel becomes bigger or smaller than patch of original dark channel (*e.g.* gray patch) because, in the original dark channel, for each pixel, dark channel is independently calculated, whereas, in the proposed dark channel, for each 5×5 window, the minimum value obtained is copied

to a local 5×5 window due to direct nearest neighbor up sampling. This can be seen from gray patch of the proposed work. When the difference between original and proposed dark channel is calculated, the difference lies at the boundary of a patch as shown in Figure 3.4 (g). In Figure 3.6, it can be seen that, in original dark channel, in gray patch three rows are created in bottom and 4 columns are created in the right with center pixel i, whereas, in the proposed dark channel, a set of minimum 5 is created on both sides due to nearest neighbor up sampling which creates a difference at the boundary of some another patch.

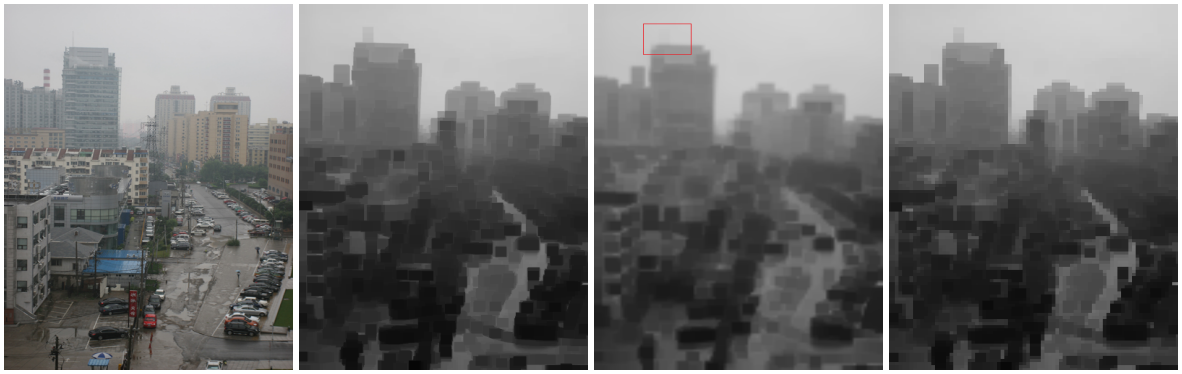

(a) (b) (c) (d)

Figure 3.3: (a) Input Foggy Image. 15×15 Dark Channels obtained using (b) Existing technique in (3.1) (c) Lin *et al.* [72] Technique (d) Proposed Technique ($m = 5, w = 3$)

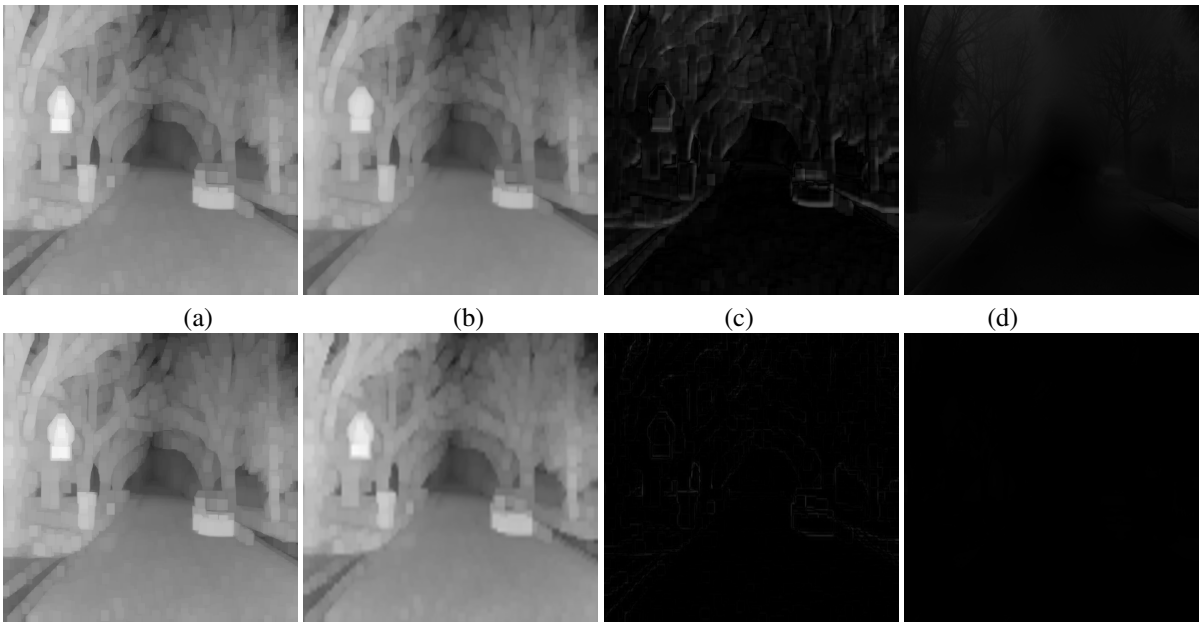

(a) (b) (c) (d)

(e) (f) (g) (h)

Figure 3.4: Comparison between original and proposed dark channel based transmission maps for Foggy input image shown in Figure 3.5 (a). (a and e) Original 15×15 Dark Channel based transmission map. (b) Transmission map obtained using Lin *et al's* [72] technique. (c) Absolute difference between (a and b). (d) Absolute difference between (Guided Filtered(a) and Guided Filtered (b)). (f) Proposed Dark Channel based transmission map with $m = 5, w = 3$. (g) Absolute difference between (e and f). (h) Absolute difference between (Guided Filtered(e) and Guided Filtered(f)).

This difference generated in the original and the proposed dark channel does not produce significant difference

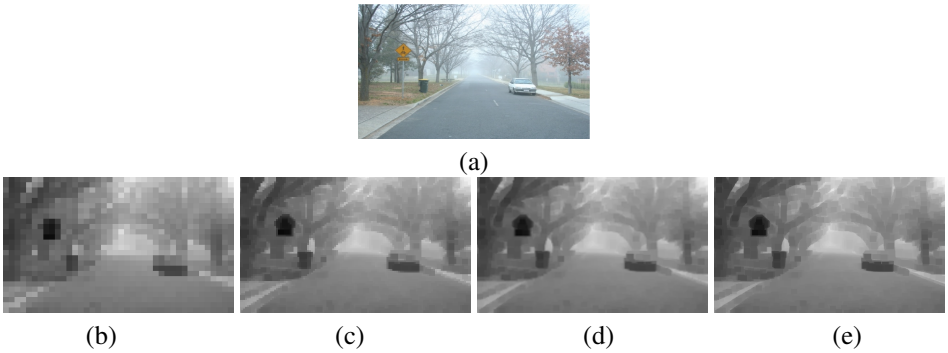

(a) (b) (c) (d) (e)

Figure 3.5: (a) Input Foggy Image "$Road$". 15×15 Dark Channels obtained using proposed technique with (b) $m = 15$, $w = 1$ (c) $m = 5$, $w = 3$ (d) $m = 3$, $w = 5$ (e) $m = 1$, $w = 15$

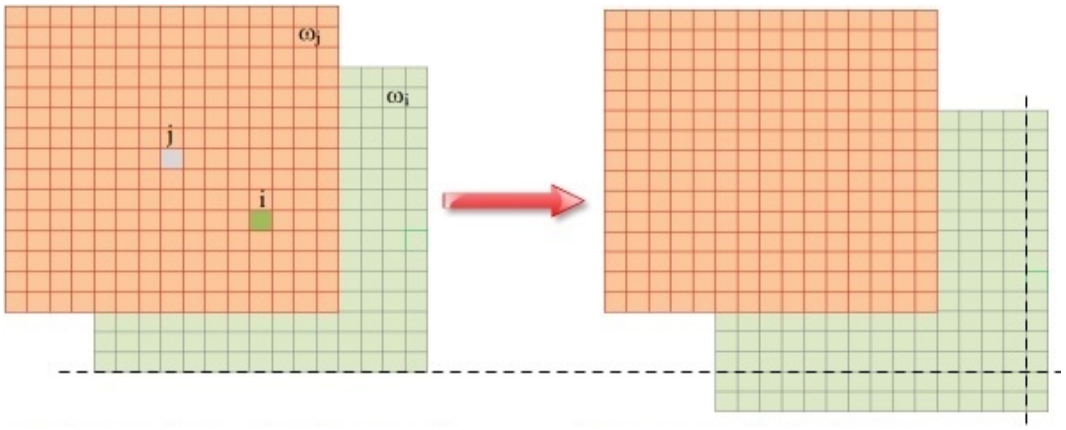

Original Dark Channel Proposed Dark Channel

Figure 3.6: Example of Difference between Original and Proposed Dark Channel

in their transmissions. In order to refine the transmission map, edge preserving smoothening is carried out, which preserves the value of initial transmission near the edges and smoothening the others. The values inside the patch of dark channel are more close to edge as compared to others. Therefore employing edge preserving smoothening cause the proposed dark channel based transmission to become almost equal to original dark channel based transmission. If the dark channel is obtained using Lin *et al's* procedure as explained above, the difference exists all around the space as shown in Figure 3.4(c) which fails the condition of DCP. In the next sub section, edge preserving smoothening based transmission refinement method is discussed.

3.2.2 Transmission Refinement

Since the dark channel is a patch wise constant value, which produces blocking artifacts around the edges [33], [109] *etc*. There are number of edge preserving smoothening filters available to remove the blocking artifacts including bilateral filter, anisotropic filter, trilateral filter and guided filter *etc.* [92]. He *et al.* [34] used guided filter for transmission refinement to perform smoothening in almost $O(N)$ time. This filter can shift the structure of an input foggy image to the filtering transmission map t. The guided filter effectively suppresses gradient reversal artifacts and produces visually appealing edge profiles. Guided filter is driven by local linear model

between the guidance I_g which is the Gaussian blurred foggy image I and the filtering transmission map t', is represented as

$$t'(y) = a_x \times I_g(y) + b_x, \quad \forall y \in \omega_x \tag{3.4}$$

y is the index of a pixel, a_x and b_x are the coefficients which are assumed to be constant in a window ω_x having radius r. Gaussian blur is applied to guidance image in order to reduce the texture details in the transmission map. This improves the contrast of de-fogged images. For transmission t, the reconstruction error between t and t' is minimized which gives the solution:

$$a_x = \frac{\frac{1}{|\omega(x)|}\sum_{y\in\omega(x)}(I_g(y) \times t_x) - \mu_x \times \bar{t_x}}{\sigma_x^{'2} + \epsilon} \tag{3.5}$$

$$b_x = \bar{t_x} - a_x \times \mu_x \tag{3.6}$$

For a given window $\omega(x)$ in I_g, μ_x and σ'_x are the mean and variance respectively, and ϵ is the regularization parameter which controls the degree of smoothness of t'. $|\omega(x)|$ is the number of pixels in window $\omega(x)$, $\bar{t_x} = \frac{1}{|\omega(x)|}\sum_{y\in\omega_x} t_x$. The edge preserved smooth transmission map t' is then obtained using

$$t'(y) = \frac{1}{\bar{\omega}_x} \sum_{x,y\in\omega(x)} (a_x I(y) + b_x) \tag{3.7}$$

In Figure 3.7, two things have been shown. First, the green color points shows the difference between the original and the proposed dark channel. Second, the lines in purple color shows the depth edges of the "mountain" image. For edge preserving smoothening, two rules defined by He *et al.* [34] are:

(i) **Rule 1:** If the guidance image I_g changes a lot in a window $\omega(x)$, then the variation in a patch $\sigma_x^{'2} >> \epsilon$, hence $a_x \approxeq 1 \; and \; b_x \approxeq 0$. So the value of transmission is preserved by using (3.7).

(ii) **Rule 2:** If the guidance image I_g is approximately constant in a window $\omega(x)$, then $\sigma_x^{'2} << \epsilon$, hence $a_x \approxeq 0$ and $b_x \approxeq 1$. So the transmission values in the corresponding patch are smoothed by averaging the pixels in a local window.

Figure 3.7: Example showing the difference between the original and proposed dark channel with respect to edges

Therefore, during the smoothening process of dark channel, pixels belonging to edge regions remain same after refinement according to Rule 1. It can be seen in Figure 3.7, that there is no clear difference between original and proposed dark channel at the edge points. therefore after the refinement step, both dark channels will produce equivalent results near and on the edge points. Pixels away from the edges get smooth according to Rule 2 depending upon how far they are from edges. During smoothening, these pixels are replaced with the average of the pixels present in the local window ω. Therefore, the values of pixels obtained after refinement of original and the proposed dark channels are very close to each other. Hence, Root Mean Square Error ($RMSE$) between these two becomes close to zero as shown in Figure 3.8(b). The number of patches produced in the dark channel depends upon the randomness of the image data which further depends upon the number of edges present in an image. If the degree of fog is increased, the edges start disappearing and therefore the randomness in the patches start reducing and hence the $RMSE$ between the original dark channel becomes very much close to zero as shown in Figure 3.8(b).

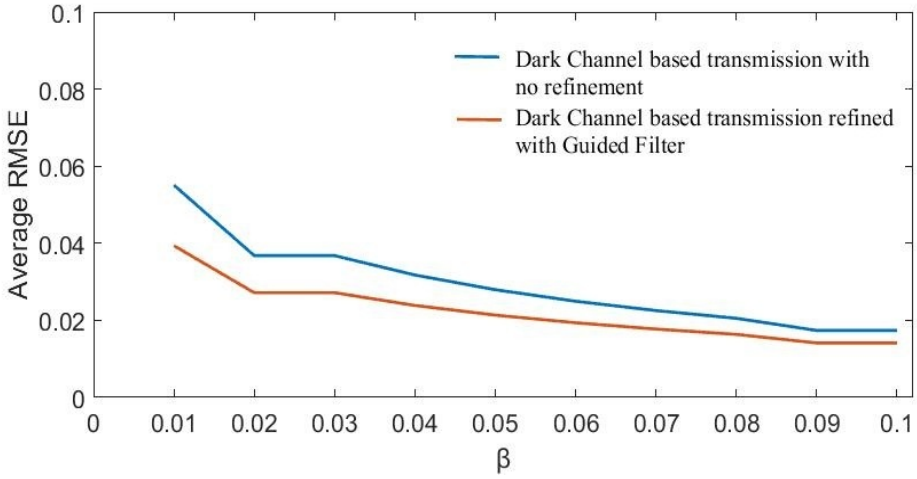

(a)

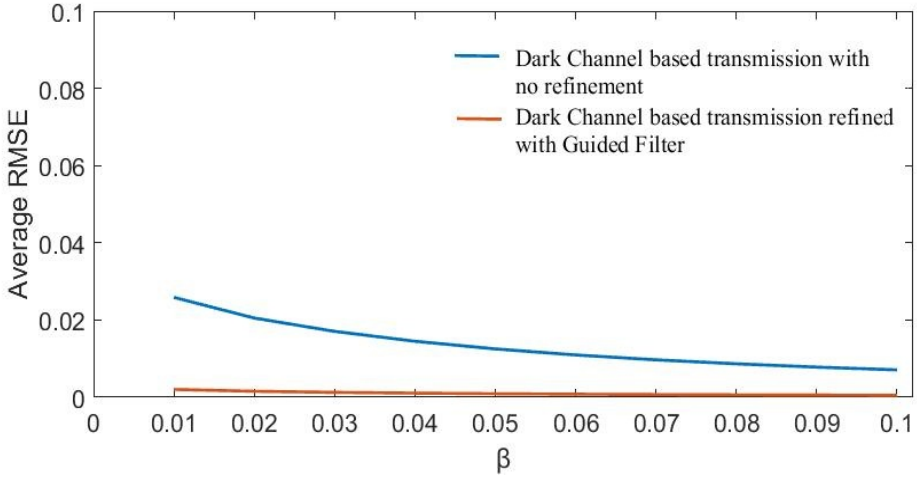

(b)

Figure 3.8: Average $RMSE$ between transmission maps obtained using (a) Original 15×15 dark channel and dark channel obtained by Lin *et al's* [72] mechanism. (b) Original dark channel and proposed dark channel with ($m = 5$ and $w = 3$).

To further speed up the de-fogging process, fast implementation of guided filter is chosen which improves the speed of guided filter by performing the operations on down sampled input images with scaling parameter s. He *et al.* [35] observed that, if edge preserving smoothening is done by subsampling the filtering and the guided image with scaling factor $s = 4$, similar results can be achieved as that of full resolution images. With fast guided filter, the transmission map t, and the guidance input image I_g are subsampled (nearest-neighbor or bilinear) with scaling factor s. All the window based filters are performed on the subsampled maps. The two coefficient maps $\bar{a}$ and $\bar{b}$ are upsampled (bilinear) to the original size. Finally, the filtered transmission map t' is computed by using (3.7) with upsampled coefficients and the guidance image.

To show that the proposed technique obtains similar results as that of original dark channel, we have considered, $FRIDA$ [115] which contains 66 test images. Synthetic fog is added to all the images with different β values (from $\beta = 0.01$ to 0.1) for given depth map d and the ground truth atmospheric light $L_A = 220,\ 235,\ 254$ using (1.10). For all the images with different fog thickness, 15×15 transmission maps are obtained using original dark channel, dark channel obtained by Lin's technique [72] and the proposed technique. The transmission maps obtained using above three dark channel construction mechanisms are refined by using Guided filter [34]. Figure 3.8 (a) shows the Root Mean Square Error ($RMSE$) between original and Lin's technique based transmission maps and Figure 3.8 (b) shows the $RMSE$ between original and proposed dark channel based transmission maps. In Figure 3.8 (b), it can be observed that $RMSE$ between original and proposed dark channel based transmission maps almost become zero after applying guided filter. This is due to the reason that, original and proposed dark channel differ only at the patch boundaries which are generally the halo artifact regions [109]. Such regions become smooth after transmission map refinement and smoothening causes the transmission value of the concerned pixel modified by using the transmission values of surrounding pixels. From Figure 3.8 (b), it can be seen that the $RMSE$ between original and proposed dark channel based transmission map (without refinement) is decreasing with increasing fog (β) because it causes more number of edges to disappear in the foggy image. $RMSE$ between guided filtered transmission maps is almost negligible for all values of β which makes it clear that the difference between original and proposed dark channel lies only around the patches containing edges. This difference can be recovered using edge preserving smoothening in transmission map. Figure 3.8 (a), shows that Lin *et al's* approach produces unpredictable gaps between original and the concerned transmission map which in turn will produce unreliable de-fogging results. Also, the average dark channel value produced by original dark channel and proposed technique for all images of $FRIDA$ are equal as shown in Figure 3.9 whereas the average dark value produced by Lin *et al's* approach are different. It can now be concluded that, the proposed technique takes approximately $O(N)$ time for dark channel construction saving a lot of computational time and produces similar results as that of original dark channel. The same experiment is performed for various other foggy images and similar conclusion has been drawn.

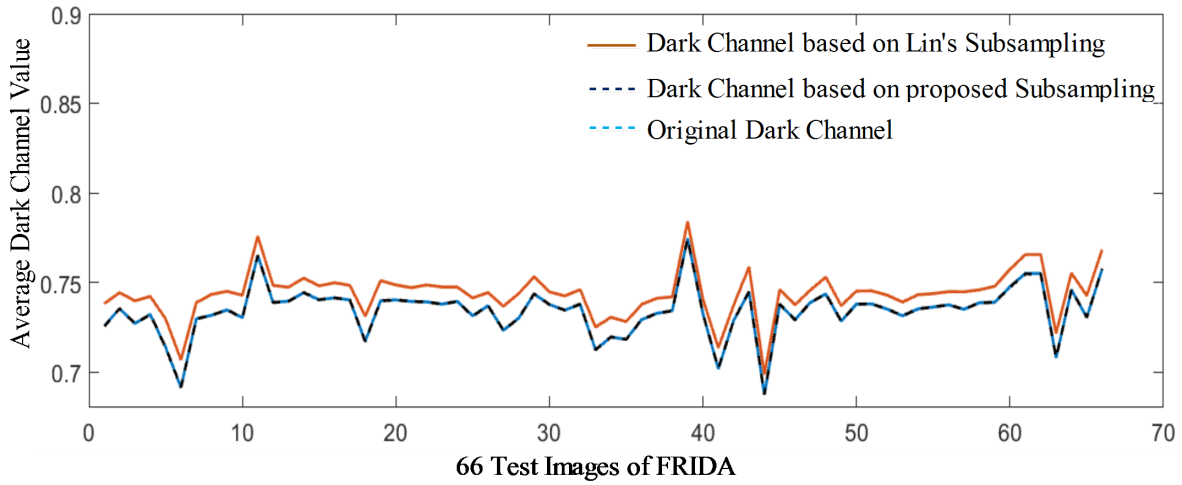

Figure 3.9: Average dark values produced by different dark channel estimation methods.

3.2.3 Atmospheric Light Estimation

According to Koschmieder model, the scene point value of a foggy image approaches to global atmospheric light in regions of infinite depth. Such regions generally lie at the top of an image. Therefore, in the proposed work, to save the computational time, approximately 25% top image rows are extracted and their corresponding dark channel is estimated by using proposed subsampling technique. According to He *et al.* [33], bright pixels in the dark channel represent most fog opaque region, but it may contain some bright light objects which may cause the value of global atmospheric light to become too bright. Such objects are filtered by applying 3-σ rule on YUV color space corresponding to colorful image I. Y in YUV color space represents luminance information whereas U and V represent the respective color information. According to Kansal *et al.* [55], for illuminated regions, any of the Y, U, V channels or all of them together have very high values. With the help of this fact, such regions can be filtered prior to atmospheric light estimation. After identifying the brighter pixels from the selected foggy image portion, their corresponding dark channel values are set to zero, so that they must not be selected as the candidates of atmospheric light. Finally, the values in R, G, B color channels corresponding to 0.1% top brightest pixels from the dark image are selected as global atmospheric light L_A. The effect of filtering the bright sources has been shown in Figure 3.10. In Figure 3.10 (d), the filtered pixels are indicated by red color. If the dark channel is directly used, the recovered image looks over dark as shown in Figure 3.10 (e) whereas if the pixels are filtered by the proposed technique, the results look more bright and clear as shown in 3.10 (f).

3.2.4 Image Restoration and Post Processing

After obtaining the global atmospheric light L_A and the refined transmission map t', the de-fogged image L_0 is recovered by using (1.32) from the foggy image I. Since the foggy image is affected by the environment lightening, some parts of the de-fogged image may suffer from low brightness and due to dark channel prior based image restoration, de-fogged images become even more darker. Therefore, in the proposed technique, a combined

Figure 3.10: Effect of pixels filtering on atmospheric light and overall de-fogged image. (a) Input Image. (b) Top $\frac{1}{4}$ rows of an input image. (c) 15×15 dark channel of image in (b). (d) Bright pixels filtered from (c). (e) Restored image by using dark channel in (c). (f) Restored image by filtering bright pixels in dark channel.

color channel transmission map is used to identify under exposed (low contrast) regions and an adaptive technique is used to enhance such regions without making any color distortion. Since, the low and high intensity values of each color channel represent darker and brighter regions respectively of an image [46] for that color channel. To identify the overall darker regions in a colorful image, the combined color channel darkness effect C^d is estimated by using

$$C^d(x) = (1 - \frac{L_0^R(x)}{max(L_0^R)}) \times (1 - \frac{L_0^G(x)}{max(L_0^G)}) \times (1 - \frac{L_0^B(x)}{max(L_0^B)}) \tag{3.8}$$

Here L_0 is the de-fogged image, max is the mathematical operator to find the maximum value in each color channel RGB. Now, C^d is normalized in the range $[0, 1]$ to obtain normalized combined color channel darkness effect as:

$$C_n^d(x) = \frac{C^d(x) - min(C^d)}{max(C^d) - min(C^d)} \tag{3.9}$$

The value of C_n^d is highest in the darkest region, which helps to enhance those regions more. Finally the processed de-fogged image L_0' is obtained by using

$$L_0'(x) = L_0(x) \times e^{(C_n^d(x) \times v)} \tag{3.10}$$

Here v is the scaling factor to adjust the image brightness. By experimenting with number of images, it has been found that the post processing results are better for values of v near 0.5. Therefore, to show the results, we have chosen the value $v = 0.5$. However the images can be made more bright by increasing v. exp is the exponential operator which abruptly increases C_n^d values of darker regions while keeping the brighter region's low. The effect of post processing has been shown in Figure 3.11. Figure 3.11(a) shows the input image, Figure 3.11(b) shows the restoration without post processing. Under enhanced region is shown in yellow box. Figure 3.11(c) shows the restoration with post processing and the improved region is shown in yellow box.

Figure 3.11: Effect of pixels filtering on atmospheric light and overall de-fogged image. (a) Input Image. (b) Restored Image without Post Processing. (c) Restored Image with Post Processing.

3.2.5 Algorithm of Minimum Preserving Sampling based Image De-fogging Technique

The steps involved in procedure of the proposed minimum preserving subsampling based image de-fogging technique have been summarized in the Algorithm 3.1:

Algorithm 3.1: Minimum Preserving Sampling based Image De-fogging Technique.

i Obtain image I' by extracting top 25% image rows of I. Find dark channel image I'^{dark} from I' by using the procedure explained in in Section 3.2.1. Finally, obtain L_A^c from I'^{dark} by using the procedure explained in Section 3.2.3.

ii Find I^{dark} from the normalized foggy image $(\frac{I^c(x)}{L_A^c})$ by using the procedure described in Section 3.2.1 and obtain the transmission map by using the procedure in Section 3.2.2.

iii Obtain the de-fogged image L_0^c from I, L_A^c and t by using (1.32).

iv Obtain the post processed image $L_0^{c'}$ from L_0^c by using the procedure described in Section 3.2.4.

3.3 Experimental Results and Analysis

Proposed technique has been implemented in $MATLAB$ 2016 and tested on various standard foggy images of Choi's database [19] and Waterloo *IVC* dehazed image database [74]. These databases contain many hazy and foggy images taken in different type of environments. There are number of images reflecting lightening conditions of different day times. In next section the results of various techniques have been shown on images including $City1$ which is a morning time image representing hazy buildings, whereas $Toys$ and $People$ are day time images representing the toys and people captured in hazy conditions. $Cones$ is an image taken in wheat field during morning time in moderate fog, $Cityscape$ is heavy fog image representing fog covered buildings and road. $Foggy\_road2$ is also moderate fog image taken on road and ground during day time. $Foggy\_ground2$ is a heavy fog image taken in ground during morning time. These images have been selected as these are capable of showing the performance of de-fogging techniques in different environments and day times. Both objective as well as subjective evaluations have been carried out to show the effectiveness of the technique.

3.3.1 Subjective Evaluation

In this section, the results of the proposed technique have been visually compared with existing techniques including Fattal [23], Tarel *et al.* [114], He *et al.* [34], Cai *et al.* [17], Choi *et al.* [18], Meng *et al.* [79], Zhu *et al.* [136], Ren *et al.* [102], Liu *et al.* [73], Colores *et al.* [104] *etc.* The transmission maps and their corresponding restored images obtained by using the proposed technique have been compared with transmission maps of He *et al.*, Zhu *et al.* and Lin *et al.* [72] in Figure 3.12 for "$Cones$" image. It can be seen that Lin's map is extremely dark due to which its restored image is also dark. This is due to the reason that minimum value in the dark channel is not preserved during direct downsampling which yields brighter dark channel and hence darker transmission map. Furthermore, guided filtering is applied on down sampled dark channel, due to which the edges preserved by guided filtering become vague after upsampling which can be observed in Figure 3.12 (d and h). Zhu *et al's.* technique estimates depth map by learning the parameters of the linear model with a supervised learning method. Although, learning strategies are effectively being used in various research fields nowadays, but they require a sufficient information to predict the effective outputs. If the adequate dataset is not available, reliable depth maps can not be obtained (as seen in Figure 3.12(c), depth edges are totally disappeared in upper half of the depth map) due to which unreliable de-fogging results are produced as shown in Figure 3.12(d). The output of the the technique is also compared with He's technique and is found better in three ways. First, the texture details in transmission map are refined by using Gaussian smoothening, which produces smoother transmission map and hence better contrast de-fogged images. Second, the illumination variation in the recovered image due to single value of atmospheric light in He's technique is improved by using post processing technique. This results in stable illumination throughout the image which can be seen in Figure 3.12(m). It can be seen that the illumination map of the proposed technique's result is more uniform as compared to others.

Before comparing the technique with existing techniques, work done by the above stated prime authors has been briefed in this section:

Fattal [23] proposed a technique to estimate parameters of restoration model (1.11) by assuming the fact that surface shading and transmission functions for a given foggy image are locally uncorrelated. This technique relies on the fact that whether the functions of shading and transmission are independent. Since this technique uses statistical property to estimate parameters for image restoration, the performance greatly depends on an input foggy image. Therefore, it may not work well when an image contains dense fog. He *et al.* [33] proposed a special prior called as dark channel which helps to obtain depth map of a foggy image. The dark channel produces square patches or blocks in a de-fogged image. Therefore, to perform smoothing the patches, soft matting algorithm was used for the refinement of transmission. This algorithm is very complex and time consuming. So the de-fogging process takes a long processing time. Due to the limitations of soft matting algorithm used by DCP Tarel *et al.* [114] proposed a fast image de-fogging technique by using median filtering and its variant for transmission map refinement. This technique can process color or gray scale images in real time. This technique produces over saturated results as it applies a contrast enhancement post processing step. Although, its processing time is better than that of He *et al* [33], but twice median filter applied in this technique makes it hard to use in real time. Later He *et al* [34] improved their own technique [33] by proposing a new edge preserving smoothing filter called as guided filter in place of soft matting algorithm. But some problems of halo artifacts still exists. Also, the dark channel phenomenon sometimes consider white and brighter objects as distant, therefore produce unreliable de-fogging results. Therefore, Meng *et al.* [79] proposed a de-fogging technique based upon DCP by imposing an inherent boundary constraint on the transmission estimation function. This technique has good effect on the recovery of foggy images but refined transmission map is obtained by computing number of iterations which is a time consuming process. Choi *et al.* [18] proposed a reference less evaluation-based de-fogging technique. This technique uses the fog acquainted statistical parameters and made prediction about the fog density of a given image. Drawback of this technique is that it uses number of statistical parameters to de-fog an image which can be harder to obtain in real time. The another limitation of this technique is that the closer regions of de-fogged images are darker whereas farther regions remain bright. Zhu *et al.* [136] found the fact that concentration of fog increases with increasing scene depth. By assuming that the scene depth is positively correlated with fog concentration and proposed a linear model by using the saturation and brightness of a foggy image to estimate the parameters of fog degradation model (1.11). It uses guided filter for transmission refinement which may suffer from some halo artifacts, as this filter is not able to finely characterize the image near some edges. However, the scattering coefficient in the atmospheric scattering model cannot actually be regarded as a constant therefore0 the recovered images suffer from dullness and higher illumination variations. Cai *et al.* [17] proposed a trainable end-to-end system called DehazeNet for transmission estimation, with specially designed feature extraction layers. Ren *et al.* [102] proposed a Multi-Scale Convolutional Neural Network ($MSCNN$) for learning the transmission map of a foggy image. It consists of a coarse scale network predicting a holistic transmission map and a fine-scale

network for refining the map. However, these techniques usually take convolutional neural networks to learn a mapping from input foggy images to the transmissions or fog free images, without considering fog related priors to constrain the mapping space compared with the traditional methods. Liu *et al.* [73] proposed a single image de-fogging technique using multi-scale correlated wavelet framework. This technique handles the de-fogging problem in frequency domain. It aims not only to significantly increase the perceptual visibility of a scene, but also to reduce the noise effect as well. Colores *et al.* [104] proposed a technique for single image de-fogging using an Multi Layer Perceptron to estimate the transmission map rather than RGB images as input data.

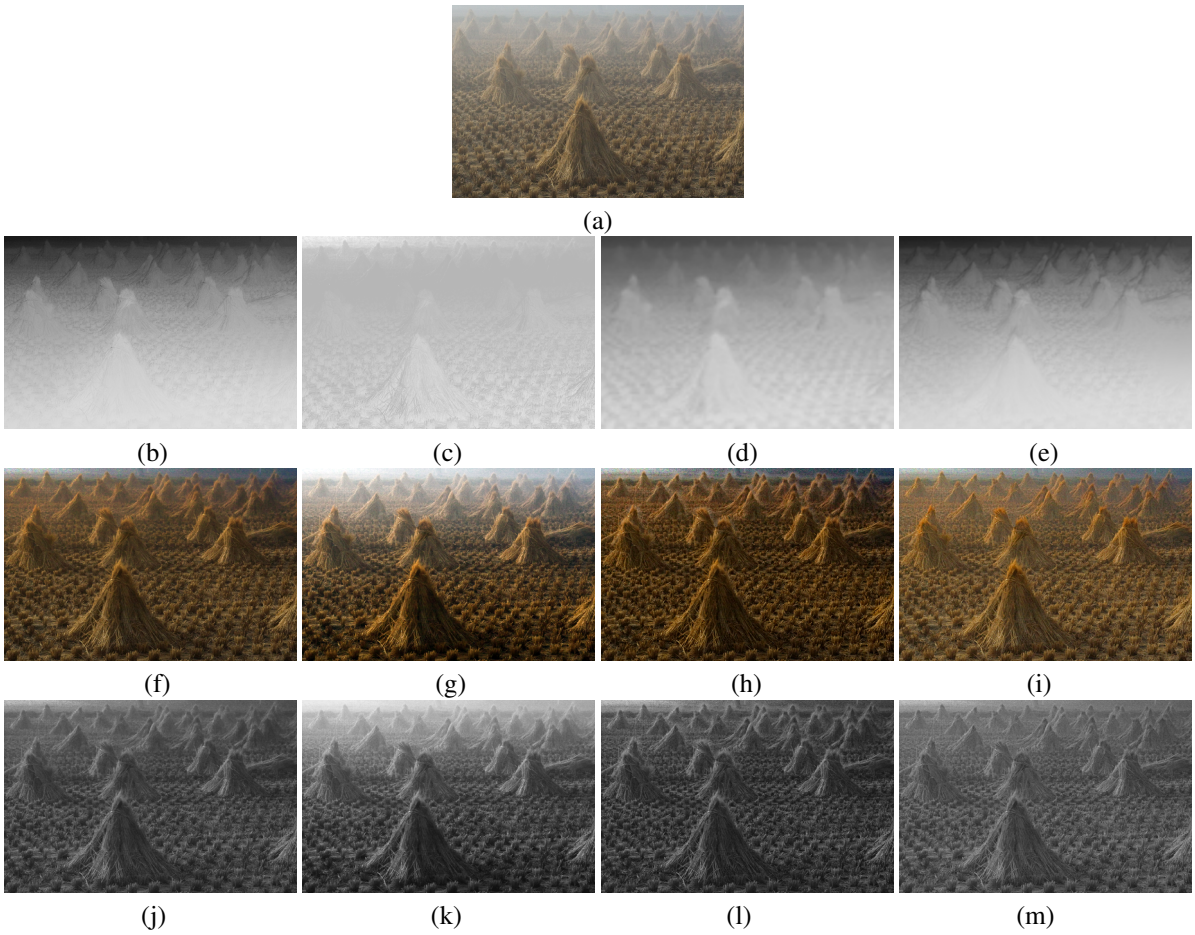

Figure 3.12: Transmission Maps (a) Input foggy image "$Cones$". (b-e) Initial Transmission maps obtained by (He *et al.*, Zhu *et al.*, Lin *et al.* and Proposed (Left-Right)). (f-i) Restored Images. (j-m) Corresponding Illumination Maps.

In Figure 3.13, the de-fogging results of proposed technique are compared with that of He's technique. Since, the technique improves He *et al's.* technique by removing the over darkness problem and enhancing edge details, can be visualized in Figure 3.13 (d and e).

In Figure 3.14, the de-fogging results of our technique are compared with that of Tarel *et al.*, He *et al.*, Cai *et al.*, Meng *et al.*, Zhu *et al.* and Liu *et al's* technique for "$City1$" image. Tarel's results are foggy around edges due to applying median filter instead of edge preserving filter. He's result is better but the over darkness problem exists due to homogeneous model based recovery, whereas Cai *et al's* machine learning based de-fogging

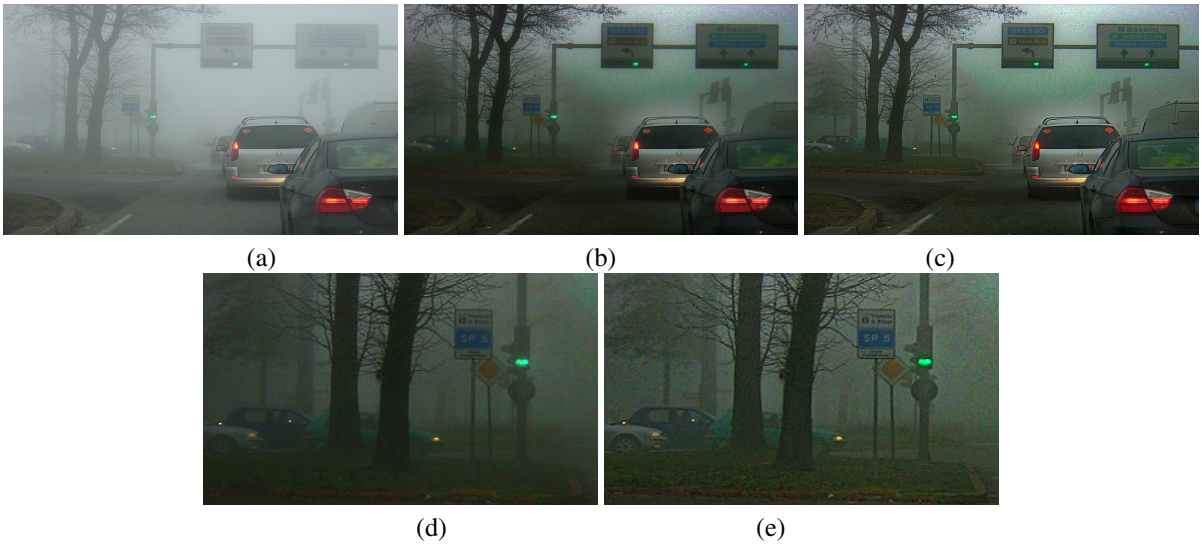

Figure 3.13: De-fogging Results (a) Input foggy image "$Foggy\_road1$" (b) De-fogging results of He *et al.* (c) Proposed Technique. (d) Portion of De-fogging results of He *et al.* (e) Portion of De-fogging results of proposed technique

technique obtains saturated results due to lack of information required in such techniques. Meng *et al's* technique improves He's technique. Its de-fogging performance is better but fine edge details are over enhanced and the image color looks unnatural. For same image, the results are also compared with Zhu *et al's* technique. It uses a linear model with supervised learning to estimate the depth map of a foggy image. Techniques based upon supervised learning require dummy foggy images for estimating the depth maps in an efficient way. However, it cannot always contain significant depth knowledge of outdoor images in practice. Therefore, this technique can not considered as reliable as shown in Figure 3.14(f). Liu *et al.* applied wavelets to improve the de-fogging results, but the recovered image looks over dark around green areas. It can be clearly observed that, the results of our technique are more bright and clear. Resultant image is comparatively clear because the texture details are filtered from the transmission map during refinement step which in result does not highlight the non edge details in the restored image and hence vagueness is avoided. The atmospheric light selection process of the technique avoids the pixels of train head lights to participate as candidates of atmospheric light, due to which unnecessary darkness is avoided. Also, the unevenness in brightness is decreased due to dynamic range extension in post processing.

In Figure 3.15, the de-fogging performance of our technique is compared with Tarel *et al.*, He *et al.*, Cai *et al.*, Meng *et al.*, Zhu *et al.* and Ren *et al's* techniques for "$Toys$" image. The de-fogging results of machine learning based techniques *i.e.* Cai *et al.* and Ren *et al.* are unreliable as described above. Meng *et al's* results looks unnatural. He's results are better than other existing techniques. But the technique improves color and edge details of He's image as shown in Figure 3.15.

Next, the de-fogging performance is compared for "$Cones$" with Fattal, Tarel *et al.*, Cai *et al.*, Choi *et al.*, Zhu *et al.* and Ren *et al's* technique. Fattal's technique [23], is based upon the assumption that transmission and surface shading are locally uncorrelated (Figure 3.16). This technique requires MRF extrapolation to calculate

the transmission of those pixels which cannot meet up with the error estimation criteria. The assumption of this technique fails in dense foggy images or when the color is vague and becomes unreliable in accurately recovering the transmission. In addition, this technique produces color distortion as shown in Figure 3.16 (b). Choi's technique is based upon reference-less prediction of fog density which leads to over enhancement and over saturation problem as seen in Figure 3.16 (e). More de-fogging results of the proposed technique can be visualized in Figures 3.17 and 3.18. It can be observed that the technique obtains consistent de-fogging results in comparison to existing compared techniques in terms of color, clarity, naturalness and scene information preservation. Moreover, in comparison to other techniques, the execution time of the our technique is significantly less which makes it suitable for real time applications.

(a) (b) (c) (d)

(e) (f) (g) (h)

Figure 3.14: De-fogging Results (a)Input foggy images "$City1$". De-fogging Results of (b) Tarel *et al.* (c) He *et al.* (d) Cai *et al.* (e) Meng *et al.* (f) Zhu *et al.* (g) Liu *et al.* (h)Proposed.

3.3.2 Objective Evaluation

The final restoration results of the proposed de-fogging technique have been compared with previous state-of-art techniques including Tarel *et al.*, He *et al.*, Meng *et al.*, Choi *et al.*, Zhu *et al.*, Cai *et al.*, Ren *et al.*, Liu *et al.* and Colores *et al.*. For comparison, 15 standard foggy images have been taken from databases [19] and [74]. To ensure comparability of various de-fogging techniques, descriptive variables or metrics for judging the output image quality are necessary. In this work, six different quality parameters including r, CNI, FRF, VCM, CI

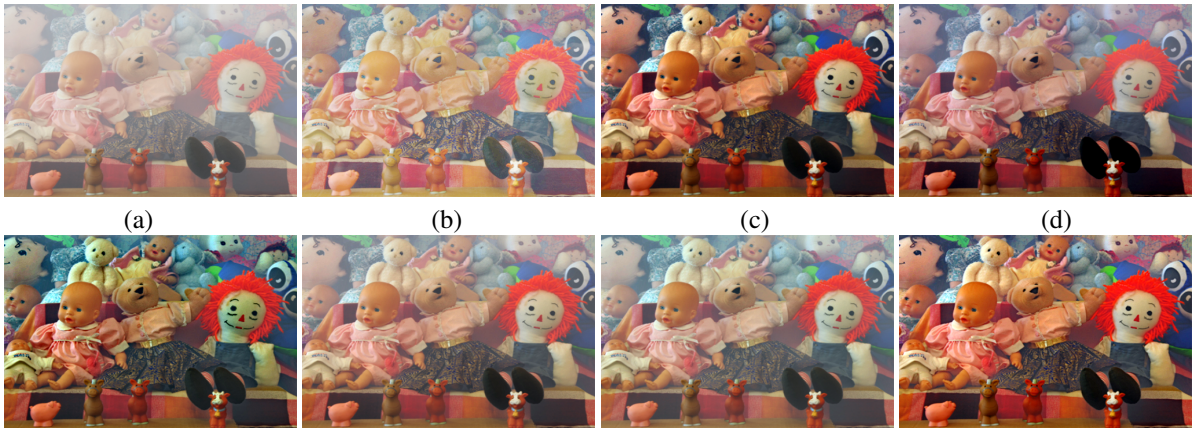

(a) (b) (c) (d)

(e) (f) (g) (h)

Figure 3.15: De-fogging Results (a)Input foggy images "$Toys$". De-fogging Results of (b) Tarel *et al.* (c) He *et al.* (d) Cai *et al.* (e) Meng *et al.* (f) Zhu *et al.* (g) Ren *et al.* (h) Proposed.

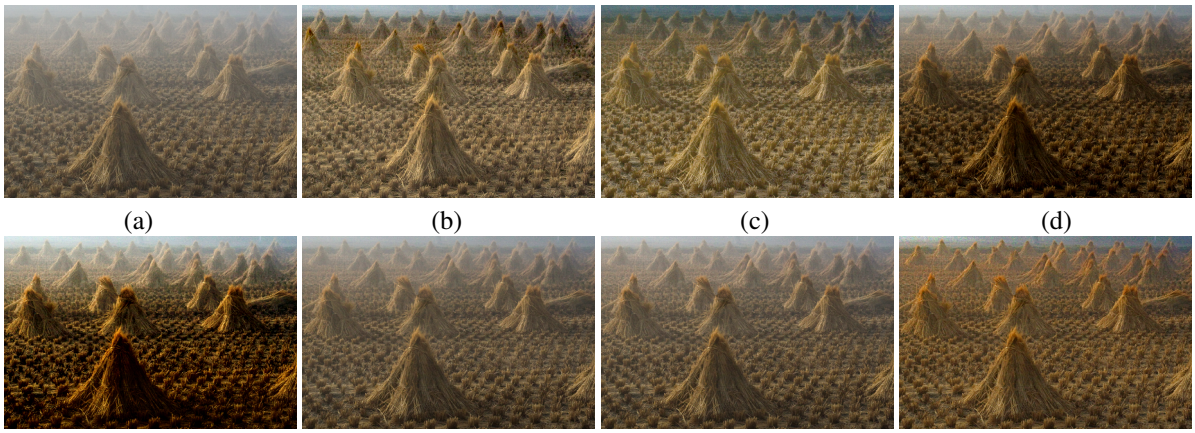

(a) (b) (c) (d)

(e) (f) (g) (h)

Figure 3.16: De-fogging Results (a)Input foggy images "$Cones$". De-fogging Results of (b) Fattal (c) Tarel *et al.* (d) Cai *et al.* (e) Choi *et al.* (f) Zhu *et al.* (g) Ren *et al.* (h) Proposed.

(a) (b) (c) (d)

Figure 3.17: De-fogging Results (a)Input foggy images "$Foggy\_road2$" (top), "$Foggy\_ground$" (bottom). De-fogging Results of (b) He *et al.* (c) Zhu *et al.* (d) Proposed.

and CIE have been considered as shown in Tables 3.2-3.7. A better de-fogging technique achieves higher values of all the above factors and takes lesser time to execute.

(a) (b) (c) (d)

Figure 3.18: De-fogging Results (a) Input foggy images "$Cityscape$" (top) and "$People$" (bottom). De-fogging results of (b) Ren *et al.* (c) Liu *et al.* (d) Proposed Technique.

From the Tables 3.2-3.7, it can be seen that Tarel *et al's* and proposed technique obtains equivalent r, CNI and FRF. At the same time, our technique obtains better VCM, CI and CIE than that of Tarel *et al.*. The technique produces better r as compared to other techniques except Meng *et al.* CI of the technique is almost double than that of Meng *et al.*. In terms of FRF, Choi *et al.*, Cai *et al.* and Liu *et al's* techniques outperform the proposed technique but at the same time, their performance lacks in other parameters. The proposed technique obtains significantly high values for all the six parameters simultaneously, not compromising one at the cost of other. Since the proposed technique aims at improving the basic DCP technique [34], the percentage improvement with respect to DCP technique is 35.33% in r, 4.41% in CNI, 13.87% in VCM, 45.59% in CI, 1.52% in CIE. However, there is a decrease in FRF by 1.09% which is almost insignificant in comparison to the other improvements. Also the maximum percentage improvement achieved by proposed technique with respect to existing techniques is 76.52% in r, 14.51% CNI, 76.69% in FRF, 16.71% VCM, 88.51% CI, 6.05% in CIE and the minimum percentage improvement is 28.48% in r, 4.41% CNI, 0.55% in FRF, 5.13% VCM, 28.17% CI, 0.82% in CIE. Results of the our technique appear more natural because the atmospheric light is not affected from unwanted bright light sources. Since the foggy image is affected by the environment lightening, some parts of the de-fogged image may suffer from low brightness and due to dark channel prior based image restoration, de-fogged images may be even more darker. Therefore, in the proposed technique, the under exposed (low contrast) regions are identified and an adaptive approach is used to enhance such regions without making any color distortion. This makes the de-fogged images of the technique look more natural and uniform in brightness. In comparison to all, the technique produces natural, better contrast images with good edge recovery. Overall, the proposed technique produces visually good results as perceived form the parameters. Also, it can be applied in real time applications due to its higher processing speed in comparison to others.

Table 3.2: Comparison of the proposed technique with existing techniques on the basis of r

	Tarel *et al.* [114]	He *et al.* [34]	Meng *et al.* [79]	Choi *et al.* [18]	Zhu *et al.* [136]	Cai *et al.* [17]	Ren *et al.* [102]	Liu *et al.* [73]	Colores *et al.* [104]	Proposed
City1	2.21	1.37	2.03	1.61	1.14	1.14	1.17	1.35	1.14	1.70
Night1	2.69	0.71	1.12	1.20	0.86	0.64	0.94	1.15	1.02	1.75
Landscape3	1.34	1.00	1.13	1.35	1.08	0.94	1.09	1.06	1.07	1.18
Foggy_building1	2.31	1.67	3.18	1.39	1.22	1.27	1.23	1.79	1.20	2.42
Foggy_road1	2.31	1.49	2.36	1.78	1.24	1.08	1.45	1.69	1.30	2.37
Foggy_road2	2.28	1.48	2.56	1.43	1.14	1.01	1.17	1.35	1.12	2.02
Cones	1.88	1.59	1.61	1.66	1.13	1.38	1.22	1.35	1.20	1.62
Cityscape	5.08	3.68	5.18	1.88	1.47	1.81	1.79	3.13	1.55	3.47
Foggy_ground	2.99	1.23	2.44	2.13	1.16	1.25	1.30	1.46	1.21	1.94
People	1.81	1.16	1.37	1.42	1.11	1.07	1.10	1.29	1.25	1.37
Foggy_building2	1.86	1.33	2.78	1.29	1.04	1.10	1.50	1.62	1.23	3.63
Toys	2.04	2.05	2.34	1.95	1.51	1.62	1.52	2.19	1.51	2.26
Y1	1.66	1.24	1.35	1.53	1.13	0.94	1.10	1.27	1.10	1.56
Y16	1.88	1.44	1.67	1.48	1.22	1.19	1.33	1.53	1.35	1.64
Aerial	1.82	1.04	1.46	1.67	1.06	0.76	1.17	1.27	1.09	1.52
Average	**2.28**	**1.50**	**2.17**	**1.58**	**1.17**	**1.15**	**1.27**	**1.57**	**1.22**	**2.03**

Table 3.3: Comparison of the proposed technique with existing techniques on the basis of CNI

	Tarel *et al.* [114]	He *et al.* [34]	Meng *et al.* [79]	Choi *et al.* [18]	Zhu *et al.* [136]	Cai *et al.* [17]	Ren *et al.* [102]	Liu *et al.* [73]	Colores *et al.* [104]	Proposed
City1	0.62	0.54	0.53	0.58	0.50	0.53	0.53	0.58	0.52	0.55
Night1	0.92	0.77	0.78	0.78	0.68	0.79	0.66	0.95	0.66	0.91
Landscape3	0.97	0.96	0.92	0.99	0.93	0.98	0.49	0.97	0.94	0.97
Foggy_building1	0.74	0.63	0.54	0.45	0.45	0.47	0.53	0.52	0.44	0.63
Foggy_road1	0.61	0.52	0.51	0.62	0.48	1.00	0.51	0.50	0.44	0.52
Foggy_road2	0.57	0.50	0.52	0.51	0.48	0.46	0.51	0.47	0.48	0.51
Cones	0.731	0.73	0.69	0.80	0.57	0.73	0.60	0.81	0.63	0.93
Cityscape	0.59	0.57	0.60	0.53	0.54	0.42	0.61	0.58	0.58	0.57
Foggy_ground	0.79	0.59	0.57	0.51	0.53	0.59	0.59	0.62	0.55	0.59
People	0.89	0.83	0.89	0.88	0.67	0.67	0.79	0.82	0.67	0.85
Foggy_building2	0.85	0.97	0.83	1.00	0.75	0.63	0.64	0.97	0.63	0.98
Toys	0.73	0.85	0.82	0.76	0.68	0.65	0.63	0.85	0.64	0.85
Y1	0.74	0.46	0.65	0.25	0.75	0.75	0.81	0.29	0.74	0.43
Y16	0.78	0.63	0.76	0.63	0.86	0.94	0.73	0.50	0.78	0.76
Aerial	0.79	0.69	0.64	0.70	0.57	0.64	0.54	0.70	0.55	0.75
Average	**0.75**	**0.68**	**0.68**	**0.67**	**0.63**	**0.68**	**0.61**	**0.68**	**0.62**	**0.72**

Table 3.4: Comparison of the proposed technique with existing techniques on the basis of FRF

	Tarel *et al.* [114]	He *et al.* [34]	Meng *et al.* [79]	Choi *et al.* [18]	Zhu *et al.* [136]	Cai *et al.* [17]	Ren *et al.* [102]	Liu *et al.* [73]	Colores *et al.* [104]	Proposed
City1	1.35	1.19	1.38	2.33	0.72	2.75	1.89	1.75	0.68	1.23
Night1	2.15	1.61	1.61	2.11	2.15	2.90	0.20	2.47	1.62	1.53
Landscape3	0.51	0.53	0.38	0.62	0.62	1.12	-2.23	0.61	0.44	0.53
Foggy_building1	3.06	3.25	3.37	4.85	1.53	3.75	3.7	3.34	1.27	3.35
Foggy_road1	2.40	2.26	2.16	3.71	1.05	3.82	1.47	2.94	1.07	2.37
Foggy_road2	1.71	1.61	1.64	2.86	1.49	2.87	1.11	2.26	0.91	1.68
Cones	1.37	1.74	1.54	2.27	0.85	1.94	0.88	2.03	1.08	1.72
Cityscape	2.58	2.66	2.96	3.04	1.15	2.04	1.89	2.46	1.42	2.62
Foggy_ground	3.69	3.35	2.81	3.38	1.82	4.26	1.26	3.81	1.60	3.47
People	0.93	0.91	1.09	2.02	0.53	1.40	0.97	1.08	0.75	0.94
Foggy_building2	2.83	2.45	2.26	2.62	1.68	1.60	1.41	2.62	1.16	2.23
Toys	1.12	2.04	1.98	2.02	1.24	1.73	1.13	2.13	1.05	2.06
Y1	1.17	1.58	1.47	1.63	1.17	2.25	0.91	1.71	0.93	1.48
Y16	0.89	0.94	1.06	1.41	0.76	0.72	0.96	1.20	0.73	0.90
Aerial	1.41	1.11	0.99	1.77	1.01	2.07	0.73	1.40	0.72	1.17
Average	**1.81**	**1.82**	**1.78**	**2.44**	**1.18**	**2.35**	**1.08**	**2.12**	**1.03**	**1.82**

Table 3.5: Comparison of the proposed technique with existing techniques on the basis of VCM

	Tarel *et al.* [114]	He *et al.* [34]	Meng *et al.* [79]	Choi *et al.* [18]	Zhu *et al.* [136]	Cai *et al.* [17]	Ren *et al.* [102]	Liu *et al.* [73]	Colores *et al.* [104]	Proposed
City1	68.83	46.00	54.17	66.00	45.83	50.67	19.50	56.33	45.00	54.83
Night1	37.00	30.17	42.67	53.50	37.50	29.33	54.33	52.50	43.50	30.00
Landscape3	48.59	45.78	49.06	51.56	47.97	45.00	20.63	47.97	47.19	48.13
Foggy_building1	35.50	21.33	32.33	49.83	48.17	52.00	57.17	34.17	47.17	31.67
Foggy_road1	28.65	29.81	37.12	35.77	53.65	58.08	49.42	36.54	24.42	36.73
Foggy_road2	48.27	25.38	35.77	40.00	27.50	26.92	52.50	34.81	25.58	33.08
Cones	67.98	61.40	69.08	75.44	47.81	56.80	49.34	63.60	47.59	61.62
Cityscape	56.62	58.98	73.87	37.39	59.17	33.58	31.58	52.45	57.35	52.99
Foggy_ground	43.57	30.54	36.07	47.50	29.11	30.71	28.04	31.07	27.68	35.36
People	86.60	79.43	76.56	83.97	76.32	75.84	75.12	81.34	77.03	79.19
Foggy_building2	38.60	23.31	39.10	21.05	45.36	50.88	30.83	33.83	56.64	61.90
Toys	55.56	69.01	70.96	67.06	50.88	53.61	53.22	72.71	49.71	70.76
Y1	59.92	51.42	52.43	57.89	46.76	41.30	45.95	53.24	44.13	57.09
Y16	70.65	70.45	70.24	70.45	65.59	64.37	68.42	70.45	67.81	72.06
Aerial	38.35	18.61	34.96	49.62	15.98	47.56	22.93	34.77	18.23	28.01
Average	**52.31**	**44.11**	**51.63**	**53.80**	**46.51**	**47.78**	**43.93**	**50.39**	**45.27**	**50.23**

Table 3.6: Comparison of the proposed technique with existing techniques on the basis of CI

	Tarel *et al.* [114]	He *et al.* [34]	Meng *et al.* [79]	Choi *et al.* [18]	Zhu *et al.* [136]	Cai *et al.* [17]	Ren *et al.* [102]	Liu *et al.* [73]	Colores *et al.* [104]	Proposed
City1	23.36	13.47	14.91	16.83	11.65	13.35	11.84	13.84	12.07	34.75
Night1	52.77	28.19	26.30	33.66	24.74	26.82	21.01	41.14	26.37	31.16
Landscape3	67.44	61.99	62.03	79.47	59.47	63.99	61.17	62.79	59.97	67.44
Foggy_building1	29.69	19.93	19.34	16.73	11.17	12.13	10.38	15.01	10.61	39.37
Foggy_road1	33.72	20.76	21.97	27.99	18.14	48.28	18.81	21.57	18.00	49.74
Foggy_road2	40.03	28.98	30.73	28.77	26.72	27.97	26.61	30.19	27.28	53.68
Cones	31.44	28.66	27.72	42.40	22.69	30.15	23.32	31.64	24.82	60.08
Cityscape	36.61	26.12	29.45	19.81	18.00	21.05	21.99	24.64	20.01	46.99
Foggy_ground	40.69	21.83	24.11	20.52	14.10	14.28	13.30	17.13	13.36	85.57
People	44.51	40.63	45.28	54.77	32.86	37.34	35.15	38.87	40.25	66.59
Foggy_building2	51.91	30.03	29.16	47.85	25.08	20.72	20.65	30.52	20.52	60.34
Toys	54.34	75.28	67.82	69.65	60.14	58.66	52.20	77.57	51.33	91.64
Y1	77.30	98.66	85.31	97.35	81.44	47.84	68.40	102.83	63.80	79.14
Y16	88.63	101.54	82.17	95.48	79.19	53.52	75.37	104.10	73.00	75.37
Aerial	41.78	32.62	32.82	38.46	26.53	28.83	25.28	32.39	25.27	73.47
Average	**47.61**	**41.91**	**39.94**	**45.98**	**34.13**	**33.66**	**32.37**	**42.95**	**32.44**	**61.02**

Table 3.7: Comparison of the proposed technique with existing techniques on the basis of CIE

	Tarel *et al.* [114]	He *et al.* [34]	Meng *et al.* [79]	Choi *et al.* [18]	Zhu *et al.* [136]	Cai *et al.* [17]	Ren *et al.* [102]	Liu *et al.* [73]	Colores *et al.* [104]	Proposed
	7.03	7.32	7.22	7.41	7.29	7.07	7.37	7.45	7.27	7.22
Night1	7.26	6.46	6.43	7.09	6.50	4.83	7.00	6.75	7.18	6.78
Landscape3	7.65	7.46	7.45	7.45	7.36	6.33	7.45	7.45	7.46	7.71
Foggy_building1	7.24	7.24	7.39	7.09	7.68	7.75	7.59	7.83	7.69	7.19
Foggy_road1	7.06	7.17	6.99	6.73	7.41	6.77	7.40	7.32	7.43	7.47
Foggy_road2	7.36	7.51	7.41	6.97	7.66	7.04	7.77	7.47	7.73	6.85
Cones	7.02	7.01	6.98	6.97	7.18	7.25	7.22	7.15	7.28	7.83
Cityscape	6.75	7.33	7.40	6.52	6.94	7.31	7.22	7.57	7.09	6.85
Foggy_ground	7.28	6.75	6.55	7.06	6.90	6.47	7.13	6.64	7.22	7.41
People	7.53	7.58	7.33	7.01	7.59	7.39	7.61	7.64	7.62	7.71
Foggy_building2	7.28	6.93	7.20	7.09	6.87	7.32	7.46	7.19	7.30	7.22
Toys	7.32	7.79	7.62	7.74	7.62	7.69	7.52	7.83	7.61	7.59
Y1	7.53	7.50	7.43	7.22	7.47	7.27	7.53	7.44	7.61	7.70
Y16	7.66	7.68	7.82	7.45	7.77	7.75	7.90	7.67	7.78	7.51
Aerial	7.08	6.98	6.92	7.07	7.29	5.93	7.55	7.02	7.49	7.36
Average	**7.27**	**7.25**	**7.21**	**7.12**	**7.30**	**6.94**	**7.45**	**7.36**	**7.45**	**7.36**

3.3.3 Execution Time Comparison

The proposed technique uses fast guided filter for transmission map refinement which is an edge preserving smoothening filter [35]. The time response of various smoothening filters for transmission map refinement is analyzed in this section. Table 3.8 shows the execution time of the overall de-fogging process when employed with various smoothening filters including bilateral filter, joint bilateral filter, guided filter and fast guided filter. To show the experiments, the technique has been used except at the transmission refinement step. The time taken by employing $Guided\ filtering$ for 600×400 image is 0.21 seconds. Whereas $Fast\ Guided\ filter$ takes 0.10 seconds. The fast guided filter is implemented by performing all the steps of guided filter on down sampled images and reduced filter size. As per He *et al.* [35], bilinear interpolation is used for sampling. It uses weighted average of four neighboring pixel values which simply involves basic mathematical operations. However sampling operations require a little time overhead, but this is not significant in front of total time saved for performing guided filtering which can also be observed in Table 3.8. It can be observed that among all the filters, the performance of fast guided filter is best.

Table 3.8: Comparison of mean execution time (in seconds) response of various smoothening filters for transmission map refinement for 600×400 image.

	DCP+ Bilateral filter	DCP+ Joint bilateral filter	DCP+ Guided Filter	DCP+ Fast Guided Filter
Execution time	5.12	6.01	0.21	0.10

Apart from the response of various smoothening filters, the time comparison of the proposed technique with other existing techniques has also been shown in Table 3.9. For this comparison, image size, tools used for implementing the technique (*i.e* C++, MATLAB or Not Mentioned) and the type of processor are considered for each of the technique.

It can be clearly noted from Table 3.9 that the processing speed of the technique is better than all other techniques listed, which shows it is computational effective. At the same time, other parameters of quality have not been compromised, as shown in Tables 3.2-3.7. Therefore, it can be concluded that the technique is better in achieving high speed along with maintaining the overall image quality.

Table 3.9: Comparison of execution time of the proposed technique with existing techniques

Technique	**Processor**	**Tool**	**Image Size**	**Execution Time**
Tan [112]	Pentium 4	N/A	600×400	5-7min
Fattal [23]	Dual-Core	C++	512×512	35s
Tarel *et al.* [114]	Quad-Core	MATLAB	600×400	5.9s
He *et al.* [34]	Quad-Core	MATLAB	600×400	1.99s
Meng *et al.* [79]	Quad-Core	MATLAB	600×400	1.80s
Choi *et al.* [18]	Quad-Core	MATLAB	600×400	12.52s
Zhu *et al.* [136]	Quad-Core	MATLAB	600×400	0.69s
Cai *et al.* [17]	Quad-Core	MATLAB	600×400	2.00s
Ren *et al.* [102]	Quad-Core	MATLAB	600×400	1.81s
Liu *et al.* [73]	Quad-Core	MATLAB	600×400	0.25s
Proposed	Quad-Core	MATLAB	600×400	0.10s

3.3.4 De-fogging Results on *FRIDA* with varying Fog Density

The objective quality parameters including r, CNI, FRF, VCM, CI, CIE have been shown for standard foggy images which shows that the proposed technique obtains better quality de-fogged images and also effective for applying in real time scenarios. In this section, the parameters have been evaluated on $FRIDA$ [115] which is a dynamic database containing 66 images. By using the original clear day images, depth maps present in this database, different foggy images can be generated by varying the value of β as shown in Figure 3.19. The de-fogging results obtained by existing techniques is shown in Figure 3.20. In Table 3.10, the average data for 330 images (generated from 66 individual images and 5 different β values) for r, CNI, FRF, VCM, CI, CIE has been shown.

From Table 3.10, it can be seen that percentage improvement of the proposed technique with respect to DCP technique is 26.65% in r, 0% in CNI, 5.72% in FRF, 4.75% in VCM and 0.47% in CE, whereas a decrease of 0.89% in CI which is comparatively very less. Also the maximum percentage improvement achieved by the technique with respect to existing techniques is 60.81% in r, 14.29% CNI, 177.42% in FRF, 25.96% VCM, 7.09% CI, 2.26% in CIE. The minimum percentage improvement achieved by the technique with respect to existing techniques is 1.28% in r, 5.66% CNI, 2.69% in FRF, 4.75% in VCM, 3.19% in CI, 0.17% in CIE. Overall, the technique produces visually good results as perceived form the parameter in case of foggy road image database [115] also.

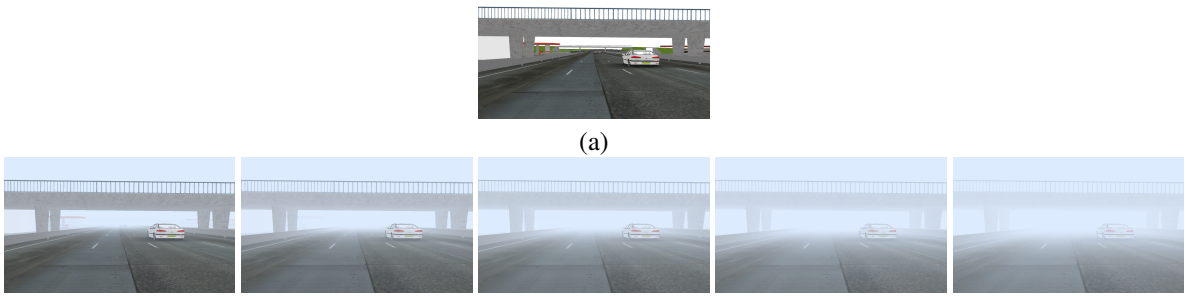

(a)

(b) (c) (d) (e) (f)

Figure 3.19: Foggy image wih varying fog density. (a) Clear image of $FRIDA$. Foggy images obtained by using (b) $\beta = 0.02$ (c) $\beta = 0.04$ (d) $\beta = 0.06$ (e) $\beta = 0.08$ (f) $\beta = 0.1$

Table 3.10: Comparison of r, CNI, FRF, VCM, CI and CIE of the proposed technique with existing techniques on $FRIDA(66\ Images)$ with varying fog density ($\beta = 0.02,\ 0.04, 0.06,\ 0.08, 0.1$)

	r	**CNI**	**FRF**	**VCM**	**CI**	**CIE**
Tarel *et al.* [114]	2.35	0.81	3.58	34.08	43.11	5.96
He *et al.* [34]	1.88	0.56	3.25	37.89	19.21	5.94
Cai *et al.* [17]	1.64	0.53	2.85	36.80	19.72	6.10
Choi *et al.* [18]	1.58	0.85	4.74	34.88	33.16	7.10
Meng *et al.* [79]	3.00	0.56	3.35	39.97	23.08	5.90
Zhu *et al.* [136]	1.52	0.51	1.64	33.24	17.98	6.08
Ren *et al.* [102]	1.58	0.50	1.28	31.85	18.08	5.84
Liu *et al.* [73]	2.22	0.56	3.93	40.82	18.45	6.21
Colores *et al.* [104]	1.48	0.49	1.24	31.51	17.78	6.05
Proposed	2.38	0.56	3.44	39.69	19.04	5.97

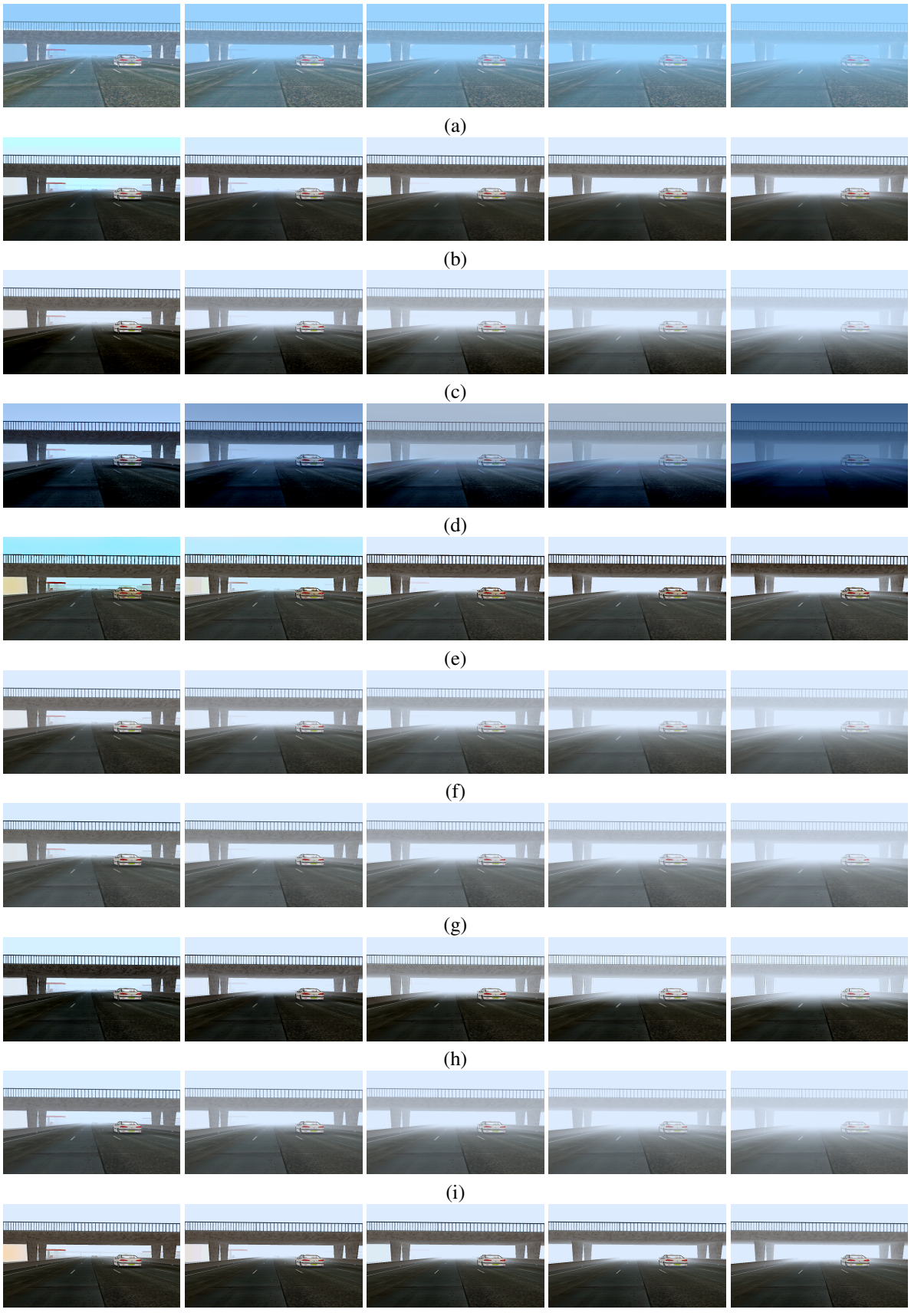

Figure 3.20: Output de-fogged images of $FRIDA$ with $\beta = 0.02,\ 0.04,\ 0.06, 0.08,\ 0.1$ (left-right) obtained by (a) Tarel (b) He (c) Cai (d) Choi (e) Meng (f) Zhu (g) Ren (h) Liu (i) Colores (j) Proposed

3.4 Conclusion of the Chapter

In this chapter, a novel image subsampling approach to preserve local minima in a image patch is proposed. The subsampled image is used for dark channel estimation. The technique constructs dark channel of a given image around 15 times faster than normal dark channel construction process without causing any degradation in visual quality of the de-fogged image. To further accelerate the de-fogging process, the atmospheric light has been found from top 25% image rows after filtering out bright light sources or regions. The percentage improvement attained by the technique in comparison to DCP technique is 34.19% in r, 4.41% in CNI, 13.87% in VCM, 45.59% in CI, 15.17% in CIE. Also the maximum percentage improvement achieved by the technique with respect to compared existing techniques is 74.79% in r, 14.51% CNI, 76.69% in FRF, 16.70% VCM, 88.51% CI, 6.05% in CIE and the minimum percentage improvement is 28.39% in r, 4.41% CNI, 0.55% in FRF, 5.13% VCM, 28.16% CI, 0.82% in CIE. For $FRIDA$ database, that percentage improvement of the technique with respect to DCP technique is 26.65% in r, 0% in CNI, 5.72% in FRF, 4.75% in VCM and 0.47% in CE. Also the maximum percentage improvement achieved by technique with respect to existing techniques is 60.81% in r, 14.29% CNI, 177.42% in FRF, 25.96% VCM, 7.09% CI, 2.26% in CIE and the minimum percentage improvement is 1.28% in r, 5.66% CNI, 2.69% in FRF, 4.75% in VCM, 3.19% in CI, 0.17% in CIE. The overall experimental results show that the technique performs well for various images by adaptively estimating atmospheric light and can be applied to real time applications due to high processing speed. 00

Chapter 4

Color Attenuation Prior based Image De-fogging

4.1 Introduction

In this Chapter, a de-fogging technique based upon CAP has been proposed. CAP uses a linear model to learn the parameters with a supervised learning method for estimating the scene depth map of a foggy image. This depth map is utilized for transmission map estimation. In the work, to quickly and accurately estimate the transmission map, a sub-sampling based local minimum operation and fast $GDGF$ is applied on CAP based initial depth map. The edge attentive restraints of $GDGF$ make edges to be conserved better in de-fogged images. The images obtained by CAP technique suffer from dullness and higher illumination variations due to consideration of fog image degradation model in homogeneous environment and a constant value of atmospheric light. Such variations are removed in the work by using Lambert's law of illumination reflection, which helps to compensate non uniform illumination. This causes simultaneous dynamic range modification, color consistency and lightness rendition without producing the artifacts in a de-fogged image. To improve the processing speed, image sub-sampling mechanism is used in various steps of image de-fogging. The sub-sampling is used in such a way that the quality of the output at any step is not compromised as demonstrated through various quality parameters. Experimental results show that our approach outperforms state-of-the-art fog removal techniques in terms of efficiency and the de-fogging effect. [†]

[†]**Contents of the work presented in this Chapter have been published in *Journal of Multimedia Tools and Applications*, Vol. 79, pp. 12069-12091, 2020, Impact Factor=2.101 (SCI Indexed)**

4.2 Background

As the input foggy image reveals a very small amount of scene detail information, it is challenging to detect and extract fog from a given image. Zhu *et al.* observed that saturation and brightness of a foggy image change strongly with changing fog concentration. In general, the concentration of fog increases with increasing scene depth. By assuming that the scene depth is positively correlated with fog concentration, Zhu *et al.* proposed following linear model to estimate the parameters of fog degradation model to recover a foggy image:

$$d(x) = \theta_0 + \theta_1 \times v(x) + \theta_2 \times s(x) + \epsilon_0(x)$$

One of the main importance of this model is its edge preservation nature. This technique is based on the difference between brightness and saturation of the pixels within a foggy image. It creates a linear model for the scene depth of the foggy image and uses it to learn the parameters of a supervised learning. By using this, the depth information can be well recovered and the scene radiance of a foggy image can be recovered easily. This technique produces good quality de-fogged images but still has some limitations. As it estimates initial depth map by using brightness and saturation maps of an input image which tends to consider the white scene objects being distant and therefore applies 15×15 window based minimum operation to consider each pixel in the neighborhood. This requires total $225 \times M \times N$ ($M \times N$ image) operations which takes a longer processing time. Also, to refine the initial depth map, GF is used which is a well known smoothening filter and preserve edges in the image. Although, this filter is efficient in recovering image edges, but in case of fine edge details, it does not work properly [64]. In reality, the foggy image may be influenced from different lightening sources present in the atmosphere. But, CAP considers fog image degradation model in homogeneous environment and a constant value of atmospheric light is used to recover entire image pixels according to (1.37). Due to this, the recovered image contains dullness or illumination variations which is another shortcoming of this technique. In this work, these limitations have been dealt in such a way that the time complexity of the whole image de-fogging process is not compromised as explained in the next section.

4.3 Proposed *CAP* based Image De-fogging Technique

In this section, the overall proposed technique is discussed which addresses above described limitations of CAP. The window based operation applied in (1.36) is a computational expensive task because it finds the local minimum values independently for each pixel. For depth map refinement, Zhu *et al.* used GF, which is a well known smoothing filter with edge-preserving property and low time complexity. However, this filter may not represent the image near fine edges. Also, the de-fogging results of CAP suffer from illumination variations and hence make the final images look diminished or dull. These limitations have been addressed in this work as following:

(i) In this work, to refine the depth map, $GDGF$ is used instead of GF, which incorporates explicit first-order edge attentive constraints to better recover the edges in de-fogged images.

(ii) To compensate non uniform illumination variations in a de-fogged image, the initial de-fogging results are modified with the help of bright channel prior and illumination reflection model.

(iii) To reduce the execution time, image sub-sampling mechanism is used in different ways at different steps without compromising the quality and constraints of image de-fogging.

iii.a Minimum preserving sub-sampling is applied to estimate the initial depth map using CAP.

iii.b $GDGF$ is modified by using bilinear sub-sampling inspired from fast GF.

iii.c Maximum preserving sub-sampling is applied to estimate the bright channel prior for non-uniform illumination compensation.

Figure 4.1 shows the block diagram of the proposed CAP based image de-fogging technique. Since the technique is the improvement of CAP which is a model (1.11) based de-fogging technique. It involves estimation of two parameters *i.e.* L_A and $d(x)/t(x)$. By using the foggy input image, initial depth map d is obtained by using CAP. Patch based depth map is then obtained by applying minimum preserving sub-sampling mechanism described in Section 4.3.1. The edge preserving smoothening of depth map is performed by using $GDGF$ described in Section 4.3.2. Inspired from [35], $GDGF$ is implemented using down sampling the input and guidance images to reduce the execution time. Global atmospheric light is found from the top 25% image rows as explained in Section 4.3.3. The de-fogged image is then obtained by using (1.37). This image may suffer from dullness and higher illumination variations. Such variations are removed in this work by using Lambert's law of illumination reaction. This helps to compensate non uniform illumination and causes simultaneous dynamic range modification, color consistency, and lightness rendition without producing the artifacts in a de-fogged image as explained in Section 4.3.4.

4.3.1 Initial Depth Map Estimation

In the proposed work, initial depth map is estimated by using (1.35). This depth estimation may fail in some cases like for the case of white objects [136] *etc.* For such objects, the brightness values are usually high and the saturation values are low. Therefore, direct depth d estimated using (1.35) may consider white objects as the distant ones. So, the depth d is modified by local neighborhood in Zhu *et al's* technique as

$$d_{\Omega}(x) = min_{y \in \Omega(x)} d(y) \tag{4.1}$$

Where $d_{\Omega}(x)$ is a local neighborhood raw depth at location x with window $\Omega(x)$ having size $W \times W$ centered at x. According to (4.1), to estimate the whole depth map for $M \times N$ pixels in an image, $W^2 \times M \times N$ operations are

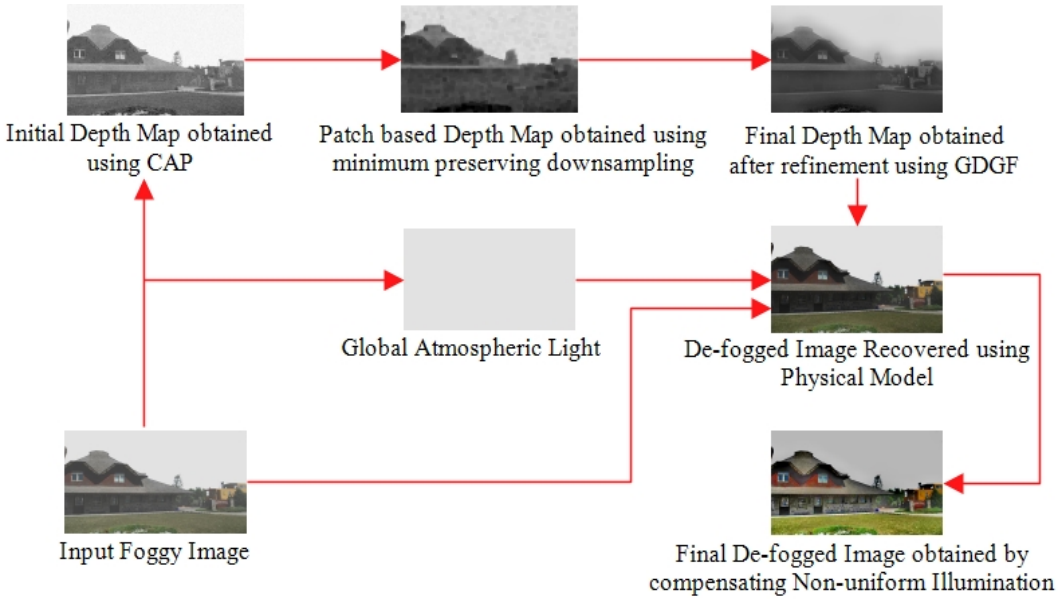

Figure 4.1: Block Diagram of CAP based De-fogging Technique

required. Therefore, in this work, inspired from Kansal *et al.* [56], we estimate the above window based depth map using the image down sampling mechanism so that the total operations can be minimized using a down sampled image. Down sampling is applied in such a way that most of the local minimums of the image are preserved in the resultant depth map.

To find dark channel of a given image, for each pixel, a minimum value is obtained from its surrounding pixels in a 3D square window of RGB color channels. This dark channel image contains redundant values as shown in Figure 3.3, therefore in this work, dark channel is estimated in such a way that the redundant calculations are reduced and the idea of preserving local minimum values in a window also holds. Following are the steps to obtain window based depth d_Ω using the initial depth map d:

- An initial depth map d obtained using (1.35) having size $M \times N$, is divided into non overlapping s_b blocks of fixed size (B_1, B_2.., B_i.....B_{s_b}) as shown in Figure 4.2. Here size of blocks is taken as 5×5.

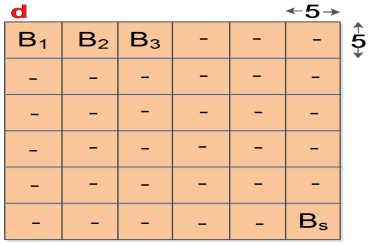

Figure 4.2: Division of depth map d into fixed size blocks.

- Then, a down sampled depth image d_{ds} is created in such a way that each pixel in d_{ds} is obtained from each

block B_i by taking the minimum in the respective block as

$$d_{ds}(x) = min(B_i), \quad i = 1, 2, 3, ...s\_b \tag{4.2}$$

The number of pixels in d_{ds} is equal to s_b. Here min specifies the mathematical operation to find the minimum depth value in a block B_i.

- After obtaining d_{ds}, its window based dark image d_{ds}^{dark} is estimated as

$$d_{ds}^{dark}(x) = min_{y \in \Omega(x)}(d_{ds}(y)) \tag{4.3}$$

Here Ω is the window of size 3×3.

- After this, nearest neighbor up sampling of d_{ds}^{dark} is performed to obtain the equivalent window based depth map d_{Ω}. Now, this depth map will be further refined as described in the next section for depth map estimation.

4.3.2 Depth Map Refinement with fast Gradient Domain Guided Filter

Guided filter is an image smoothing filter having the special property of preserving the edges. It is also well known for its low computational cost. However, a GF is miserable to halo artifacts as it uses a local linear model for an image representation which may not preserve edges cleanly. Kou *et al.* [64] proposed a modification in GF called as $GDGF$. In this, first order edge awareness constraints are incorporated in GF which helps to better preserve edges in a smoothed image. In GF, no specific constraints were applied to handle the gradient. Therefore, in some cases, it becomes difficult to preserve the edges. The filtered results obtained by $GDGF$ are closer to an input image around the edges. Therefore, in this, the edges are better preserved in comparison to GF. The cost function of $GDGF$ is represented as

$$E(a_x, b_x) = \sum_{i \in \omega(x)} [(a_x \times I_g(i) + b_x - d_x)^2 + \frac{\epsilon}{\Gamma_{I_g,x}}(a_x - \gamma_x)^2] \tag{4.4}$$

$$\gamma_x = 1 - \frac{1}{1 + e^{\psi_x}}, \quad \psi_x = \frac{4 \times (S_x - \theta_S)}{\theta_S - min(S)} \tag{4.5}$$

$$\Gamma_{I_g,x} = \frac{1}{N} \sum_{i=1}^{N_p} \frac{S_x + \epsilon}{S_i + \epsilon} \tag{4.6}$$

$$S_x = \sigma'_{I_g,1}(x) \times \sigma'_{I_g,r}(x) \tag{4.7}$$

Where γ_x is an edge attentive filtering parameter. $\Gamma_{I_g,x}$ is an edge attentive weight filtering parameter which measures the importance of pixel k with respect to the whole guidance image. ϵ is a small constant and its value is generally taken as $(0.001 \times L)^2$, where L represents the dynamic range of an input image, N_p is the total number

of pixels in a guidance image, S_x denotes the variance of the area centered at x, S represents all $S_i(i = 1...N_p)$, θ_S denotes the mean value of all S_i. $\sigma'_{I_g,1}$ and $\sigma'_{I_g,r}$ denotes the standard deviations for the windows $\omega_1(x)$ and $\omega_r(x)$ of image I_g. This indicates that S_x estimates the variance of the regions having radius 1 and r at the same time. The optimum values for $GDGF$ are then estimated as:

$$a_x = \frac{\theta_{I_g.d,r}(x) - \theta_{I_g,r}(x) \times \theta_{d,r}(x) + \frac{\epsilon}{\Gamma_{I_g,x}} \times \gamma_x}{\sigma'^2_{I_g,r}(x) + \frac{\epsilon}{\Gamma_{I_g,x}}}, \tag{4.8}$$

$$b_x = \theta_{d,r}(x) - a_x \times \theta_{I_g,r}(x), \tag{4.9}$$

In (4.8), (.) denotes the element wise multiplication of two different matrices. Here $\theta_{I_g.d,r}(x)$, $\theta_{I_g,r}(x)$ and $\theta_{d,r}$ denote the average values of $I_g.d$, I_g and d in the window $\omega(x)$. Finally the value of d' is estimated as

$$d'(y) = \theta_{a(y)} \times I_g(y) + \theta_{b(y)}, \quad \theta_{a(y)} = \frac{1}{|\omega(y)|} \sum_{x \in \omega(y)} a_x, \quad \theta_{b(y)} = \frac{1}{|\omega(y)|} \sum_{x \in \omega(y)} b_x \tag{4.10}$$

Here $|\omega(i)|$ denotes the cardinality of $\omega(i)$. If the pixel x lies on an edge, the value of γ_k approaches to 1 and 0 if the pixel x belongs to a smooth region. It can be said that, a_x behaves similar to γ_x. Finally, it can be concluded that, $GDGF$, provides better performance near edges by incorporating two edge attentive parameters including γ_x and $\Gamma_{I_g,x}$. The another positive factor about $GDGF$ is that it still performs filtering in $O(N)$ time. I_g is the guidance image which is the input image I and d' is the refined depth map obtained after applying $GDGF$. As discussed above, GF does not cleanly preserve all edges. $GDGF$ incorporates first order edge awareness constraints in GF and helps it to better preserve the edges in a smoothed image. This has also been shown in Figure 4.3. The areas inside red rectangles are zoomed and shown in other rectangles as indicated by arrows. In Figure 4.3 (b), the de-fogged image is produced by GF where as in Figure 4.3(c), $GDGF$ is used. The zoomed regions show that the former filter does not work properly for some fine details which can be dealt with $GDGF$.

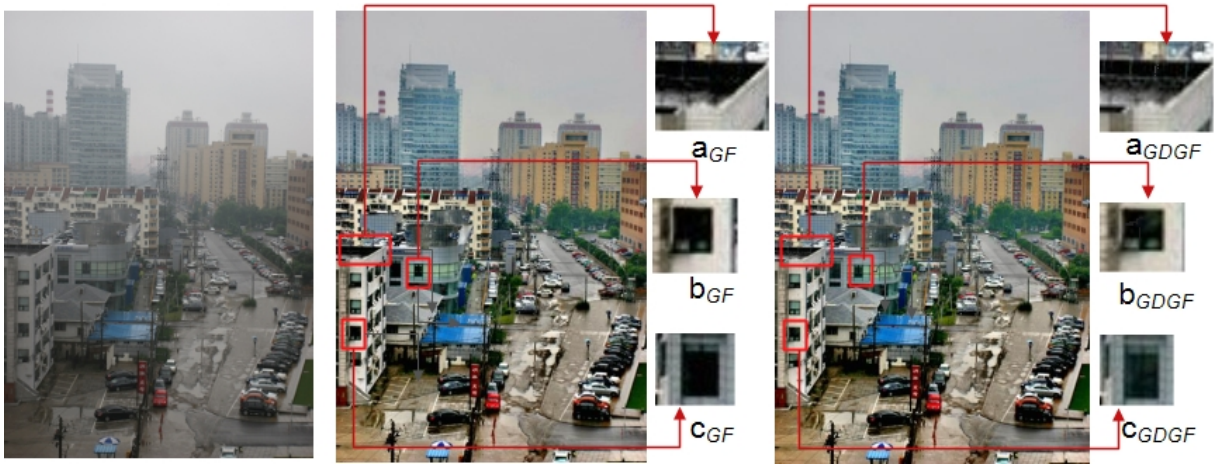

(a) (b) (c)

Figure 4.3: (a) Input Foggy Image. De-fogged images obtained using (b) Guided Filter [34] (c) Gradient Domain guided image Filter [64]

Inspired from [35], the performance of $GDGF$ is improved in this work by performing the above described operations on down sampled input images with scaling factor s. He *et al.* observed that, if GF is applied on down sampled images (Input image and the guided image) with $s = 4$, similar results can be achieved as that of full resolution images. This leads to a speedup of more than 10 times with almost no visible degradation. Similarly, in this work, with $GDGF$, the depth map d_{ref} and the guidance input image I are down sampled (nearest-neighbor or bilinear). All the window based filters are performed on the down sampled images. Finally, the coefficient maps $\bar{a}$ and $\bar{b}$ are up sampled to the original size by using bilinear interpolation and the refined depth map d' is computed by using the up sampled coefficients and the guidance image.

4.3.3 Atmospheric Light Estimation

Global atmospheric light L_A plays an important role in restoration based image de-fogging techniques. Higher values of atmospheric light produce darker de-fogged images and lower values obtain brighter de-fogged images [109]. According to [136], top 0.1% brightest pixels in the depth map represent the most fog opaque region of a foggy image which can be considered as the best region for atmospheric light estimation. According to physical model (1.11), the scene point value of a foggy image approaches to global atmospheric light in the regions of infinite depth. Consider (1.11):

$$I(x) = L_0 \times (x)e^{-\beta \times d(x)} + L_A \times (1 - e^{-\beta \times d(x)})$$

For the pixel x of infinite depth ($d(x) \to \infty$), $e^{-\beta \times d(x)} \to 0$, therefore,

$$I(x) \approxeq L_A \qquad or \qquad L_A \approxeq I$$

The regions of infinite depth generally lie at the top portion of an image. Therefore to save the computational time, L_A is found from the depth map of top 25% image rows. The rows are extracted and their corresponding depth map is obtained according to (4.3). Finally, the values in R, G, B color channels corresponding to top 0.1% brightest pixels in the depth image are selected as the value of global atmospheric light L_A. This value of atmospheric light obtained is further used in image de-fogging as described in the next section.

4.3.4 Transmission Estimation, Image Restoration and Non Uniform Illumination Compensation

The objective of an image de-fogging technique is to obtain a fog free image (L_0) from a foggy image (I). For this, refined depth map d' is obtained as described in Section 4.3.2. L_A is obtained as described in Section 3.3.

Transmission Map t is estimated using (1.10). Considering (1.37):

$$L_0^c(x) = L_A^c + \frac{I^c(x) - L_A}{min\{max\{e^{-\beta \times d'(x)}, 0.1\}, 0.9\}}$$

$L_0^c(x)$ is then recovered by putting the values of $I(x)$, $t(x)$ and L_A in (1.37). For avoiding noise in the de-fogging results, the values of transmission $t(x)$ are restricted between 0.1 and 0.9 [136]. $\beta = 1.0$ is also taken from [136].

It is generally an under-constrained problem to solve the scene radiance from the physical model (1.11) because the single value of global atmospheric light and the medium extinction coefficient are taken for the whole image. For avoiding the problem caused due to error in estimation of global atmospheric light and a constant value of β, we propose a method to compensate non uniform illumination and avoid dullness in the recovered image L_0 inspired from [111]. This method causes simultaneous dynamic range modification, color consistency, and lightness rendition in a time efficient manner. According to Lambert's law of illumination reflectance, the amount of light reflected by a point on the object or intensity of the given pixel, is the product of scene illumination and the object's reflectance, where light is completely disseminated in all directions. It is represented mathematically as:

$$L_0^c(x) = L_{L_0}(x) \times L_{R_0}^c(x) \tag{4.11}$$

Here L_{L_0} is the scene illumination and $R_{L_0}^c$ is the reflectance for color channel c. To avoid the problem of non-uniform illumination in the de-fogged image L_0, the fundamental problem is that, how to abolish the illumination veil L_{L_0}, at the same time keeping the reflectance R_{L_0}. The concept of bright channel prior has been widely used in the area of image processing [111]. According to bright channel prior, most local patches in an outdoor color image contain pixels whose intensity is very high in at least one color channel in RGB channel of each image point. Based on the model described in (4.11), the initial illumination veil $L_{L_0}^{bright}$ can be constructed from the bright channel prior as

$$L_{L_0}^{bright}(x) = max_{c \in RGB}(max_{y \in \Omega(x)}(L_0^c(y))) \tag{4.12}$$

The scene illumination should be smooth and also proficient of maintaining the image details. The smoothness is achieved by finding local maximum on a square patch in (4.12). To preserve image details, the edge preserving smoothening operation is applied on $L_{L_0}^{bright}$ by using $GDGF$ as described in Section 4.3.2 to obtain the final scene illumination L_{L_0} (4.11). Now as discussed above, the reflection coefficient is found by rearranging (4.11) as:

$$R_{L_0}^c(x) = \frac{L_0^c(x)}{L_{L_0}(x)} \tag{4.13}$$

The procedure described above does not produce any color distortion but there may be certain scenes points which may violate some "gray world" presumptions and generate some color biasness in R_{L_0}. To correct this, the gain/offset correction is performed simply by biasing the image average color towards pure white. A normalization operation is performed for a scene with dynamic range between $R_{L_0}^{min}$ and $R_{L_0}^{max}$. This transform can be done

using

$$R_{L_0}^{c'}(x,y) = \begin{cases} 0 & \text{if } L_R^c(x,y) \leq R_{L_0}^{min} \\ \frac{L_R^c(x,y) - L_{R_{min}}}{L_{R_{max}} - R_{L_0}^{min}} & \text{if } R_{L_0}^{min} \leq L_R^c(x,y) \leq R_{L_0}^{max} \\ 1 & L_R^c(x,y) \geq R_{L_0}^{max} \end{cases}$$

$R_{L_0}^{c'}$ and $R_{L_0}^{c}$ are the c^{th} color channel's input and output bands respectively,

$R_{L_0}^{min} = \mu - 2 \times \sigma$ and

$R_{L_0}^{max} = \mu + 2 \times \sigma$ are found by calculating mean μ and variance σ corresponding to the input image R_{L_0}.

The procedure described above yields a good visible representation of a de-fogged image as shown in Figure 4.4 (c). To find the bright channel (4.12), the strategy used in Section 4.3.1 is used. By doing this, the computational cost can be reduced. In this case, instead of applying minimum operation, local maximum is used.

(a) (b) (c)

Figure 4.4: (a) Input Foggy Image (b) De-fogged image without illumination compensation (c) De-fogged image with illumination compensation

4.3.5 Algorithm of *CAP* based Image De-fogging Technique

The steps involved in procedure of the CAP based image de-fogging technique have been summarized in the Algorithm 4.1:

Algorithm 4.1: *CAP* based Image De-fogging Technique.

i Obtain the brightness V and saturation components S from the foggy image I.

ii Find the initial depth map d from V and S with (1.35) by putting $\theta_0 = 0.121779$, $\theta_1 = 0.959710$, $\theta_2 = -0.780245$ and $\sigma^2 = 0.041337$.

iii Obtain window based depth map d_Ω from d by using the procedure described in Section 4.3.1 and refined depth map d' from the steps explained in Section 4.3.2.

iv Find L_A^c by using the top 25% rows of depth map d_Ω by using the procedure described in Section 4.3.3.

v Obtain the de-fogged image L_0^c from I, L_A and t by using (1.37).

vi Obtain the post processed image $L_0^{c'}$ from L_0^c by using the procedure described in Section 4.3.4

4.4 Experimental Results and Analysis

Proposed technique has been implemented in $MATLAB$ 2016 and tested on various standard foggy images of Choi's database [19] and Waterloo *IVC* dehazed image database [74]. These databases contain many hazy and foggy images taken in different type of environments. There are number of images reflecting lightening conditions of different day times. In next section the results of various techniques have been shown on images including $City1$ which is a morning time image representing hazy buildings, whereas $Night1$ and $Landscape3$ are evening time hazy images representing the natural scenes. $Cones$ is an image taken in wheat field during morning time in moderate fog, $Foggy\_building1$ and $Foggy\_road1$ are heavy fog images representing fog covered buildings and road. $Foggy\_road2$ is also a moderate fog image taken on road during day time. These images have been selected as these are capable of showing the performance of de-fogging techniques in different environments and day times. Both objective as well as subjective evaluations have been carried out to show the effectiveness of our technique on various image types.

4.4.1 Subjective Evaluation

In this section, the results of the our technique have been visually compared with existing techniques including Tarel *et al.* [114], He *et al.* [34], Cai *et al.* [17], Choi *et al.* [18], Meng *et al.* [79], Zhu *et al.* [136], Ren *et al.* [102], Liu *et al.* [73], Colores *et al.* [104] and Kansal *et al.* [56] *etc.* The work done by these authors in the field of de-fogging has been explained in Chapter 3, Section 3.3.1. Figure 4.5 contains the de-fogging results on "$City1$" image for He *et al.*, Tarel *et al.*, Meng *et al.*, Zhu *et al.*, Choi *et al.*, Cai *et al.* and proposed technique. Meng *et al.* and Tarel *et al's* results are saturated in sky area whereas the non sky region of Choi's result is over saturated. Results of Zhu *et al's* technique are better but the contrast of a de-fogged image is poor. In comparison, results of

the technique have higher contrast and are non saturated.

In Figure 4.6, the results of our technique are compared for an evening time image, "$Night1$". Clearly, the de-fogging results of all the techniques are over dark due to which the scene information is even lost. Since the technique applies non uniform illumination compensation which improves the illumination of the final image. Similar effect can also be observed in Figure 4.7 for "$Landscape3$".

In Figure 4.8, comparison is made between the de-fogging results of Fattal, Tarel *et al.*, He *et al.*, Meng *et al.*, Choi *et al.*, Cai *et al.* and proposed techniques for " $Cones$". He *et al.*, Choi *et al.* and Cai *et al's* techniques produce over saturation in the de-fogged images. Results of Meng *et al's* technique are better but look dull and diminished. In comparison, the result of our technique is better which can be visually observed.

In Figure 4.9 for "$Foggy\_building1$", it can be seen that the proposed technique can uncover the details and recover realistic color information also in dense foggy regions. Opposite to this, results of Meng *et al.*, Cai *et al.* and Choi *et al.* are over saturated. Cai *et al.* proposed a framework which trains a model to predict the transmission value $t(x)$ for each pixel by using its surrounding patch. It obtains good results but leaves a noticeable amount of fog in the recovered images. Results of Zhu *et al.* and Ren *et al.* are better than these but dense foggy regions are not properly enhanced and the overall results are poor in contrast.

Similar observation can be made in Figure 4.10 for "$Foggy\_road1$". The results have also been compared with Liu *et al's* wavelet based technique. This can simultaneously remove fog, improves sharpness of the image and remove noise. In Figure 4.10 (j), enhanced edges can be observed but at the same time image information in many areas is lost due to over darkness. Result of Colores *et al's* technique [104] based upon MLP is shown in Figure 4.10 (k). This technique is based upon multilayer perceptron to compute the transmission map directly from the minimum channel and a contrast stretching technique to improve the dynamic range of the restored image which shows no significant visibility improvement. In contrast to this, the road area, trees and cars *etc.* in the proposed results can be clearly visualized.

Next, the results of de-fogging for our technique are shown in Figure 4.11 for image "$Foggy\_road2$". For Cai *et al's* technique, the road portion becomes clearly over saturated. Meng's technique generates false colors in sky portion of the image. Tarel *et al's* image is good, but due to the use of double median filter, halo artifacts can be observed around the depth edges. Zhu *et al's* results are better but the information of the image is not well recovered. Liu *et al's* results are over dark whereas Colores *et al's* image is not clearly enhanced. In contrast to this, the results of the proposed technique efficiently removes fog and improves the image details. Finally, it can be concluded that the technique is capable of removing fog from digital images in different kinds of environments with varying amount of fog as shown in different type of images.

4.4.2 Objective Evaluation

The final restoration results of the proposed de-fogging technique have been compared with previous state-of-art techniques including Tarel *et al.*, He *et al.*, Meng *et al.*, Choi *et al.*, Zhu *et al.*, Cai *et al.*, Ren *et al.*, Liu *et al.*,

Figure 4.5: De-fogging results (a) Input foggy images "$City1$". De-fogging Results of (b) Tarel *et al.* (c) He *et al.* (d) Meng *et al.* (e) Zhu *et al.* (f) Choi *et al.* (g) Cai *et al.* (h) Proposed.

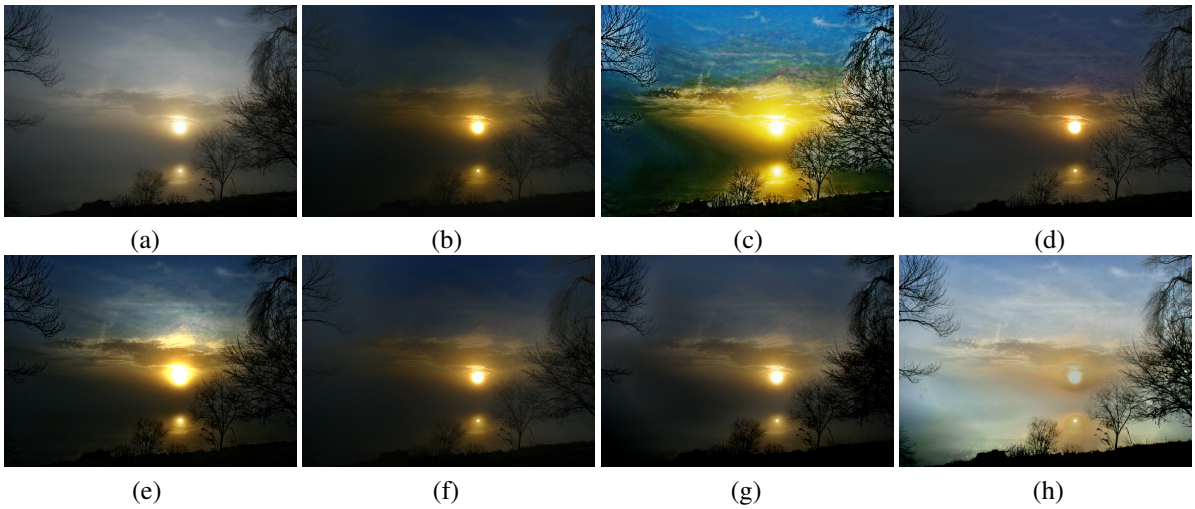

Figure 4.6: De-fogging results (a)Input foggy images "$Night1$". De-fogging results of (b) He *et al.* (c) Tarel *et al.* (d) Meng *et al.* (e) Xiao *et al.* (f) Tang *et al.* (g) Zhu *et al.* (h) Proposed

Colores *et al.* and Kansal *et al.* For comparison, 15 standard foggy images have been taken from databases [19] and [74]. To ensure comparability of various de-fogging techniques, descriptive variables or metrics for judging the output image quality are necessary. In this work, six different quality parameters including r, CNI, FRF, VCM, CI and CIE are shown in Tables 4.1- 4.6. A better de-fogging technique achieves higher values of the above factors. A better de-fogging technique achieves higher values of all the above factors and takes lesser time to execute.

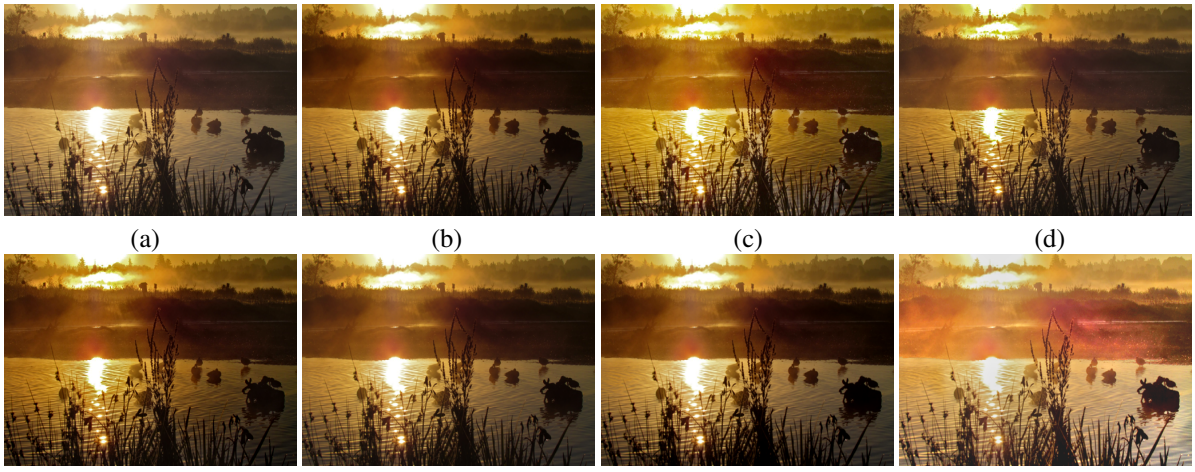

Figure 4.7: De-fogging results (a) Input foggy image "$Landscape3$". De-fogging results of (b) He *et al.* (c) Tarel *et al.* (d) Meng *et al.* (e) Xiao *et al.* (f) Tang *et al.* (g) Zhu *et al.* (h) Proposed

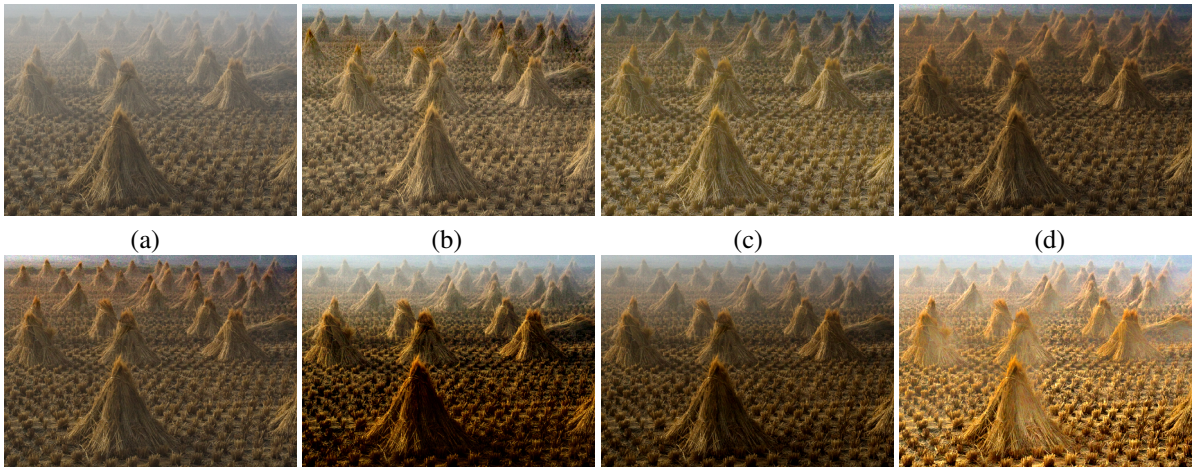

Figure 4.8: De-fogging results (a) Input foggy image "$Cones$". De-fogging results of (b) Fattal (c) Tarel *et al.* (d) He *et al.* (e) Meng *et al.* (f) Choi *et al.* (g) Cai *et al.* (h) Proposed

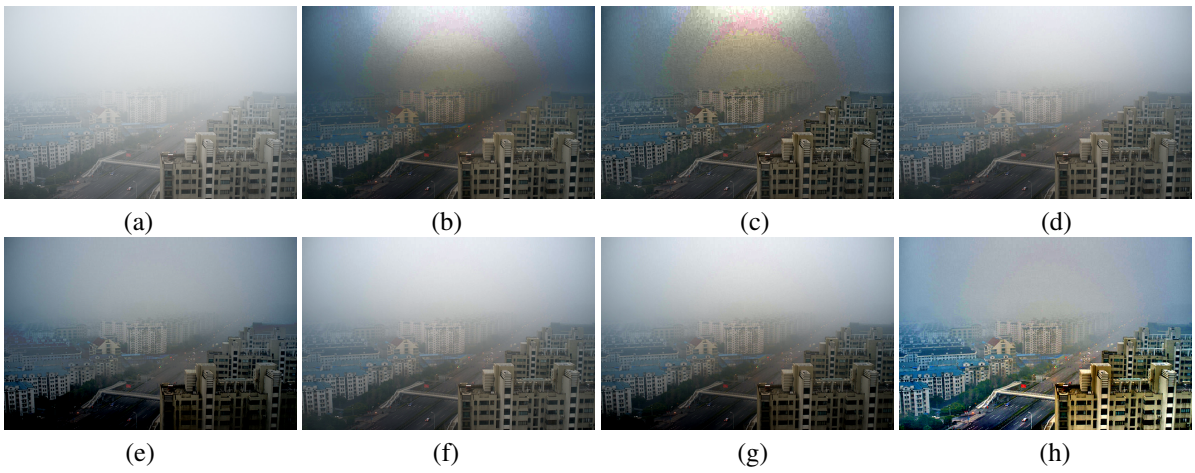

Figure 4.9: De-fogging results (a) Input foggy images "$Foggy\_building1$". De-fogging results of (b) He *et al.* (c) Meng *et al.* (d) Zhu *et al.* (e) Choi *et al.* (f) Ren *et al.* (g) Cai *et al.* (h) Proposed

Figure 4.10: De-fogging results (a)Input foggy images "$Foggy\_road1$". De-fogging results of (b) He *et al.* (c) Tarel *et al.* (d) Meng *et al.* (e)Shiau *et al.* (f) Choi *et al.* (g) Zhu *et al.* (h) Cai *et al.* (i) Ren *et al.* (j) Liu *et al.* (k) Colores *et al.* (l) Proposed

Figure 4.11: (a) Input Foggy Image "$Foggy\_road2$". De-fogged images obtained using techniques of (b) He *et al.* (c) Tarel *et al.* (d) Meng *et al.* (e) Shiau *et al.* (f) Choi *et al.* (g) Zhu *et al.* (h) Cai *et al.* (i) Ren *et al.* (j) Liu *et al.* (k) Colores *et al.* (l) Proposed

From Tables 4.1-4.6, it can be observed that our technique outperforms the existing techniques except Meng *et al.* in terms of r, but at the same time, CNI, FRF, CI and CIE are better than that of Meng *et al.*. In comparison to proposed technique, Choi *et al's* technique is better in terms of VCM and slightly better in terms of FRF and CI, but r, CNI and CIE of our technique are far better than Choi *et al's* technique. At the same time Choi's technique is almost 100 times slower than that of proposed technique as shown in Table 4.7. Kansal *et al's* technique is also better than that of the proposed technique in terms of VCM and CI, but they are less in terms of r, FRF, CNI and CIE.

Since the proposed technique aims to improve Zhu *et al's* CAP based technique, the percentage improvement achieved by the technique with respect to CAP technique is 82.91% in r, 20.63% in CNI, 73.11% in FRF, 4.71% in VCM, 30.00% in CI, 1.91% in CIE, which is considerably high. The maximum percentage improvement achieved by the technique with respect to other techniques is 86.09% in r, 22.58% in CNI, 100.00% in FRF, 13.22% in VCM, 37.07% in CI, 7.20% in CIE. The minimum percentage improvement achieved by the technique with respect to other techniques is 5.42% in r, 1.33% in CNI, 11.96% in FRF, 1.99% in VCM, 3.31% in CI, 1.09% in CIE. Furthermore, the average execution time taken by the the technique is significantly less than that of Zhu's technique. The overall results achieved by the the technique are satisfactory as described above.

Table 4.1: Comparison of the proposed technique with existing techniques on the basis of r

	Tarel *et al.* [114]	He *et al.* [34]	Meng *et al.* [79]	Choi *et al.* [18]	Zhu *et al.* [136]	Cai *et al.* [17]	Ren *et al.* [102]	Liu *et al.* [73]	Colores *et al.* [104]	Kansal *et al.* [56]	Proposed
City1	2.21	1.37	2.03	1.61	1.14	1.14	1.17	1.35	1.14	1.70	2.06
Night1	2.69	0.71	1.12	1.20	0.86	0.64	0.94	1.15	1.02	1.75	2.06
Landscape3	1.34	1.00	1.13	1.35	1.08	0.94	1.09	1.06	1.07	1.18	1.46
Foggy_building1	2.31	1.67	3.18	1.39	1.22	1.27	1.23	1.79	1.20	2.42	2.33
Foggy_road1	2.31	1.49	2.36	1.78	1.24	1.08	1.45	1.69	1.30	2.37	2.66
Foggy_road2	2.28	1.48	2.56	1.43	1.14	1.01	1.17	1.35	1.12	2.02	1.52
Cones	1.88	1.59	1.61	1.66	1.13	1.38	1.22	1.35	1.20	1.62	1.79
Cityscape	5.08	3.68	5.18	1.88	1.47	1.81	1.79	3.13	1.55	3.47	1.96
Foggy_ground	2.99	1.23	2.44	2.13	1.16	1.25	1.30	1.46	1.21	1.94	4.77
People	1.81	1.16	1.37	1.42	1.11	1.07	1.10	1.29	1.25	1.37	1.74
Foggy_building2	1.86	1.33	2.78	1.29	1.04	1.10	1.50	1.62	1.23	3.63	2.04
Toys	2.04	2.05	2.34	1.95	1.51	1.62	1.52	2.19	1.51	2.26	1.87
Y1	1.66	1.24	1.35	1.53	1.13	0.94	1.10	1.27	1.10	1.56	2.07
Y16	1.88	1.44	1.67	1.48	1.22	1.19	1.33	1.53	1.35	1.64	1.44
Aerial	1.82	1.04	1.46	1.67	1.06	0.76	1.17	1.27	1.09	1.52	2.30
Average	**2.28**	**1.50**	**2.17**	**1.58**	**1.17**	**1.15**	**1.27**	**1.57**	**1.22**	**2.03**	**2.14**

Table 4.2: Comparison of the proposed technique with existing techniques on the basis of CNI

	Tarel *et al.* [114]	He *et al.* [34]	Meng *et al.* [79]	Choi *et al.* [18]	Zhu *et al.* [136]	Cai *et al.* [17]	Ren *et al.* [102]	Liu *et al.* [73]	Colores *et al.* [104]	Kansal *et al.* [56]	Proposed
City1	0.62	0.54	0.53	0.58	0.50	0.53	0.53	0.58	0.52	0.55	0.65
Night1	0.92	0.77	0.78	0.78	0.68	0.79	0.66	0.95	0.66	0.91	0.62
Landscape3	0.97	0.96	0.92	0.99	0.93	0.98	0.49	0.97	0.94	0.97	0.91
Foggy_building1	0.74	0.63	0.54	0.45	0.45	0.47	0.53	0.52	0.44	0.63	0.75
Foggy_road1	0.61	0.52	0.51	0.62	0.48	1.00	0.51	0.50	0.44	0.52	0.76
Foggy_road2	0.57	0.50	0.52	0.51	0.48	0.46	0.51	0.47	0.48	0.51	0.54
Cones	0.731	0.73	0.69	0.80	0.57	0.73	0.60	0.81	0.63	0.93	0.89
Cityscape	0.59	0.57	0.60	0.53	0.54	0.42	0.61	0.58	0.58	0.57	0.66
Foggy_ground	0.79	0.59	0.57	0.51	0.53	0.59	0.59	0.62	0.55	0.59	0.79
People	0.89	0.83	0.89	0.88	0.67	0.67	0.79	0.82	0.67	0.85	0.85
Foggy_building2	0.85	0.97	0.83	1.00	0.75	0.63	0.64	0.97	0.63	0.98	0.70
Toys	0.73	0.85	0.82	0.76	0.68	0.65	0.63	0.85	0.64	0.85	0.80
Y1	0.74	0.46	0.65	0.25	0.75	0.75	0.81	0.29	0.74	0.43	0.76
Y16	0.78	0.63	0.76	0.63	0.86	0.94	0.73	0.50	0.78	0.76	0.83
Aerial	0.79	0.69	0.64	0.70	0.57	0.64	0.54	0.70	0.55	0.75	0.88
Average	**0.75**	**0.68**	**0.68**	**0.67**	**0.63**	**0.68**	**0.61**	**0.68**	**0.62**	**0.72**	**0.76**

Table 4.3: Comparison of the proposed technique with existing techniques on the basis of FRF

	Tarel *et al.* [114]	He *et al.* [34]	Meng *et al.* [79]	Choi *et al.* [18]	Zhu *et al.* [136]	Cai *et al.* [17]	Ren *et al.* [102]	Liu *et al.* [73]	Colores *et al.* [104]	Kansal *et al.* [56]	Proposed
City1	1.35	1.19	1.38	2.33	0.72	2.75	1.89	1.75	0.68	1.23	2.11
Night1	2.15	1.61	1.61	2.11	2.15	2.90	0.20	2.47	1.62	1.53	0.85
Landscape3	0.51	0.53	0.38	0.62	0.62	1.12	-2.23	0.61	0.44	0.53	0.16
Foggy_building1	3.06	3.25	3.37	4.85	1.53	3.75	3.7	3.34	1.27	3.35	4.38
Foggy_road1	2.40	2.26	2.16	3.71	1.05	3.82	1.47	2.94	1.07	2.37	2.94
Foggy_road2	1.71	1.61	1.64	2.86	1.49	2.87	1.11	2.26	0.91	1.68	1.80
Cones	1.37	1.74	1.54	2.27	0.85	1.94	0.88	2.03	1.08	1.72	1.78
Cityscape	2.58	2.66	2.96	3.04	1.15	2.04	1.89	2.46	1.42	2.62	2.86
Foggy_ground	3.69	3.35	2.81	3.38	1.82	4.26	1.26	3.81	1.60	3.47	3.99
People	0.93	0.91	1.09	2.02	0.53	1.40	0.97	1.08	0.75	0.94	1.18
Foggy_building2	2.83	2.45	2.26	2.62	1.68	1.60	1.41	2.62	1.16	2.23	2.90
Toys	1.12	2.04	1.98	2.02	1.24	1.73	1.13	2.13	1.05	2.06	1.95
Y1	1.17	1.58	1.47	1.63	1.17	2.25	0.91	1.71	0.93	1.48	1.54
Y16	0.89	0.94	1.06	1.41	0.76	0.72	0.96	1.20	0.73	0.90	1.15
Aerial	1.41	1.11	0.99	1.77	1.01	2.07	0.73	1.40	0.72	1.17	1.27
Average	**1.81**	**1.82**	**1.78**	**2.44**	**1.18**	**2.35**	**1.08**	**2.12**	**1.03**	**1.82**	**2.06**

Table 4.4: Comparison of the proposed technique with existing techniques on the basis of VCM

	Tarel *et al.* [114]	He *et al.* [34]	Meng *et al.* [79]	Choi *et al.* [18]	Zhu *et al.* [136]	Cai *et al.* [17]	Ren *et al.* [102]	Liu *et al.* [73]	Colores *et al.* [104]	Kansal *et al.* [56]	Proposed
City1	68.83	46.00	54.17	66.00	45.83	50.67	19.50	56.33	45.00	54.83	66.17
Night1	37.00	30.17	42.67	53.50	37.50	29.33	54.33	52.50	43.50	30.00	49.67
Landscape3	48.59	45.78	49.06	51.56	47.97	45.00	20.63	47.97	47.19	48.13	41.09
Foggy_building1	35.50	21.33	32.33	49.83	48.17	52.00	57.17	34.17	47.17	31.67	54.17
Foggy_road1	28.65	29.81	37.12	35.77	53.65	58.08	49.42	36.54	24.42	36.73	41.35
Foggy_road2	48.27	25.38	35.77	40.00	27.50	26.92	52.50	34.81	25.58	33.08	56.15
Cones	67.98	61.40	69.08	75.44	47.81	56.80	49.34	63.60	47.59	61.62	59.43
Cityscape	56.62	58.98	73.87	37.39	59.17	33.58	31.58	52.45	57.35	52.99	25.77
Foggy_ground	43.57	30.54	36.07	47.50	29.11	30.71	28.04	31.07	27.68	35.36	16.25
People	86.60	79.43	76.56	83.97	76.32	75.84	75.12	81.34	77.03	79.19	78.95
Foggy_building2	38.60	23.31	39.10	21.05	45.36	50.88	30.83	33.83	56.64	61.90	35.59
Toys	55.56	69.01	70.96	67.06	50.88	53.61	53.22	72.71	49.71	70.76	49.12
Y1	59.92	51.42	52.43	57.89	46.76	41.30	45.95	53.24	44.13	57.09	56.68
Y16	70.65	70.45	70.24	70.45	65.59	64.37	68.42	70.45	67.81	72.06	63.97
Aerial	38.35	18.61	34.96	49.62	15.98	47.56	22.93	34.77	18.23	28.01	36.65
Average	**52.31**	**44.11**	**51.63**	**53.80**	**46.51**	**47.78**	**43.93**	**50.39**	**45.27**	**50.23**	**48.73**

Table 4.5: Comparison of the proposed technique with existing techniques on the basis of CI

	Tarel *et al.* [114]	He *et al.* [34]	Meng *et al.* [79]	Choi *et al.* [18]	Zhu *et al.* [136]	Cai *et al.* [17]	Ren *et al.* [102]	Liu *et al.* [73]	Colores *et al.* [104]	Kansal *et al.* [78]	Proposed
City1	23.36	13.47	14.91	16.83	11.65	13.35	11.84	13.84	12.07	34.75	18.75
Night1	52.77	28.19	26.30	33.66	24.74	26.82	21.01	41.14	26.37	31.16	31.35
Landscape3	67.44	61.99	62.03	79.47	59.47	63.99	61.17	62.79	59.97	67.44	67.82
Foggy_building1	29.69	19.93	19.34	16.73	11.17	12.13	10.38	15.01	10.61	39.37	17.52
Foggy_road1	33.72	20.76	21.97	27.99	18.14	48.28	18.81	21.57	18.00	49.74	26.92
Foggy_road2	40.03	28.98	30.73	28.77	26.72	27.97	26.61	30.19	27.28	53.68	36.79
Cones	31.44	28.66	27.72	42.40	22.69	30.15	23.32	31.64	24.82	60.08	40.10
Cityscape	36.61	26.12	29.45	19.81	18.00	21.05	21.99	24.64	20.01	46.99	28.05
Foggy_ground	40.69	21.83	24.11	20.52	14.10	14.28	13.30	17.13	13.36	85.57	63.30
People	44.51	40.63	45.28	54.77	32.86	37.34	35.15	38.87	40.25	66.59	41.92
Foggy_building2	51.91	30.03	29.16	47.85	25.08	20.72	20.65	30.52	20.52	60.34	47.58
Toys	54.34	75.28	67.82	69.65	60.14	58.66	52.20	77.57	51.33	91.64	68.62
Y1	77.30	98.66	85.31	97.35	81.44	47.84	68.40	102.83	63.80	79.14	55.76
Y16	88.63	101.54	82.17	95.48	79.19	53.52	75.37	104.10	73.00	75.37	64.42
Aerial	41.78	32.62	32.82	38.46	26.53	28.83	25.28	32.39	25.27	73.47	56.63
Average	**47.61**	**41.91**	**39.94**	**45.98**	**34.13**	**33.66**	**32.37**	**42.95**	**32.44**	**61.02**	**44.37**

Table 4.6: Comparison of the proposed technique with existing techniques on the basis of CIE

	Tarel *et al.* [114]	He *et al.* [34]	Meng *et al.* [79]	Choi *et al.* [18]	Zhu *et al.* [136]	Cai *et al.* [17]	Ren *et al.* [102]	Liu *et al.* [73]	Colores *et al.* [104]	Kansal *et al.* [78]	Proposed
City1	7.03	7.32	7.22	7.41	7.29	7.07	7.37	7.45	7.27	7.22	7.14
Night1	7.26	6.46	6.43	7.09	6.50	4.83	7.00	6.75	7.18	6.78	6.95
Landscape3	7.65	7.46	7.45	7.45	7.36	6.33	7.45	7.45	7.46	7.71	7.86
Foggy_building1	7.24	7.24	7.39	7.09	7.68	7.75	7.59	7.83	7.69	7.19	6.95
Foggy_road1	7.06	7.17	6.99	6.73	7.41	6.77	7.40	7.32	7.43	7.47	7.28
Foggy_road2	7.36	7.51	7.41	6.97	7.66	7.04	7.77	7.47	7.73	6.85	7.12
Cones	7.02	7.01	6.98	6.97	7.18	7.25	7.22	7.15	7.28	7.83	7.90
Cityscape	6.75	7.33	7.40	6.52	6.94	7.31	7.22	7.57	7.09	6.85	6.90
Foggy_ground	7.28	6.75	6.55	7.06	6.90	6.47	7.13	6.64	7.22	7.41	7.23
People	7.53	7.58	7.33	7.01	7.59	7.39	7.61	7.64	7.62	7.71	7.90
Foggy_building2	7.28	6.93	7.20	7.09	6.87	7.32	7.46	7.19	7.30	7.22	7.59
Toys	7.32	7.79	7.62	7.74	7.62	7.69	7.52	7.83	7.61	7.59	7.64
Y1	7.53	7.50	7.43	7.22	7.47	7.27	7.53	7.44	7.61	7.70	7.67
Y16	7.66	7.68	7.82	7.45	7.77	7.75	7.90	7.67	7.78	7.51	7.69
Aerial	7.08	6.98	6.92	7.07	7.29	5.93	7.55	7.02	7.49	7.36	7.75
Average	**7.27**	**7.25**	**7.21**	**7.12**	**7.30**	**6.94**	**7.45**	**7.36**	**7.45**	**7.36**	**7.44**

4.4.3 Execution Time Comparison

The execution time comparison of the proposed technique with other existing techniques has been shown in Table 4.7. For this comparison, image size, tools used for implementing the technique (*i.e* C++, MATLAB or Not Mentioned) and the type of processor are considered for each of the technique.

Table 4.7: Comparison of execution time of the proposed technique with existing techniques

Technique	**Processor**	**Tool**	**Image Size**	**Execution Time**
Tan [112]	Pentium 4	N/A	600×400	5-7min
Fattal [23]	Dual-Core	C++	512×512	35s
Tarel *et al.* [114]	Quad-Core	MATLAB	600×400	5.9s
He *et al.* [34]	Quad-Core	MATLAB	600×400	1.99s
Meng *et al.* [79]	Quad-Core	MATLAB	600×400	1.80s
Choi *et al.* [18]	Quad-Core	MATLAB	600×400	12.52s
Zhu *et al.* [136]	Quad-Core	MATLAB	600×400	0.69s
Cai *et al.* [17]	Quad-Core	MATLAB	600×400	2.00s
Ren *et al.* [102]	Quad-Core	MATLAB	600×400	1.81s
Liu *et al.* [73]	Quad-Core	MATLAB	600×400	0.25s
Colores *et al.* [104]	Quad-Core	MATLAB	600×400	0.35s
Kansal *et al.* [56]	Quad-Core	MATLAB	600×400	0.10s
Proposed	Quad-Core	MATLAB	600×400	0.12s

It can be seen from Table 4.7 that the processing speed of our technique is better than all techniques except Kansal *et al.*. But overall de-fogging performance of the technique is better than the other existing techniques. It can be concluded that the technique is computational effective than that of existing techniques and at the same time, other parameters of quality have not been compromised.

4.4.4 De-fogging Results on *FRIDA* with varying Fog Density

In this section, the parameters have been evaluated on $FRIDA$. The visual result for $FRIDA$ image is shown in Figure 4.12. In Table 4.8, the average data of the proposed technique for 330 images for r, CNI, FRF, VCM, CI, CIE has been shown in comparison to existing techniques. It can be observed that the technique still outperforms various existing techniques in the case of images suffering from different fog densities.

From Tables 4.8, it can be seen that the percentage improvement of the technique with respect to CAP technique is 232.94% in r, 66.27% in CNI, 227.84% in FRF, 51.40% in VCM, 200.09% in CI and 5.49% in CIE. Also the maximum percentage improvement achieved by the technique with respect to existing techniques is 242.84% in r, 70.32% CNI, 334.47% in FRF, 59.91% VCM, 203.36% CI, 9.90% in CIE and the min-

imum percentage improvement is 69.00% in r, 3.70% in CNI, 13.29% in FRF, 23.43% VCM, 25.09% CI, 3.35% in CIE.

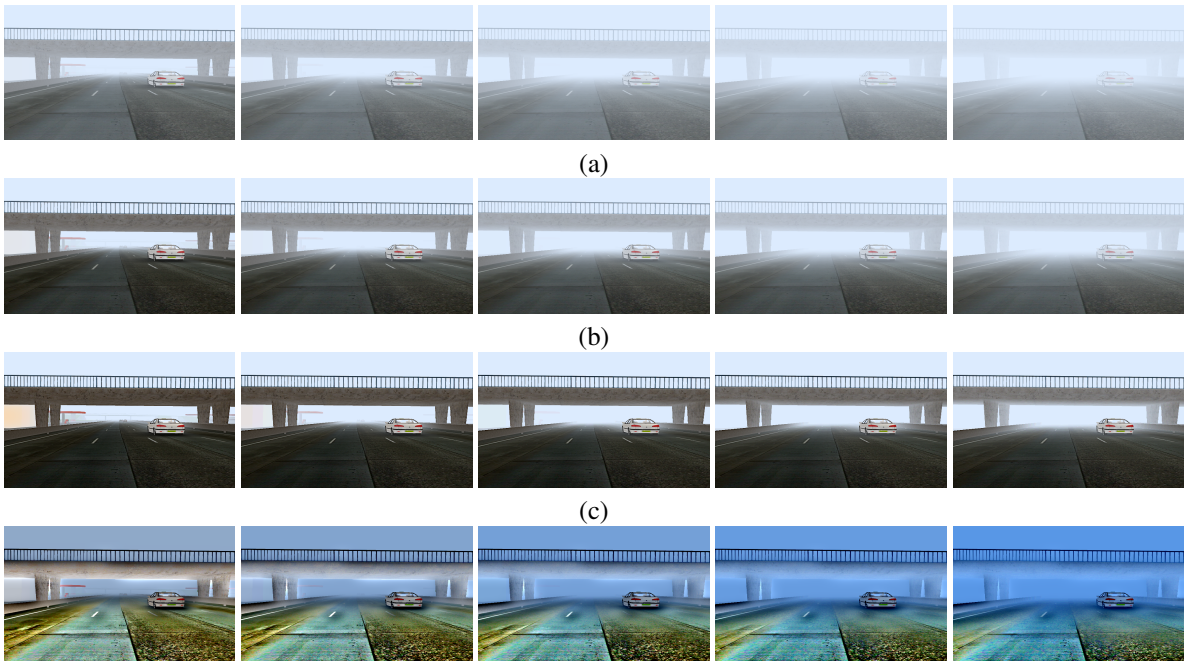

Figure 4.12: (a) Input foggy images of $FRIDA$ with $\beta = 0.02,\ 0.04,\ 0.06, 0.08,\ 0.1$ (left-right) (b) Corresponding de-fogged images obtained by Zhu *et al's* technique, (c) Corresponding de-fogged images obtained by Kansal *et al's* technique, (d) Corresponding de-fogged images obtained by proposed technique.

Table 4.8: Comparison of r, CNI, FRF, VCM, CI and CIE of the proposed technique with existing techniques on $FRIDA(66\ Images)$ with varying fog density ($\beta = 0.02,\ 0.04, 0.06,\ 0.08, 0.1$)

	r	**CNI**	**FRF**	**VCM**	**CI**	**CIE**
Tarel *et al.* [114]	2.35	0.81	3.58	34.08	43.11	5.96
He *et al.* [34]	1.88	0.56	3.25	37.89	19.21	5.94
Cai *et al.* [17]	1.64	0.53	2.85	36.80	19.72	6.10
Choi *et al.* [18]	1.58	0.85	4.74	34.88	33.16	7.10
Meng *et al.* [79]	3.00	0.56	3.35	39.97	23.08	5.90
Zhu *et al.* [136]	1.52	0.51	1.64	33.24	17.98	6.08
Ren *et al.* [102]	1.58	0.50	1.28	31.85	18.08	5.84
Liu *et al.* [73]	2.22	0.56	3.93	40.82	18.45	6.21
Colores *et al.* [104]	1.48	0.49	1.24	31.51	17.78	6.05
Kansal *et al.* [56]	2.38	0.56	3.44	39.69	19.04	5.97
Proposed	5.07	0.84	5.37	50.38	53.93	6.42

4.5 Conclusion of the Chapter

In this Chapter, a de-fogging technique based upon CAP is proposed. Using CAP, depth from a foggy image at each pixel is estimated based on difference between saturation and brightness for the respective pixel. Local window based minimum operation is applied to optimize the estimation time of the depth map. Depth map is further refined using gradient domain guided image filter which recovers fine edge details. For avoiding the problem caused due to error in estimation of global atmospheric light and a constant value of β, we present a novel strategy to post process the de-fogged image. It causes simultaneous dynamic range modification, color consistency, and lightness rendition without having the artifacts in a time efficient manner. The technique attains improvement over Zhu *et al's* technique by 79.16% in r, 16.9% in CNI, 73.10% in FRF, 4% in VCM, 30% in CI, 1.9% in CIE, which is considerably high. The maximum percentage improvement achieved by the technique with respect to other compared techniques is 80.67% in r, 22.58% in CNI, 73.10% in FRF, 13.22% in VCM, 37.07% in CI, 7.20% in CIE, whereas the minimum percentage improvement is 1.89% in r, 1.33% in CNI, 11.95% in FRF, 1.98% in VCM, 3.30% in CI, 1.09% in CIE. For $FRIDA$ database, the percentage improvement achieved by the the technique with respect to CAP technique is 232.94% in r, 66.27% in CNI, 227.84% in FRF, 51.40% in VCM, 200.09% in CI and 5.49% in CIE. Also the maximum percentage improvement achieved by the technique with respect to existing techniques is 242.84% in r, 70.32% CNI, 334.47% in FRF, 59.91% VCM, 203.36% CI, 9.90% in CIE and the minimum percentage improvement is 69.00% in r, 3.70% in CNI, 13.29% in FRF, 23.43% VCM, 25.09% CI, 3.35% in CIE. Experimental results show that the technique achieves high efficiency and a better de-fogging effect. It can be also be applied to real time applications due to its low computational cost.

Chapter 5

Fusion based Image De-fogging using Dual Tree Complex Wavelet Transform

5.1 Introduction

In this Chapter, an effective fusion based foggy image restoration technique by using $DTCWT$ has been proposed. Minimum color channel and the dark channel of a foggy image are constructed. Low and high pass components of both these channels are fused to obtain a transmission map. Dark channel is estimated by minimum preserving down sampling approach which improves the computational efficiency of de-fogging process. Since DCP based de-fogging techniques suffer from halo artifacts and darkness, proposed technique improves the overall contrast and the halo artifact regions in a time efficient way. To make the de-fogging results look uniformly bright, an adaptive post processing technique is applied on the de-fogged images. Comparative experiments with existing state-of-the-art algorithms show that de-fogging results of the technique are better. [†].

Image de-fogging techniques generally suffer from color and edge distortion problems. Color distortion generally occurs due to a smaller patch size while an edge distortion happens due to a larger patch. Another major limitation of the de-fogging techniques is the large time complexity which makes them hard to use in real time applications. The above mentioned problems have been elucidated in the proposed work. In this Chapter, transmission map is estimated by fusing wavelet subbands of minimum color channel and dark channel of a foggy image. The wavelet chosen is $DTCWT$ ([14], [63]) which ensures the perfect reconstruction of image details in the transmission map due to its shift in-variance property. $DTCWT$ is also rich in directional selectivity of an input signal and hence obtains high quality edges in the de-fogging results. The processing time is reduced by estimating the dark channel with minimum preserving downsampling approach. In addition to this, de-fogging results are further enhanced by using an adaptive post processing technique. The major contributions of the Chapter

[†]**Contents of the work presented in this Chapter have been published in *International Journal of Wavelets, Multiresolution and Information Processing*, 16(06), pp. 1850054(1-27), 2018. (SCI Indexed)**

are:

(i) Transmission Map is found by fusing wavelet sub-bands of dark channel maps with patch size 1×1 and 15×15 by using $DTCWT$, to solve the color and edge distortion problems which occur due to a fixed window size. Due to high directional selectivity of $DTCWT$, the edge details are enhanced in the transmission map. $DTCWT$ also ensures the perfect reconstruction of image details in the transmission map due to its shift invariance property.

(ii) In order to increase the computational efficiency of the technique, dark channel is estimated by using the minimum preserving down sampling approach.

(iii) Since, foggy images are affected by the environment lightening, some parts of the de-fogged images may suffer from low brightness and due to dark channel prior based image restoration, de-fogged images will be even more darker. Therefore, an adaptive post processing technique is used to maintain the uniform brightness in the de-fogging results.

5.2 Dual Tree Complex Wavelet Transform

DCP [33] technique produces blocking or halo artifacts due to patch based minimum operation and causes transmission over estimation problem in regions around the edges of an image. Halo artifacts are actually the difference between patch based dark channel and the minimum color channel as demonstrated by Shiau *et al.* [109]. Although, by using soft matting or guided filter, these artifacts can be reduced, but the areas around the depth edges still look foggy. So, in order to improve the transmission overestimation around the edges, this Chapter proposes a $DTCWT$ based fusion technique to estimate transmission map. The theory of wavelet combines the signal processing and mathematics. In recent years, it has been widely applied to image processing applications like noise reduction, resolution enhancement, classification, segmentation, image restoration and motion estimation *etc.* Wang *et al.* [120] applied DWT on two coarse dark channels to estimate transmission map for image de-fogging. Although, conventional DWT prevents repetitions and allows to use the same filter pairs in different scales, but it has two main characteristics which include the shift invariance and low directional selectivity. When there is a slight shift in the input signal, it causes higher energy variation in the wavelet coefficients. This is the shift invariance property of DWT. To effectively represent a two dimensional ($2D$) signal, DWT is inappropriate. It decomposes the high pass frequency component of an input signal in horizontal, vertical and the diagonal directions only. Such real DWT problems can be dealt with complex wavelets. But, beyond level 1, even complex wavelets cause problems in achieving perfect reconstruction of the input signal.

To beat these issues, Kingsbury [62] proposed the concept of $DTCWT$. This allows perfect reconstruction of an input signal while affording the other advantages of complex wavelets. For performing wavelet analysis, $DTCWT$ makes use of analytic filters. Two real DWT trees (a and b), as shown in Figure 5.1, are used to

implement the real and imaginary parts of one dimensional ($1D$) $DTCWT$. Tree a represents the real part (r) of the complex wavelet coefficient, whereas Tree b shows the imaginary part (i) oriented in the same direction. x is the input image, $H_{0a},\ H_{0b},\ H_{00a},\ H_{00b}$ are the low pass filters at different levels whereas $H_{1a},\ H_{1b},\ H_{01a},\ H_{01b}$ are the high pass filters. The $DTCWT$ uses length-10 filters [62], the table of coefficients [63] of the analyzing filters in the first stage (Table 5.1) and the remaining levels (Table 5.2) are shown. These filters are designed in such a way that the corresponding wavelets, $\psi_{H_a}(t)$ and $\psi_{H_b}(t)$ form approximately a Hilbert pair. Similarly, the resulting scaling functions, $\varphi_{H_a}(t)$ and $\varphi_{H_b}(t)$ should be such that $\varphi_{H_b}(t)$ is approximately the Hilbert transform of $\varphi_{H_a}(t)$. Therefore the complex wavelet $\psi(t)$ and complex scaling function $\varphi(t)$ described by the following equation would be approximately analytic [62]:

$$\psi(t) = \psi_{H_a}(t) + i\psi_{H_b}(t), \qquad \varphi(t) = \varphi_{H_a}(t) + i\varphi_{H_b}(t) \tag{5.1}$$

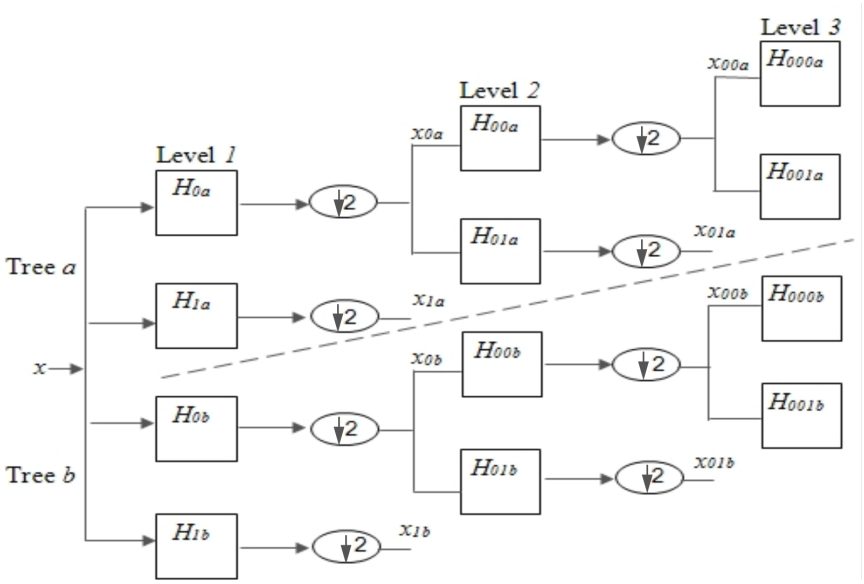

Figure 5.1: Tree Structure of $DTCWT$.

The extension to two dimensions is achieved by $2D$ complex separable wavelets described by (5.2) and a $2D$ complex separable scaling function described by (5.3). They are implemented by separable filters along columns and then rows:

$$\psi 1(x,y) = \varphi(x)\psi(y), \qquad \psi 2(x,y) = \psi(x)\varphi(y), \qquad \psi 3(x,y) = \psi(x)\psi(y) \tag{5.2}$$

$$\varphi 4(x,y) = \varphi(x)\varphi(y) \tag{5.3}$$

where $\psi(.)$ and $\varphi(.)$ are as shown in (5.1). The resulting wavelet coefficients are then combined by simple sum and difference operations to give real and imaginary wavelet coefficients.

Table 5.1: Analysis Filter Coefficients at first level

Tree a		**Tree b**	
H_{0a}	H_{1a}	H_{0b}	H_1b
0	0	0.01122679	0
-0.08838834	-0.01122679	0.01122679	0
0.08838834	0.01122679	-0.08838834	-0.08838834
0.69587998	0.08838834	0.08838834	-0.08838834
0.69587998	0.08838834	0.69587998	0.69587998
0.08838834	-0.69587998	0.69587998	-0.69587998
-0.08838834	0.69587998	0.08838834	0.08838834
0.01122679	-0.08838834	-0.08838834	0.08838834
0.01122679	-0.08838834	0	0.01122679
0	0	0	-0.01122679

Table 5.2: Analysis Filter Coefficients at remaining levels

Tree a		**Tree b**	
H_{00a}	H_{01a}	H_{00b}	$H_{01}b$
0.03516384	0	0	-0.03516384
0	0	0	0
-0.08832942			0.08832942
0.23389032	0	0	0.23389032
0.76027237	0.58751830	0.58751830	-0.76027237
0.58751830	-0.76027237	0.76027237	0.58751830
0	0.23389032	0.23389032	0
-0.11430184	0.08832942	-0.08832942	-0.11430184
0	0	0	0
0	-0.03516384	0.03516384	0

DWT produces four bandpass sub-images at each level corresponding to low-low, low-high, high-low and high-high filtering, while $DTCWT$ produces three sub-images in each of spectral quadrants and giving six band-pass sub-images of complex coefficients at each level which are strongly oriented at angles of $\pm 15^{\circ}$, $\pm 45^{\circ}$ and $\pm 75^{\circ}$, as shown in Figure 5.2 [121]. Upper part of Figure 5.2 represents real oriented $DTCWT$ whereas lower part shows its imaginary counterpart. $DTCWT$ produces four low pass sub-bands and twelve high pass sub-bands in total.

As discussed above, $DTCWT$ is very effective in representing image details due to its high direction selectiv-

ity and shift invariance properties. Therefore, these properties are utilized in this work to estimate an effective transmission map for image de-fogging as explained in Section 5.3.3.

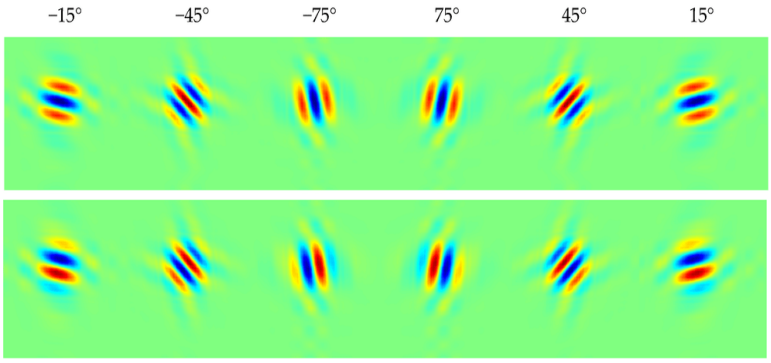

Figure 5.2: Response of Real and Complex filters depicting the orientations of dual tree complex wavelet transform.

5.3 Proposed Fusion based Image De-fogging Technique based on DTCWT

In this section, fusion based transmission, atmospheric light estimation, image restoration and post processing used in this $DTCWT$ based image de-fogging technique have been discussed in details.

5.3.1 Sampling based Dark Channel Estimation

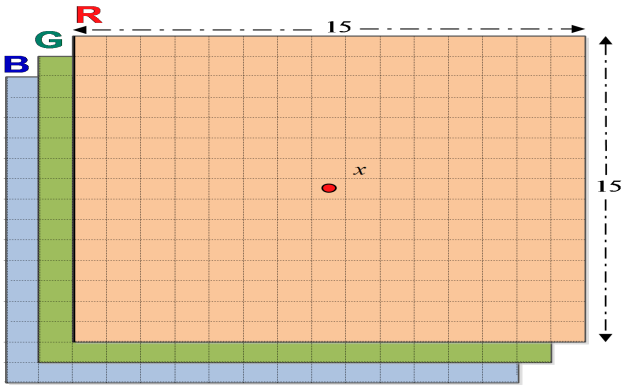

Figure 5.3: Dark channel Construction for a given Pixel x

According to (1.29), to find $W \times W$ window based dark channel of a given pixel x, as shown in Figure 5.3, it searches the minimum value in $W \times W \times 3$ *i.e.* $3 \times W^2$ pixels. This process is repeated for $M \times N$ pixels of the whole image which is computational expensive task. The dark channel image consists of rectangular patches of duplicate values due to window based local minimum operation as shown in Figure 5.4. Since the dark

(a) (b)

Figure 5.4: Dark channel Construction for a given Pixel. (a) Input Image (b) Its dark channel image.

channel image consists of redundant local minimum values, therefore in this work, for a given image, dark channel estimation is applied in such a way that it minimizes the redundant calculations along with preserving the local minimum value in a window.

- First, a RGB foggy image I of size $M \times N$ is divided into non overlapping s_b blocks of fixed size (B_1, B_2.., B_i.....B_{s_b}) of size $5 \times 5 \times 3$ as shown in Figure 5.5.

Figure 5.5: Division of a RGB image I into fixed size blocks.

- Then, a $2D$ down sampled image I_{ds} is created in such a way that each pixel in I_{ds} is obtained from each respective block B_i by taking the minimum in the respective block as

$$I_{ds}(x) = min(B_i), \quad i = 1, 2, 3, ...s\_b \tag{5.4}$$

  The number of pixels in I_{ds} is equal to s_b. Here min specifies the mathematical operation to find the minimum intensity value in a block B_i.

- After obtaining I_{ds}, its window based dark image I_{ds}^{dark} is estimated as

$$I_{ds}^{dark}(x) = min_{y \in \Omega(x)}(I_{ds}(y)) \tag{5.5}$$

  Here Ω is the window of size 3×3.

- After this, nearest neighboring up sampling of I_{ds}^{dark} is performed to obtain the equivalent dark channel image. Now, this dark channel image will be utilized to estimate the transmission map.

5.3.2 Atmospheric Light Estimation

According to [33], 0.1% brightest pixels from a dark channel image represent most fog opaque region of a foggy image which can be considered as the best region for atmospheric light estimation. According to physical model (1.11), the scene point value of a foggy image approaches to global atmospheric light in the regions of infinite depth. Consider (1.11):

$$I(x) = L_0(x) \times t(x) + L_A \times (1 - t(x))$$

Where $t(x) = e^{-\beta \times d(x)}$. For the pixel x of infinite depth ($d(x) \to \infty$), and hence $e^{-\beta \times d(x)} \to 0$, therefore,

$$I(x) \approxeq L_A \qquad or \qquad L_A \approxeq I$$

The regions of infinite depth generally lie at the top portion of an image. Therefore, in this work, to save the computational time, L_A is found from the dark channel of top 25% image rows. The rows are extracted and their

corresponding dark channel image is found by using (1.29). According to He *et al.* [33] brighter regions in the dark channel image better represents atmospheric light. But such regions may contain bright objects (*e.g.* train headlights, traffic lights *etc.*), therefore these regions can become invalid for the process of global atmospheric light estimation. Such objects can be filtered out by applying 3-σ rule on YUV components of this region [55]. The YUV color space is derived from RGB space. It comprises the luminance (Y) and two color difference (U, V) components. Luminance is a photometric measure of the luminous intensity per unit area of light travelling in a given direction. It describes the amount of light that passes through, is emitted from, or is reflected from a particular area, and falls within a given solid angle. The luminance is computed as a weighted sum of red, green and blue components; the color difference, or chrominance, components are formed by subtracting luminance from blue and from red. The advantage of this model is decoupling of luminance and color information. According to Kansal *et al.* [55], if a pixel x belongs to the region of bright light source, each or all Y, U and V channel values for this pixel are very high. With the help of this fact, such regions can be filtered prior to atmospheric light estimation by using [55]. After identifying the brighter pixels from the selected foggy image portion, their corresponding dark channel values are set equal to zero, so that they must not be selected as the candidates of atmospheric light. Finally, the values in R, G, B color channels corresponding to 0.1% brightest pixels from the dark channel image are selected as the value of global atmospheric light L_A.

5.3.3 Fusion based Transmission Estimation

The images recovered by using transmission map estimated in DCP (1.31) contain blocking artifacts or halo artifacts around the edges as shown in Figure 5.6 (c). These artifacts are generated because the transmission is directly estimated from window based dark channel with window size 15×15. In Figure 5.6 (e), 1×1 window is taken which does not produce halo artifacts, but the smaller window generates brighter transmission map and hence darker de-fogged images. Therefore, a serious color distortion can be observed in Figure 5.6 (e). Hence, it can be concluded that window size plays a major role in dark channel prior de-fogging techniques. For larger windows, the dark channel prior phenomenon becomes better because the chance of a patch containing dark pixel is increased [33]. On the other side, for a larger window, the fact that transmission values are constant in a local window turns out less appropriate, which produces color distortion in the de-fogging results. Therefore, in this work, both, 15×15 and 1×1 dark channels are utilized for improving transmission map.

Since the dark channel consists of rectangular blocks [33], therefore false high frequency information is stored in the de-fogged image as shown in Figure 5.6 (c). Alternatively, it can be said that, smoother part or low frequency component of a dark channel represents a real transmission map. But at the same time, it does not preserve the original image details like edges *etc.* As discussed above, 1×1 dark channel preserves the image details as shown in Figure 5.6 (e). Therefore, in this work, low pass component of the final transmission map is obtained by fusing the low frequency components of 15×15 and 1×1 dark channels as explained below. High pass component of final transmission map is directly taken from high pass component of 1×1 dark channel because it preserves the

image details as discussed above. Here 1×1 dark channel is also referred to as minimum color channel (I^{min}). Low and high frequency components obtained are then fused to obtain the final transmission map.

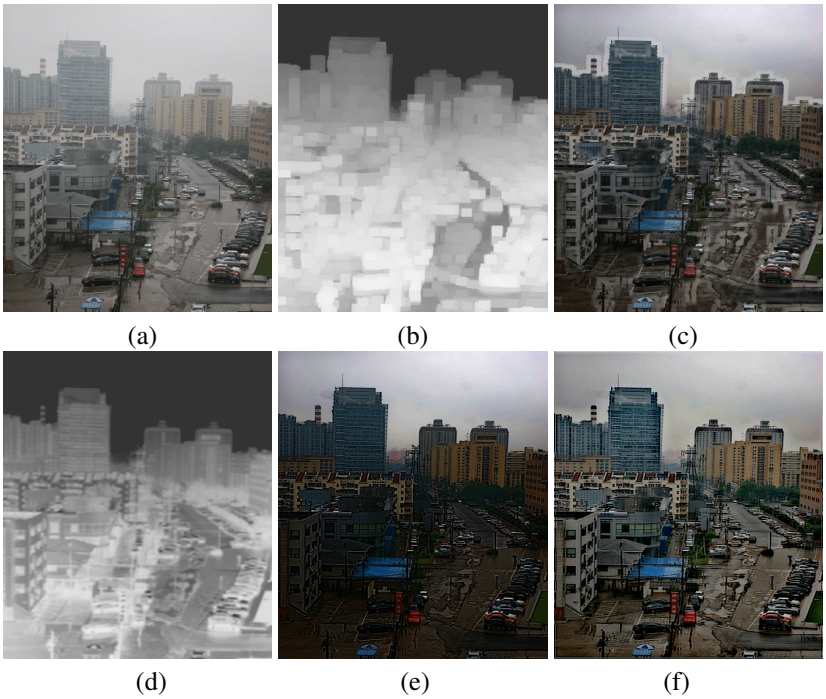

Figure 5.6: Phenomenon of halo artifact. (a) Input foggy image. (b) Transmission maps estimated using patch dark channel prior with patch size of 15×15 (d) Transmission maps estimated using minimum color channel. (c) and (e) are de-fogged images produced using transmission maps in (b) and (d). (f) De-fogged image produced by proposed weighted transmission

Low frequency components of 15×15 and 1×1 dark channel are fused in such a way that the halo artifacts become weak in the resulting low pass components. To do this, we have modified Shiau *et al's* [109] technique. To weaken the halo artifacts, Shiau took the weighted average of 15×15 and 1×1 dark channels. But in their technique, the maximum weight is given to 1×1 dark channel, due to which serious color distortion problem exists in the de-fogged images as discussed above. Therefore in this technique, weights of both the channels for each pixel are adaptively adjusted according to strength of halo artifact at that pixel. Shiau *et al.* estimated the regions of halo artifacts by using difference prior method. Difference prior estimates the difference between 1×1 (I^{min}) and 15×15 (I^{dark}) dark channels to find the regions of halo artifacts [109]. In this work, the normalized difference is found from low frequency components of both the dark channels to find the strength of halo artifact $Halo\_strength(x)$ at a given pixel x in the low pass components as:

$$Halo\_strength(x) = \frac{LP(I^{min}(x)) - LP(I^{dark}(x))}{LP(I^{min}(x))} \tag{5.6}$$

Here LP denotes the respective low pass sub-bands obtained by applying $DTCWT$ transform on minimum color channel (I^{min}) and the dark channel (I^{dark}). Larger is the value of $Halo\_strength(x)$, the halo artifacts appear more prominent which can be observed in Figure 5.7(d). Shiau *et al.* took the weighted average of I^{min} and I^{dark}

to mitigate the halo artifact with fixed weights but in the proposed technique, weight at each pixel x is equal to the strength of halo artifact at that pixel. The adaptive weights are then used to find the weighted average of low pass components of I^{min} and I^{dark}

$$LP(I^{'dark}(x)) = LP(I^{dark}(x)) \times (1 - Halo\_strength(x)) + LP(I^{min}(x)) \times Halo\_strength(x) \quad (5.7)$$

Since, the value of $Halo\_strength(x)$ lies in the range [0, 1], therefore (5.7) signifies that the pixels, where the

(a) (b) (c) (d)

Figure 5.7: (a) Input images. (b) Minimum color channel (c) Dark Channel (d) Difference between minimum color channel and dark channel.

halo artifact is strong are modified by giving more weight to I^{min} and less weight to I^{dark} depending upon the value of halo artifact strength and vice versa. By doing this, the halo artifact strength becomes weak in $I^{'dark}$ and hence reduces the transmission overestimation problem around the edges. After this, Gaussian blur is applied to $LP(I'^{dark})$ in order to smoothen out the left weakened halo artifacts in $LP(I'^{dark})$. Figure 5.8 shows the block diagram of the proposed transmission estimation process. The process flow starts from the estimation of minimum color channel and the dark channel. Before this, minimum color channel is pre-processed with Gaussian filter to remove the texture details [70]. $DTCWT$ has been used to transform minimum color channel and the dark channel in spatial frequency domain. Since dark channel contains false edges as explained above, therefore, a low pass filter is applied on high pass sub-bands of I^{dark}. Whereas, minimum color channel retains the edge details of an image, therefore, a high pass filter is applied to high pass sub-bands of I^{min}. To enhance the details in the de-fogged image, high pass filtered component of I^{min} is enhanced by simply multiplying it with a constant. Then, the high pass sub-bands of both I^{min} and I^{dark} are summed up to obtain the final high pass sub-bands. Low pass sub-bands are obtained by using (5.7). Finally, an inverse $DTCWT$ is applied to the respective low and high pass sub-bands to obtain I'^{dark}. Transmission map t is then estimated by using the modified dark channel I'^{dark}.

5.3.4 Image Restoration and Post Processing

The values of global atmospheric light L_A and the transmission map t are obtained by using the process explained in Sections 5.3.2 and 5.3.3. $L_0^c(x)$ is found by using:

$$L_0^c(x) = L_A^c + \frac{I^c(x) - L_A^c}{max(t(x), t_0)}$$

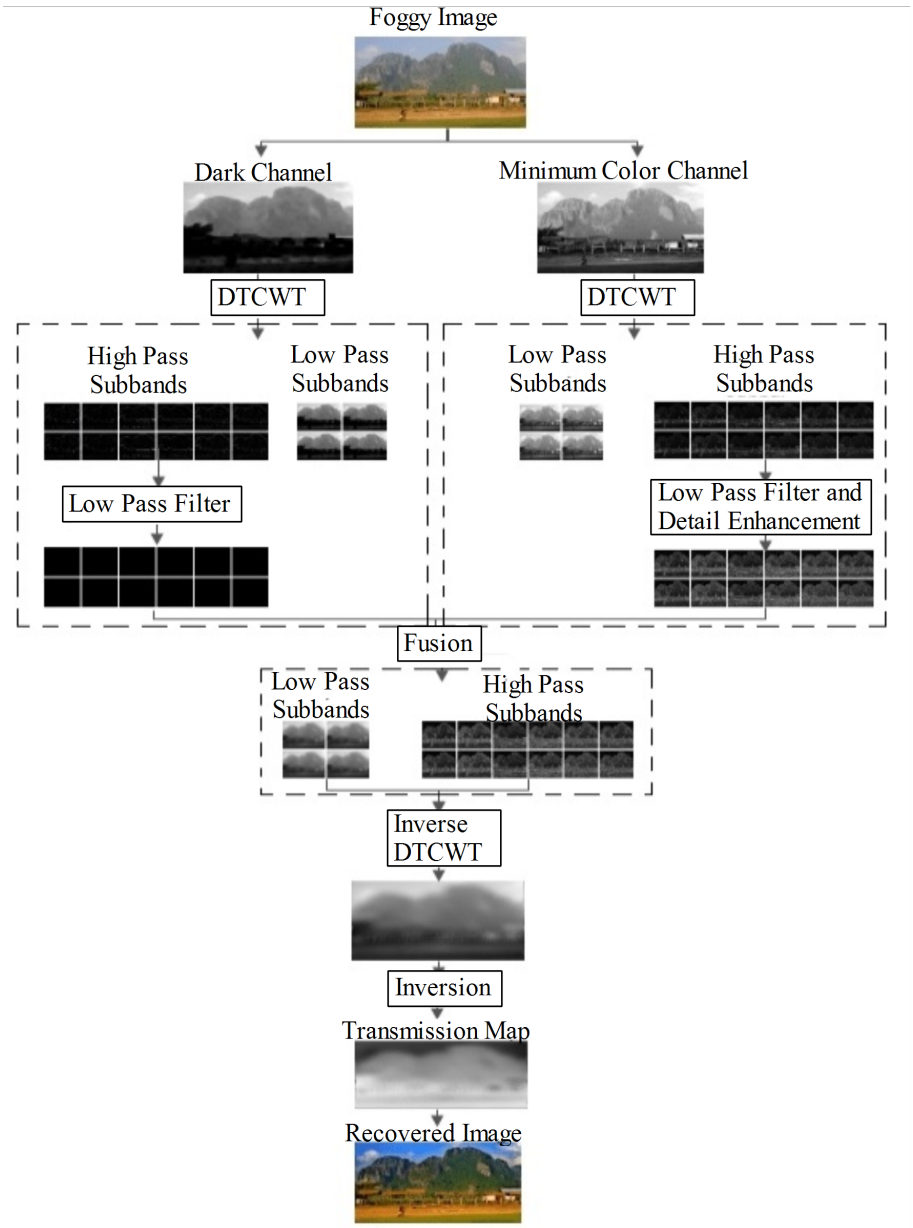

Figure 5.8: Block Diagram of Transmission Map estimation.

$L_0^c(x)$ is then recovered by putting the values of $I(x)$, $t(x)$ and L_A in (1.32). Here t_0 is the lower bound set on transmission *t(x)* for avoiding it to become zero or negative. $t_0 = 0.1$ is taken from [33].

Since, foggy images are affected by the environment lightening, some parts of the de-fogged images may suffer from low brightness and due to dark channel prior based image restoration, de-fogged images will be even more darker. Therefore, in this technique, a combined color channel transmission map is used to identify under exposed (low contrast) regions and an adaptive post processing technique is used to enhance such regions without making any color distortion. Since, for each color channel in RGB image, the low and high intensity values represent its darker and brighter regions. To identify the overall darker regions in a RGB image, the combined

color channel darkness effect $C^d(x)$ for each pixel is estimated in [46] by using

$$C^d(x) = (1 - \frac{L_0^R(x)}{max(L_0^R)}) \times (1 - \frac{L_0^G(x)}{max(L_0^G)}) \times (1 - \frac{L_0^B(x)}{max(L_0^B)}) \tag{5.8}$$

Here L_0 is the de-fogged image, max is the mathematical operator to find the maximum value in each color channel of a RGB image. Now, C^d is normalized in the range $[0, 1]$ to obtain a normalized combined color channel darkness effect C_n^d by using

$$C_n^d(x) = \frac{C^d(x) - min(C^d)}{max(C^d) - min(C^d)} \tag{5.9}$$

The value of C_n^d is highest in the darkest region and vice versa. Finally, the enhanced de-fogged image L_0' is obtained by using

$$L_0'(x) = L_0(x) \times exp^{(C_n^d(x) \times v)} \tag{5.10}$$

Here v is the scaling factor to adjust the brightness of an image. exp is the exponential operator which abruptly increases C_n^d values of darker regions while keeping the brighter region's low. In this work, v is adaptively found by estimating the difference between the average brightness of the dark region and the bright region by using:

$$v = 1 - \frac{{L_{av}}^d}{{L_{av}}^b} \tag{5.11}$$

Here ${L_{av}}^d$ and ${L_{av}}^b$ are the average intensities of the darker and the brighter regions of L_0 respectively. L_0 is separated to dark and bright regions by using Otsu's method [90]. Large difference between ${L_{av}}^d$ and ${L_{av}}^b$ represents higher degree of non uniformity in the de-fogged image L_0, therefore smaller is the value of $\frac{{L_{av}}^d}{{L_{av}}^b}$. Therefore, in (5.11), inversion operation is carried out to find high value v for darker images and vice versa. The effect of post processing can be observed in Figure 5.9.

(a) (b) (c)

Figure 5.9: The effect of post processing (a)Input Image. De-fogging Results of the proposed technique (b) Without Post Processing (c) With Post Processing.

5.3.5 Algorithm of Fusion based Image De-fogging Technique using *DTCWT*

The steps involved in procedure of fusion based image de-fogging technique using $DTCWT$ have been summarized in the Algorithm 5.1:

Algorithm 5.1: Fusion based Image De-fogging Technique using *DTCWT*.

i Obtain image I' by extracting top 25% image rows of I. Find dark channel image I'^{dark} from I' by using the procedure explained in Section 5.3.1. Finally, obtain L_A^c from I'^{dark} by using the procedure explained in Section 5.3.2.

ii To find the transmission map t, follow the steps:

ii.a Find I^{min} and I^{dark} from the normalized foggy image $(\frac{I^c(x)}{L_A^c})$.

ii.b Apply $DTCWT$ independently on I^{min} and I^{dark} to obtain the low and high pass sub-bands, $LP_i(I^{min}),\ LP_i(I^{dark})\ \ i \in 1, 2.., 4$ and $HP_i(I^{min}),\ HP_i(I^{dark})\ \ i \in 1, 2.., 12$ respectively. Here i represents number of low and high pass components obtained after applying $DTCWT$. As discussed in Section 5.2, 4 low pass and 12 high pass sub-bands are obtained in case of $2D$ data.

ii.c Estimate $Halo\_strength_i(x)$ for each low pass sub-band (LP_i) generated from I^{min} and I^{dark} by using (5.6) of Section 5.3.3.

ii.d Estimate weighted low pass sub-bands (LP_i') of the resultant dark channel image (I'_{dark}) corresponding to each low pass sub-band (LP_i) of I^{min} and I^{dark} by using (5.7) of Section 5.3.3.

ii.e Apply Gaussian blur to each low pass sub-band (LP_i') obtained in above step to produce (LP'_{G_i}).

ii.f Estimate resulting high pass sub-bands (HP_i') of the resultant dark channel image (I'_{dark}) corresponding to each high pass sub-band (HP_i) of I^{min} by multiplying with a constant k.

ii.g Apply inverse $DTCWT$ on the resultant low and high pass sub-bands to obtain the refined normalized dark channel $I^{'dark}$.

ii.h Find the transmission map by replacing I^{dark} with I'^{dark} in (1.31).

iii Obtain the de-fogged image L_0^c from I, L_A^c and t by using (1.32).

iv Obtain the post processed image $L_0^{c'}$ from L_0^c by using the procedure described in Section 5.3.4.

5.4 Experimental Results and Analysis

Proposed technique has been implemented in $MATLAB$ 2016 and tested on various standard foggy images of Choi's database [19] and Waterloo *IVC* dehazed image database [74]. These databases contain many hazy and foggy images taken in different type of environments. There are number of images reflecting lightening conditions of different day times. In next section the results of various techniques have been shown on images including $foggy\_building2$ which is a distant image taken in morning time hazy and cloudy conditions. $Y1$ and $Y16$ are also a hazy images showing number of mountains. $Aerial$ is the satellite image showing a large Earth's area which

is a different type of hazy image. $Night1$ is an evening time hazy image representing natural scene whereas $Toys$ and $People$ are day time images representing the toys and people captured in hazy conditions. $Cones$ is an image taken in wheat field during morning time in moderate fog, $Foggy\_road2$ is also a moderate fog image taken on road during day time. These images have been selected as these are capable of showing the performance of de-fogging techniques in different environments and day times. Both objective as well as subjective evaluations have been carried out to show the effectiveness of the technique.

5.4.1 Subjective Evaluation

In this Section, the results of the our technique have been visually compared with existing techniques including Fattal [23], Tarel *et al.* [114], He *et al.* [34], Cai *et al.* [17], Choi *et al.* [18], Meng *et al.* [79], Zhu *et al.* [136], Ren *et al.* [102], Liu *et al.* [73], Colores *et al.* [104], Kansal *et al.* [56] and Proposed_CAP (Technique proposed in Chapter 4) *etc.* The work done by these authors in the field of de-fogging has been explained in Chapter 3, Section 3.3.1. The subjective evaluation of the de-fogging results is done by visual perception of a de-fogged image. A good de-fogging technique produces an output image having strong contrast, real colors and similar structure as that of an input image.

Figure 5.10 shows the de-fogging results of various techniques on "$Foggy\_building2$" image. As shown in Figure 5.10 (b), Tarel *et al's* results are unnatural. The de-fogging results of He *et al.* are over dark. Cai *et al's* results are over dark in front while still foggy at the back. Choi *et al's* results are over dark as well as the color information is not reliable while Zhu *et al's* result look hazy. Ren *et al's* technique produces better de-fogging results in comparison to all but the proposed technique obtains much bright, sharp and uniform de-fogging results as shown in Figure 5.10 (h).

Figure 5.11 shows the de-fogging results of various techniques on "$Y16$" image. As shown in Figure 5.11 (b), Tarel *et al's* results look vague near the mountain regions. The mountain area of He *et al.*, Cai *et al.* and Meng *et al's* technique is also not clear. Zhu *et al's* de-fogging results still look foggy. Ren *et al's* image is good but the mountain region is blur in comparison to result of our technique.

Next, we compare the de-fogging results of the technique for "$Aerial$" image. Figure 5.12 shows a foggy image of land taken from the sky. The de-fogging results obtained by Cai *et al.*, Choi *et al.* and Zhu *et al.* are over dark. Ren *et al's* technique is based upon machine learning strategies which are effectively being used in various research fields nowadays, but they require a sufficient information to predict the effective outputs. If the adequate dataset is not available, reliable depth maps can not be obtained and so the unreliable de-fogging results as shown in Figure 5.12 (e). The de-fogging performance of Kansal *et al.* is better than the others but they are blur in comparison to our technique.

Next, results of the technique have been compared with the existing techniques for "$Y1$" image as shown in Figure 5.13. The de-fogging results obtained by Cai *et al.*, Choi *et al.* and Zhu *et al.* are over dark. Figure 5.13 (g) shows the de-fogging results of Colores *et al.*. Its de-fogging results are better but the edge information is not

clearly enhanced. As compared to other technique's, proposed technique's result is more sharp, clear and uniform.

Figure 5.14 compares the results of the technique with Zhu *et al.*, Ren *et al.*, Kansal *et al.*, Liu *et al.* and Colores *et al's* techniques. It can be clearly observed that the results of our technique are brighter and clearer as compared to other techniques. Finally, for "$Foggy\_road2$", "$Cones$", " $Night1$" and "$Toys$" images, the de-fogged images of various techniques have been shown in Figure 5.15. Our results maintain the original tone of the true scene, avoid the over-enhancement and recover more vivid color than the relevant ground truth images The overall results of the technique are impressive, reliable and accurate. The color of a de-fogged image looks natural and the contrast is better throughout the images. In the next sub-section, results of the technique are compared with other techniques from objective point of view to show the effectiveness of the technique.

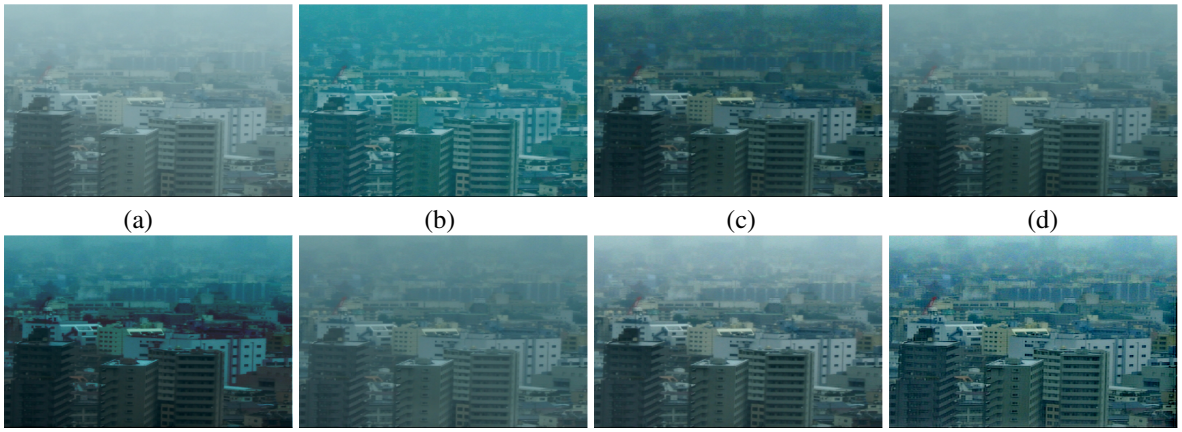

(a) (b) (c) (d)

(e) (f) (g) (h)

Figure 5.10: De-fogging results (a) Input foggy images "$Foggy\_building2$". De-fogging results of (b) Tarel *et al.* (c) He *et al.* (d) Cai *et al.* (e) Choi *et al.* (f) Zhu *et al.* (g) Ren *et al.* (h) Proposed.

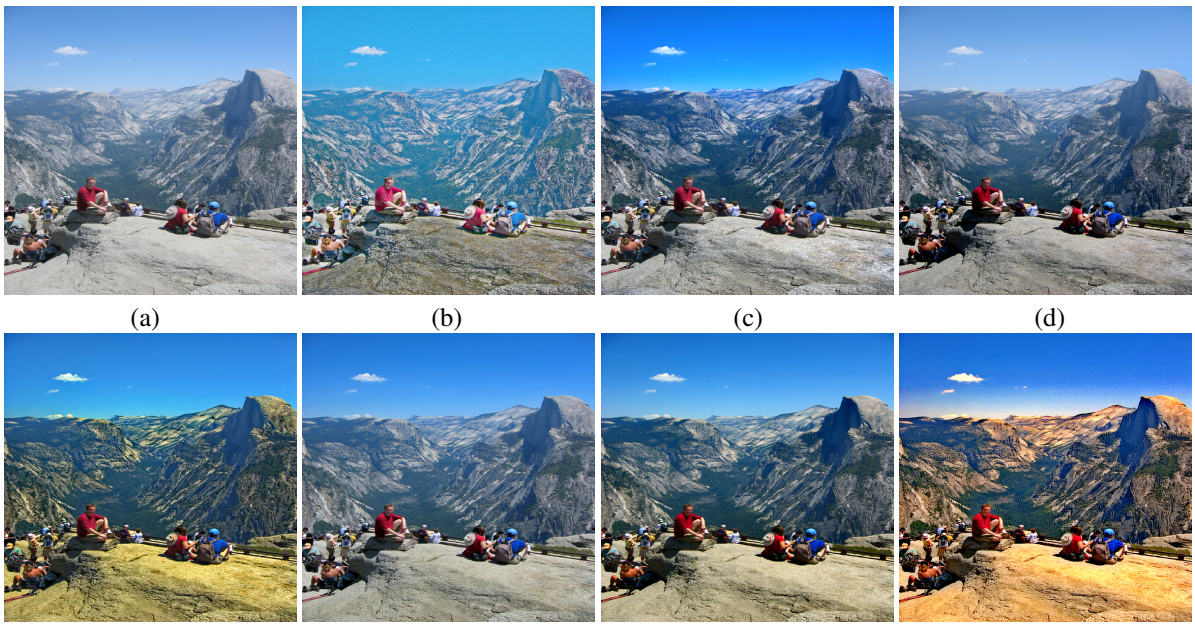

(a) (b) (c) (d)

(e) (f) (g) (h)

Figure 5.11: De-fogging results (a) Input foggy images "$Y16$". De-fogging results of (b) Tarel *et al.* (c) He *et al.* (d) Cai *et al.* (e) Meng *et al.* (f) Zhu *et al.* (g) Ren *et al.* (h) Proposed.

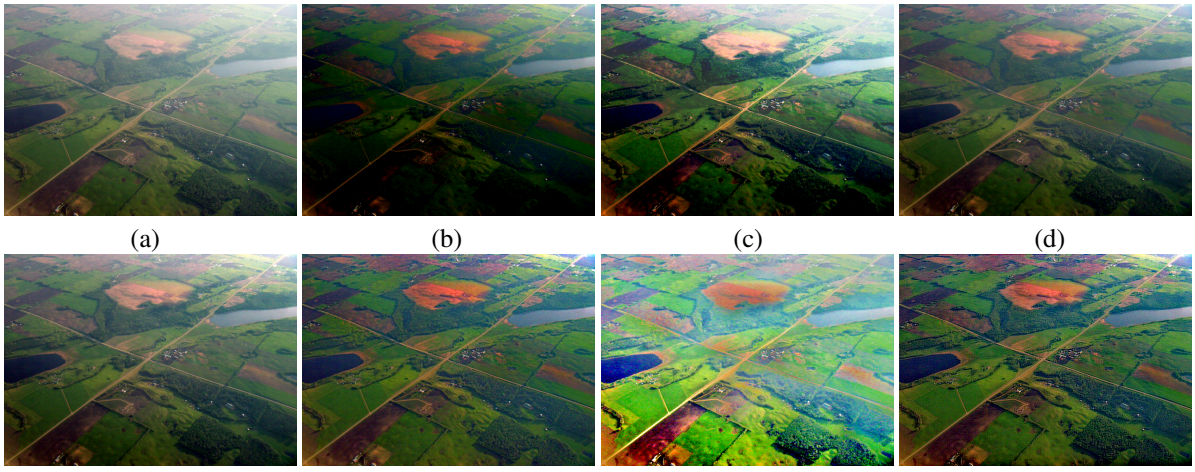

Figure 5.12: De-fogging results (a) Input foggy image "$Aerial$". De-fogging results of (b) Cai *et al.* (c) Choi *et al.* (d) Zhu *et al.* (e) Ren *et al.* (f) Kansal *et al.* (g) Proposed_CAP (h) Proposed.

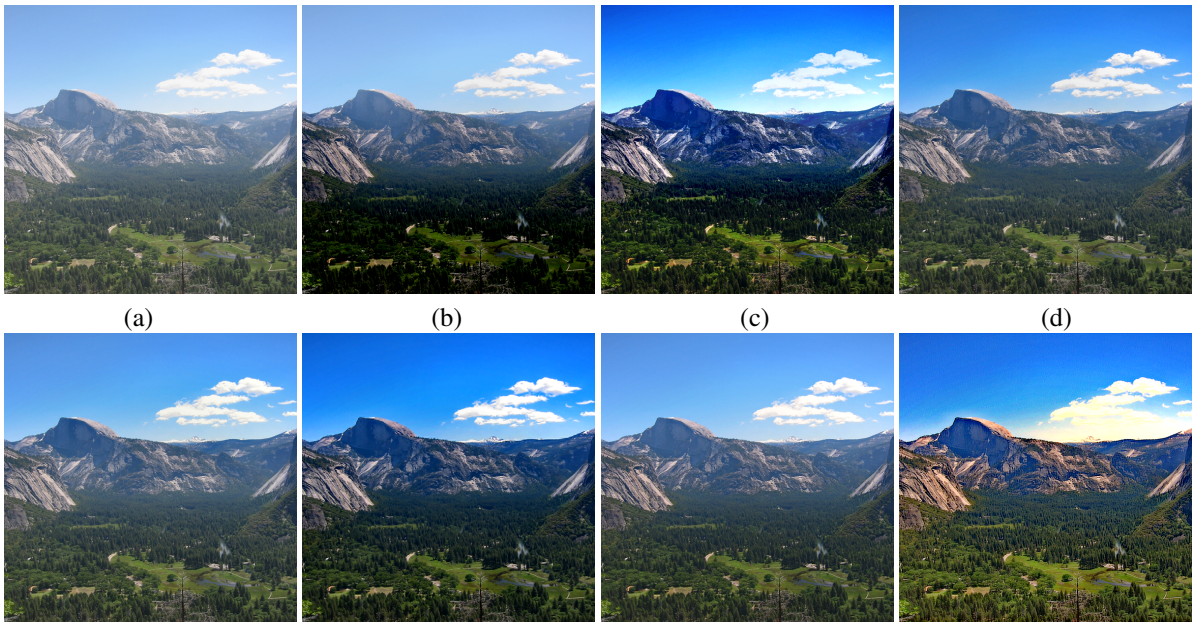

Figure 5.13: De-fogging results (a)Input foggy image "$Y1$". De-fogging results of (b) Cai *et al.* (c) Choi *et al.* (d) Zhu *et al.* (e) Ren *et al.* (f) Liu *et al.* (g) Colores *et al.* (h) Proposed.

5.4.2 Objective Evaluation

The final restoration results of the proposed de-fogging technique have been compared with previous state-of-art techniques including Tarel *et al.*, He *et al.*, Meng *et al.*, Choi *et al.*, Zhu *et al.*, Cai *et al.*, Ren *et al.*, Liu *et al.*, Colores *et al.*, Kansal *et al.* and Proposed_CAP. For comparison, 15 standard foggy images have been taken from databases [19] and [74]. To ensure comparability of various de-fogging techniques, descriptive variables or metrics for judging the output image quality are necessary. In this work, six different quality parameters including r, CNI, FRF, VCM, CI and CIE have been considered as shown in Tables 5.3-5.8. A better de-fogging technique achieves higher values of the above factors.

Figure 5.14: De-fogging results (a)Input foggy image "$People$". De-fogging results of (b) Zhu *et al.* (c) Ren *et al.* (d) Kansal *et al.* (e) Proposed_CAP (f) Liu *et al.* (g) Colores *et al.* (h) Proposed.

It can be seen that the proposed technique attains highest average value of r in comparison to other techniques including the minimum preserving subsampling and CAP based proposed de-fogging techniques. Proposed_CAP technique is slightly than our $DTCWT$ based technique in terms of CNI and CIE, but at the same time its VCM is very less. Choi *et al's* technique also performs slightly better than that of our $DTCWT$ based technique in FRF and CI but its r, CNI, VCM and CIE are very less.

The technique improves DCP and the proposed minimum preserving subsampling based image de-fogging by incorporating multiple patch sizes of dark channel and minimum preserving subsampling based dark channel estimation. The overall percentage improvement achieved by the technique with respect to DCP [34] is 85.33% in r, 7.35% in CNI, 29.34% in FRF, 37.94% in VCM, 7.92% in CI, 2.48% in CIE and with Kansal *et al.* [56] is 36.95 in r, 2.81 in CNI, 30.77 in FRF, 21.14 in VCM, 0.95 in CIE. However there is a decrease of -25.88 in CI, but at the same time other factors have been improved significantly. Also, the maximum percentage improvement achieved by the technique with respect to other techniques is 141.74% in r, 17.74% in CNI, 131.07% in FRF, 41.38% in VCM, 39.73% in CI, 7.06% in CIE. The minimum percentage improvement achieved by the technique with respect to other techniques is 24.33% in r, 2.81% in CNI, 1.28% in FRF, 13.10% in VCM, 19.38% in CI, 0.95% in CIE.

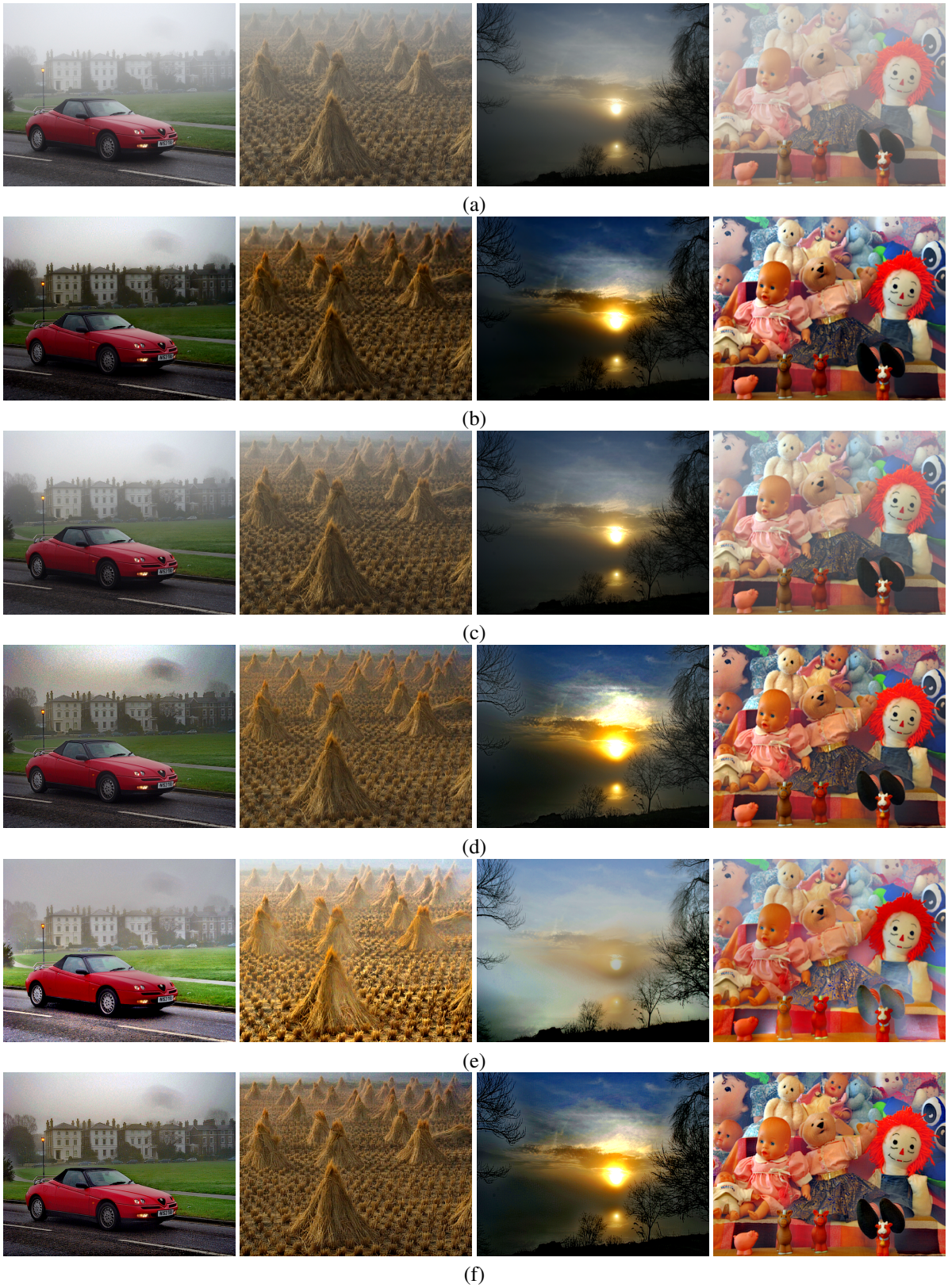

Figure 5.15: De-fogged results on "$Foggy\_road2$", "$Cones$", "$Night1$", "$Toys$" (Top-Row, Left-Right) (a)Input foggy images. De-fogging results of (b) Liu *et al.* (c) Colores *et al.* (d) Kansal *et al.* (e) Proposed_CAP (f) Proposed

Table 5.3: Comparison of the proposed technique with existing techniques on the basis of r

	Tarel *et al.* [114]	He *et al.* [34]	Meng *et al.* [79]	Choi *et al.* [18]	Zhu *et al.* [136]	Cai *et al.* [17]	Ren *et al.* [102]	Liu *et al.* [73]	Colores *et al.* [104]	Kansal *et al.* [56]	Proposed_CAP	Proposed
City1	2.21	1.37	2.03	1.61	1.14	1.14	1.17	1.35	1.14	1.70	2.06	2.56
Night1	2.69	0.71	1.12	1.20	0.86	0.64	0.94	1.15	1.02	1.75	2.06	2.54
Landscape3	1.34	1.00	1.13	1.35	1.08	0.94	1.09	1.06	1.07	1.18	1.46	1.76
Foggy_building1	2.31	1.67	3.18	1.39	1.22	1.27	1.23	1.79	1.20	2.42	2.33	3.13
Foggy_road1	2.31	1.49	2.36	1.78	1.24	1.08	1.45	1.69	1.30	2.37	2.66	3.62
Foggy_road2	2.28	1.48	2.56	1.43	1.14	1.01	1.17	1.35	1.12	2.02	1.52	2.69
Cones	1.88	1.59	1.61	1.66	1.13	1.38	1.22	1.35	1.20	1.62	1.79	2.42
Cityscape	5.08	3.68	5.18	1.88	1.47	1.81	1.79	3.13	1.55	3.47	1.96	3.75
Foggy_ground	2.99	1.23	2.44	2.13	1.16	1.25	1.30	1.46	1.21	1.94	4.77	3.57
People	1.81	1.16	1.37	1.42	1.11	1.07	1.10	1.29	1.25	1.37	1.74	2.09
Foggy_building2	1.86	1.33	2.78	1.29	1.04	1.10	1.50	1.62	1.23	3.63	2.04	3.00
Toys	2.04	2.05	2.34	1.95	1.51	1.62	1.52	2.19	1.51	2.26	1.87	3.02
Y1	1.66	1.24	1.35	1.53	1.13	0.94	1.10	1.27	1.10	1.56	2.07	2.72
Y16	1.88	1.44	1.67	1.48	1.22	1.19	1.33	1.53	1.35	1.64	1.44	2.30
Aerial	1.82	1.04	1.46	1.67	1.06	0.76	1.17	1.27	1.09	1.52	2.30	2.52
Average	**2.28**	**1.50**	**2.17**	**1.58**	**1.17**	**1.15**	**1.27**	**1.57**	**1.22**	**2.03**	**2.14**	**2.78**

Table 5.4: Comparison of the proposed technique with existing techniques on the basis of CNI

	Tarel *et al.* [114]	He *et al.* [34]	Meng *et al.* [79]	Choi *et al.* [18]	Zhu *et al.* [136]	Cai *et al.* [17]	Ren *et al.* [102]	Liu *et al.* [73]	Colores *et al.* [104]	Kansal *et al.* [56]	Proposed_CAP	Proposed
City1	0.62	0.54	0.53	0.58	0.50	0.53	0.53	0.58	0.52	0.55	0.65	0.60
Night1	0.92	0.77	0.78	0.78	0.68	0.79	0.66	0.95	0.66	0.91	0.62	0.95
Landscape3	0.97	0.96	0.92	0.99	0.93	0.98	0.49	0.97	0.94	0.97	0.91	1.00
Foggy_building1	0.74	0.63	0.54	0.45	0.45	0.47	0.53	0.52	0.44	0.63	0.75	0.62
Foggy_road1	0.61	0.52	0.51	0.62	0.48	1.00	0.51	0.50	0.44	0.52	0.76	0.53
Foggy_road2	0.57	0.50	0.52	0.51	0.48	0.46	0.51	0.47	0.48	0.51	0.54	0.55
Cones	0.731	0.73	0.69	0.80	0.57	0.73	0.60	0.81	0.63	0.93	0.89	0.80
Cityscape	0.59	0.57	0.60	0.53	0.54	0.42	0.61	0.58	0.58	0.57	0.66	0.60
Foggy_ground	0.79	0.59	0.57	0.51	0.53	0.59	0.59	0.62	0.55	0.59	0.79	0.60
People	0.89	0.83	0.89	0.88	0.67	0.67	0.79	0.82	0.67	0.85	0.85	0.93
Foggy_building2	0.85	0.97	0.83	1.00	0.75	0.63	0.64	0.97	0.63	0.98	0.70	0.95
Toys	0.73	0.85	0.82	0.76	0.68	0.65	0.63	0.85	0.64	0.85	0.80	0.90
Y1	0.74	0.46	0.65	0.25	0.75	0.75	0.81	0.29	0.74	0.43	0.76	0.44
Y16	0.78	0.63	0.76	0.63	0.86	0.94	0.73	0.50	0.78	0.76	0.83	0.72
Aerial	0.79	0.69	0.64	0.70	0.57	0.64	0.54	0.70	0.55	0.75	0.88	0.79
Average	**0.75**	**0.68**	**0.68**	**0.67**	**0.63**	**0.68**	**0.61**	**0.68**	**0.62**	**0.72**	**0.76**	**0.73**

Table 5.5: Comparison of the proposed technique with existing techniques on the basis of FRF

	Tarel *et al.* [114]	He *et al.* [34]	Meng *et al.* [79]	Choi *et al.* [18]	Zhu *et al.* [136]	Cai *et al.* [17]	Ren *et al.* [102]	Liu *et al.* [73]	Colores *et al.* [104]	Kansal *et al.* [56]	Proposed_CAP	Proposed
City1	1.35	1.19	1.38	2.33	0.72	2.75	1.89	1.75	0.68	1.23	2.11	2.90
Night1	2.15	1.61	1.61	2.11	2.15	2.90	0.20	2.47	1.62	1.53	0.85	2.68
Landscape3	0.51	0.53	0.38	0.62	0.62	1.12	-2.23	0.61	0.44	0.53	0.16	0.85
Foggy_building1	3.06	3.25	3.37	4.85	1.53	3.75	3.7	3.34	1.27	3.35	4.38	4.43
Foggy_road1	2.40	2.26	2.16	3.71	1.05	3.82	1.47	2.94	1.07	2.37	2.94	2.89
Foggy_road2	1.71	1.61	1.64	2.86	1.49	2.87	1.11	2.26	0.91	1.68	1.80	2.54
Cones	1.37	1.74	1.54	2.27	0.85	1.94	0.88	2.03	1.08	1.72	1.78	1.93
Cityscape	2.58	2.66	2.96	3.04	1.15	2.04	1.89	2.46	1.42	2.62	2.86	2.74
Foggy_ground	3.69	3.35	2.81	3.38	1.82	4.26	1.26	3.81	1.60	3.47	3.99	3.49
People	0.93	0.91	1.09	2.02	0.53	1.40	0.97	1.08	0.75	0.94	1.18	1.71
Foggy_building2	2.83	2.45	2.26	2.62	1.68	1.60	1.41	2.62	1.16	2.23	2.90	2.52
Toys	1.12	2.04	1.98	2.02	1.24	1.73	1.13	2.13	1.05	2.06	1.95	2.22
Y1	1.17	1.58	1.47	1.63	1.17	2.25	0.91	1.71	0.93	1.48	1.54	1.66
Y16	0.89	0.94	1.06	1.41	0.76	0.72	0.96	1.20	0.73	0.90	1.15	1.34
Aerial	1.41	1.11	0.99	1.77	1.01	2.07	0.73	1.40	0.72	1.17	1.27	1.39
Average	**1.81**	**1.82**	**1.78**	**2.44**	**1.18**	**2.35**	**1.08**	**2.12**	**1.03**	**1.82**	**2.06**	**2.35**

Table 5.6: Comparison of the proposed technique with existing techniques on the basis of VCM

	Tarel *et al.* [114]	He *et al.* [34]	Meng *et al.* [79]	Choi *et al.* [18]	Zhu *et al.* [136]	Cai *et al.* [17]	Ren *et al.* [102]	Liu *et al.* [73]	Colores *et al.* [104]	Kansal *et al.* [56]	Proposed_CAP	Proposed
City1	68.83	46.00	54.17	66.00	45.83	50.67	19.50	56.33	45.00	54.83	66.17	74.50
Night1	37.00	30.17	42.67	53.50	37.50	29.33	54.33	52.50	43.50	30.00	49.67	38.67
Landscape3	48.59	45.78	49.06	51.56	47.97	45.00	20.63	47.97	47.19	48.13	41.09	51.72
Foggy_building1	35.50	21.33	32.33	49.83	48.17	52.00	57.17	34.17	47.17	31.67	54.17	39.50
Foggy_road1	28.65	29.81	37.12	35.77	53.65	58.08	49.42	36.54	24.42	36.73	41.35	49.04
Foggy_road2	48.27	25.38	35.77	40.00	27.50	26.92	52.50	34.81	25.58	33.08	56.15	53.27
Cones	67.98	61.40	69.08	75.44	47.81	56.80	49.34	63.60	47.59	61.62	59.43	81.58
Cityscape	56.62	58.98	73.87	37.39	59.17	33.58	31.58	52.45	57.35	52.99	25.77	58.26
Foggy_ground	43.57	30.54	36.07	47.50	29.11	30.71	28.04	31.07	27.68	35.36	16.25	47.14
People	86.60	79.43	76.56	83.97	76.32	75.84	75.12	81.34	77.03	79.19	78.95	89.23
Foggy_building2	38.60	23.31	39.10	21.05	45.36	50.88	30.83	33.83	56.64	61.90	35.59	52.63
Toys	55.56	69.01	70.96	67.06	50.88	53.61	53.22	72.71	49.71	70.76	49.12	76.61
Y1	59.92	51.42	52.43	57.89	46.76	41.30	45.95	53.24	44.13	57.09	56.68	65.99
Y16	70.65	70.45	70.24	70.45	65.59	64.37	68.42	70.45	67.81	72.06	63.97	74.09
Aerial	38.35	18.61	34.96	49.62	15.98	47.56	22.93	34.77	18.23	28.01	36.65	60.53
Average	**52.31**	**44.11**	**51.63**	**53.80**	**46.51**	**47.78**	**43.93**	**50.39**	**45.27**	**50.23**	**48.73**	**60.85**

Table 5.7: Comparison of the proposed technique with existing techniques on the basis of CI

	Tarel *et al.* [114]	He *et al.* [34]	Meng *et al.* [79]	Choi *et al.* [18]	Zhu *et al.* [136]	Cai *et al.* [17]	Ren *et al.* [102]	Liu *et al.* [73]	Colores *et al.* [104]	Kansal *et al.* [56]	Proposed_CAP	Proposed
City1	23.36	13.47	14.91	16.83	11.65	13.35	11.84	13.84	12.07	34.75	18.75	15.12
Night1	52.77	28.19	26.30	33.66	24.74	26.82	21.01	41.14	26.37	31.16	31.35	52.12
Landscape3	67.44	61.99	62.03	79.47	59.47	63.99	61.17	62.79	59.97	67.44	67.82	67.34
Foggy_building1	29.69	19.93	19.34	16.73	11.17	12.13	10.38	15.01	10.61	39.37	17.52	20.62
Foggy_road1	33.72	20.76	21.97	27.99	18.14	48.28	18.81	21.57	18.00	49.74	26.92	24.78
Foggy_road2	40.03	28.98	30.73	28.77	26.72	27.97	26.61	30.19	27.28	53.68	36.79	33.30
Cones	31.44	28.66	27.72	42.40	22.69	30.15	23.32	31.64	24.82	60.08	40.10	34.12
Cityscape	36.61	26.12	29.45	19.81	18.00	21.05	21.99	24.64	20.01	46.99	28.05	30.48
Foggy_ground	40.69	21.83	24.11	20.52	14.10	14.28	13.30	17.13	13.36	85.57	63.30	24.02
People	44.51	40.63	45.28	54.77	32.86	37.34	35.15	38.87	40.25	66.59	41.92	42.18
Foggy_building2	51.91	30.03	29.16	47.85	25.08	20.72	20.65	30.52	20.52	60.34	47.58	40.95
Toys	54.34	75.28	67.82	69.65	60.14	58.66	52.20	77.57	51.33	91.64	68.62	82.52
Y1	77.30	98.66	85.31	97.35	81.44	47.84	68.40	102.83	63.80	79.14	55.76	93.22
Y16	88.63	101.54	82.17	95.48	79.19	53.52	75.37	104.10	73.00	75.37	64.42	79.62
Aerial	41.78	32.62	32.82	38.46	26.53	28.83	25.28	32.39	25.27	73.47	56.63	38.04
Average	**47.61**	**41.91**	**39.94**	**45.98**	**34.13**	**33.66**	**32.37**	**42.95**	**32.44**	**61.02**	**44.37**	**45.23**

Table 5.8: Comparison of the proposed technique with existing techniques on the basis of CIE

	Tarel *et al.* [114]	He *et al.* [34]	Meng *et al.* [79]	Choi *et al.* [18]	Zhu *et al.* [136]	Cai *et al.* [17]	Ren *et al.* [102]	Liu *et al.* [73]	Colores *et al.* [104]	Kansal *et al.* [56]	Proposed_CAP	Proposed
City1	7.03	7.32	7.22	7.41	7.29	7.07	7.37	7.45	7.27	7.22	7.14	7.34
Night1	7.26	6.46	6.43	7.09	6.50	4.83	7.00	6.75	7.18	6.78	6.95	7.31
Landscape3	7.65	7.46	7.45	7.45	7.36	6.33	7.45	7.45	7.46	7.71	7.86	7.62
Foggy_building1	7.24	7.24	7.39	7.09	7.68	7.75	7.59	7.83	7.69	7.19	6.95	7.39
Foggy_road1	7.06	7.17	6.99	6.73	7.41	6.77	7.40	7.32	7.43	7.47	7.28	7.35
Foggy_road2	7.36	7.51	7.41	6.97	7.66	7.04	7.77	7.47	7.73	6.85	7.12	7.61
Cones	7.02	7.01	6.98	6.97	7.18	7.25	7.22	7.15	7.28	7.83	7.90	7.17
Cityscape	6.75	7.33	7.40	6.52	6.94	7.31	7.22	7.57	7.09	6.85	6.90	7.28
Foggy_ground	7.28	6.75	6.55	7.06	6.90	6.47	7.13	6.64	7.22	7.41	7.23	6.96
People	7.53	7.58	7.33	7.01	7.59	7.39	7.61	7.64	7.62	7.71	7.90	7.61
Foggy_building2	7.28	6.93	7.20	7.09	6.87	7.32	7.46	7.19	7.30	7.22	7.59	7.68
Toys	7.32	7.79	7.62	7.74	7.62	7.69	7.52	7.83	7.61	7.59	7.64	7.85
Y1	7.53	7.50	7.43	7.22	7.47	7.27	7.53	7.44	7.61	7.70	7.67	7.32
Y16	7.66	7.68	7.82	7.45	7.77	7.75	7.90	7.67	7.78	7.51	7.69	7.84
Aerial	7.08	6.98	6.92	7.07	7.29	5.93	7.55	7.02	7.49	7.36	7.75	7.16
Average	**7.27**	**7.25**	**7.21**	**7.12**	**7.30**	**6.94**	**7.45**	**7.36**	**7.45**	**7.36**	**7.44**	**7.43**

5.4.3 Execution Time Comparison

The execution time comparison of the proposed technique with other existing techniques has been shown in Table 5.9. For this comparison, image size, tools used for implementing the technique (*i.e* C++, MATLAB or Not Mentioned) and the type of processor are considered for each of the technique.

Table 5.9: Comparison of execution time of the proposed technique with existing techniques

Technique	**Processor**	**Tool**	**Image Size**	**Execution Time**
Tan [112]	Pentium 4	N/A	600×400	5-7min
Fattal [23]	Dual-Core	C++	512×512	35s
Tarel *et al.* [114]	Quad-Core	MATLAB	600×400	5.9s
He *et al.* [34]	Quad-Core	MATLAB	600×400	1.99s
Meng *et al.* [79]	Quad-Core	MATLAB	600×400	1.80s
Choi *et al.* [18]	Quad-Core	MATLAB	600×400	12.52s
Zhu *et al.* [136]	Quad-Core	MATLAB	600×400	0.69s
Cai *et al.* [17]	Quad-Core	MATLAB	600×400	2.00s
Ren *et al.* [102]	Quad-Core	MATLAB	600×400	1.81s
Liu *et al.* [73]	Quad-Core	MATLAB	600×400	0.25s
Colores *et al.* [104]	Quad-Core	MATLAB	600×400	0.35s
Kansal *et al.* [56]	Quad-Core	MATLAB	600×400	0.10s
Proposed_CAP	Quad-Core	MATLAB	600×400	0.12s
Proposed	Quad-Core	MATLAB	600×400	0.37s

It can be clearly seen from Table 5.9 that the processing speed of proposed technique is better than all other techniques except Kansal *et al.* and Proposed_cap techniques. But overall de-fogging performance of the technique is better than the other existing techniques which can be observed from Tables 5.3-5.8 also. It can be concluded that the technique is computational effective than that of existing techniques and at the same time, other parameters of quality have not been compromised. Finally, it can be concluded that the technique is better in achieving higher processing speed along with maintaining the overall image quality.

5.4.4 De-fogging Results on *FRIDA* with varying Fog Density

The objective quality parameters including r, CNI, FRF, VCM, CI *and* CIE have been shown for standard foggy images which shows that the technique obtains better quality de-fogged images and also effective for applying in real time scenarios. In this Section, the parameters have been evaluated on $FRIDA$ which is a dynamic database containing 66 images. By using the original clear day images, depth maps present in this database, different foggy images can be generated by varying the value of β. The de-fogging results obtained by existing

techniques for a foggy image of $FRIDA$ is shown in Figure 5.16. In Table 5.10, the average data for 330 (66 individual images and 5 different β) images for r, CNI, FRF, VCM, CI and CIE has been shown. It can be observed that the technique outperforms the existing techniques in the case of images suffering from different fog densities also.

From Table 5.10, it can be seen that the percentage improvement of the technique with respect to DCP is 68.33% in r, 18.20% in FRF, 14.19% in VCM and whereas a decrease of 0.72 in CNI and 1.26% in CI and 0.87% in CIE which are significantly very less in comparison to the achieved improvements. The percentage improvement of the technique with respect to Kansal *et al's* technique is 32.91% in r, 11.81% in FRF, 9.14% in VCM and a decrease of 1.34% in CIE, 0.72 in CNI and 0.38% in CI. This technique improves DCP and Kansal *et al's* technique, but it produces little over enhancement in case of road images during the post processing step which causes the performance to be degraded in case of these images. The maximum percentage improvement achieved by the technique with respect to existing techniques is 113.38% in r, 12.60% CNI, 211.00% in FRF, 37.33% VCM, 6.69% CI, 0.89% in CIE. The minimum percentage improvement achieved by the technique with respect to existing techniques is 5.19% in r, 4.13% in CNI, 7.25% in FRF, 6.01% VCM, 2.79% CI, 0.89% in CIE. Overall, the results produced by the technique obtain better quality de-fogged images in comparison to existing image de-fogging techniques.

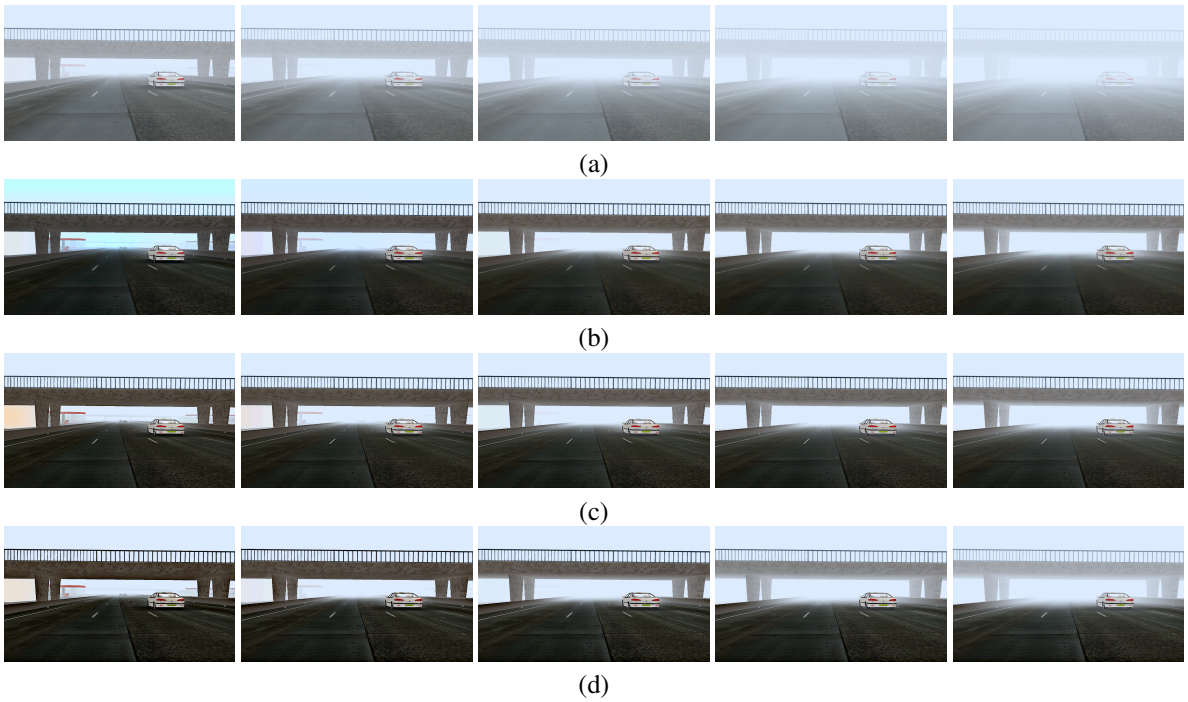

(a)

(b)

(c)

(d)

Figure 5.16: (a) Input foggy images of $FRIDA$ with $\beta = 0.02,\ 0.04,\ 0.06, 0.08,\ 0.1$ (left-right) (b) Corresponding de-fogged images obtained by He *et al's* technique, (c) Corresponding de-fogged images obtained by Kansal *et al's* technique, (d) Corresponding de-fogged images obtained by proposed technique.

Table 5.10: Comparison of r, CNI, FRF, VCM, CI and CIE of the proposed technique with existing techniques on $FRIDA(66\ Images)$ with varying fog density ($\beta = 0.02,\ 0.04, 0.06,\ 0.08, 0.1$)

	r	**CNI**	**FRF**	**VCM**	**CI**	**CIE**
Tarel *et al.* [114]	2.35	0.81	3.58	34.08	43.11	5.96
He *et al.* [34]	1.88	0.56	3.25	37.89	19.21	5.94
Cai *et al.* [17]	1.64	0.53	2.85	36.80	19.72	6.10
Choi *et al.* [18]	1.58	0.85	4.74	34.88	33.16	7.10
Meng *et al.* [79]	3.00	0.56	3.35	39.97	23.08	5.90
Zhu *et al.* [136]	1.52	0.51	1.64	33.24	17.98	6.08
Ren *et al.* [102]	1.58	0.50	1.28	31.85	18.08	5.84
Liu *et al.* [73]	2.22	0.56	3.93	40.82	18.45	6.21
Colores *et al.* [104]	1.48	0.49	1.24	31.51	17.78	6.05
Kansal *et al.* [56]	2.38	0.56	3.44	39.69	19.04	5.97
Proposed_CAP	5.07	0.84	5.37	50.38	53.93	6.42
Proposed	3.16	0.55	3.84	43.27	18.97	5.89

5.5 Conclusion of the Chapter

This Chapter proposes an effective technique of fusion based image de-fogging. In this technique, the transmission map is obtained by fusing two transmission maps by using $DTCWT$. By utilizing the directional selectivity property of $DTCWT$, the edge details of a de-fogged image are enhanced. It can effectively remove halo artifacts as shown in de-fogged images. In addition to this, cost of the de-fogging process is also reduced by finding the dark channel with a down sampling approach. This technique improves DCP and the proposed minimum preserving subsampling based image de-fogging by incorporating multiple patch sizes of dark channel and minimum preserving subsampling based dark channel estimation. The overall percentage improvement achieved by this technique with respect to DCP is 81.29% in r, 7.36% in CNI, 29.34% in FRF, 37.95% in VCM, 7.92% in CI, 2.48% in CIE and with Kansal *et al.* is 35.09 in r, 2.81 in CNI, 21.14 in FRF, 30.77 in VCM, 0.95 in CIE. Also, the maximum percentage improvement achieved by the technique with respect to other compared techniques is 80.67% in r, 17.74% in CNI, 131.07% in FRF, 41.38% in VCM, 39.72% in CI, 7.06% in CIE and the minimum percentage improvement is 24.33% in r, 2.81% in CNI, 12.76% in FRF, 13.10% in VCM, 1.94% in CI, 9.51% in CIE. For $FRIDA$ database, the percentage improvement achieved by the technique with respect to DCP is 68.33% in r, 18.20% in FRF, 14.19% in VCM. The percentage improvement of the technique with respect to Kansal *et al's* technique is 32.91% in r, 11.81% in FRF, 9.14% in VCM. The technique improves the DCP and Kansal *et al's* technique, but it produces little over enhancement in case of road

images during the post processing step which causes the performance to be degraded in case of these images. The maximum percentage improvement achieved by the technique with respect to existing techniques is 113.38% in r, 12.60% CNI, 211.00% in FRF, 37.33% VCM, 6.69% CI, 0.89% in CIE. The minimum percentage improvement achieved by the technique with respect to existing techniques is 5.19% in r, 4.13% in CNI, 7.25% in FRF, 6.01% VCM, 2.79% CI, 0.89% in CIE. This Chapter validates the effectiveness and robustness of the image de-fogging technique which is capable of recovering foggy images with improved visual quality in color and details, while reducing the cost of computation. The technique removes halos artifacts by fusing two coarse transmission maps with different patch sizes. However, use of several scales of $DTCWT$ might be possible for further improvement.

.

Chapter 6

Extension of Minimum Preserving Subsampling based Image De-fogging Technique to Videos

6.1 Introduction

The image de-fogging techniques can be applied for video de-fogging but they involve some extra steps due to temporal nature of video data. In this Chapter, a video de-fogging technique is proposed by extending0 minimum preserving subsampling based image de-fogging technique [56]. Since, video processes large number of frames per second, there is a higher probability that number of adjacent frames are similar and highly correlated. In the videos, degradation due to fog is spatial variant, it is a challenge to recover the color and details of scene. General contrast enhancement techniques, such as histogram equalization and gamma correction, may not generate satisfying results. Therefore, many methods, such as using multiple images or additional information, have been proposed. The advantage of single image de-fogging is that it needs minimal input and may be valid for most scenes. Extending image de-fogging technique to video is not a trivial work. The challenges mainly come from the following aspects: [†].

(i) **Computational efficiency**: The technique must be able to efficiently process the large number of pixels in a video sequence. Hence, to deal with the enormous growing amount of digitalized video, it is important to have not only accurate but also computationally efficient video de-fogging techniques.

(ii) **Temporal coherence:** It has been proven that human visualization system (HVS) is very sensitive to temporal inconsistencies presented in video sequences. However, applying image de-fogging technique

[†]**Contents of the work presented in this Chapter have been published in *Journal of Modern Optics*, 65(18), pp. 2103-2123, 2018. (SCI Indexed)**

naively on frame by frame often results in visual flicker. Such an approach does not maintain homogeneities between neighboring frames and thus make video look inconsistent.

(iii) **Spatial consistency:** The de-fogged video should look as natural as the original one. Apart from temporal inconsistencies, it is also important to handle the discontinuities occur inside the video frame. The parameters of de-fogging for a given frame should be according to the current frame information. Therefore, to maintain the computational efficiency and temporal coherence, the spatial consistency should not be compromised.

Figure 6.1: Spatial inconsistency. (a) Input Foggy Image (b) De-fogged image obtained by Tarel *et al.* [114]

In this Chapter, a technique for restoring visibility from foggy videos is proposed, which can remove fog from videos and preserve the temporal and spatial coherence. An efficient single image de-fogging technique to perform per frame processing to the foggy video is employed, which outputs a sequence of transmission map of the original video. The minimum preserving subsampling based image de-fogging technique [56] has been extended to video de-fogging in this work. When there is a change in a scene of the video, flickering may occur. However, in the same scene, a gentle changeover must look between the neighboring frames. But, if the proposed technique for images is used frame by frame for video de-fogging, unexpected flickers must occur even in the same scene. From (1.11), it can be seen that I, t and L_A can be the factors creating this problem. As the original foggy video is generally smooth and has no flickers, therefore these unexpected flickers in the de-fogged videos are not happened due to the video itself. Also, each pixel in the frame is independently estimated in our technique, therefore it will not be influenced from its neighboring pixels. This shows that image I itself is a stable factor. Therefore, the flickering artifacts are generally caused due to changing atmospheric light L_A and transmission t among different frames. Instead of processing video frame by frame, in this work, a scene change detection algorithm based upon histogram correlation between the video frames is used and modified. The detailed process has been explained in the upcoming sections.

6.2 Background

Video is made of frames and each frame can be treated as single image. In a video, a time component is involved along with spatial data. Therefore, a technique might develop a model of human movement which would help increase accuracy with video sequences. Depending on frame rate and object velocity, deformation or blurring of the object in the video frame may be an issue or not.

6.2.1 General Video Structure

A general video structure is based upon a hierarchical framework, which includes multiple scenes. Each scene may consist of number of frames. The video de-fogging approach is based on the premise that the most representative frame for the whole scene should be one of the representative frames for its scenes and is selected from the representative frames. The relationship of video, scene and frame is shown in Figure 6.2 and is given by:

$$Video = \{Scene_i \mid 0 \leq i \leq N_{scenes}\}, \tag{6.1}$$

$$Scene_{ij} = \{Shot_i \mid 0 \leq i \leq N_{shot_i}\}, \tag{6.2}$$

$$Shot_i = \{Frame_k \mid 0 \leq k \leq N_{frames}\} \tag{6.3}$$

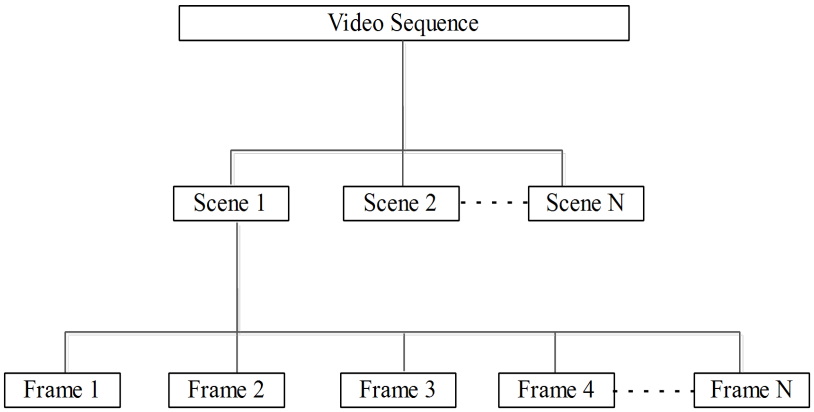

Figure 6.2: General Video Structure

- **Scene:** A scene is a logical grouping of shots into a semantic unit.
- **Shot:** A shot is a sequence of frames captured by a single camera in a single continuous action. A shot boundary is the transition between two shots.
- **Frame:** A digital video consists of frames that are a single frame consists of pixels.

Here N_{scene} is the number of scenes in a video, N_{shot_i} is the number of shots in $Scene_i$, N_{frames} is the number of frames in a given shot.

6.2.2 Video Scene Change Detection

Scene Change Detection (SCD) is a process to segment video sequences into scenes for creating indexed video databases. Scene change detection plays an indispensable role in segmenting a long video sequence into smaller units for further processing. A video shot is a sequence of successive frames with similar visual content in the same physical location. Therefore, an abrupt scene change can be identified when there is a large amount of visual content change across two successive frames while gradual transition is much difficult to detect because the successive frame difference during transition is substantially reduced. In Figure 6.3, the scene change is shown after different frames of a video. In this Figure, 10 frames of a foggy video are shown. Estimating transmission map and the atmospheric light for each frame individually during video de-fogging is computationally very expensive. It may also generate some unexpected flickers as described above. Therefore, it is always better to use information from the previous frames and use it again for processing upcoming frames. It improves computational performance and also removes unwanted flickers. To use the information from the previous frames, the relation between current and the previous frame is required. The relation can be estimated using a scene change detection algorithm. Many scene change detection techniques have been proposed [95]. In this work, Histogram Correlation based Scene Change Detection has been used proposed by Radwan *et al.* [96]. Correlation describes the degree of relationship between two variables. Frames in the video may consist of gradual transitions, motions and abrupt transitions. In the case of gradual transition, two adjacent frames slightly differ in their intensity values, but they have similar texture and the edges. So they have very strong correlation in the spatial domain. If there is a slight motion transition, the adjacent frames slightly differ in their intensity values and also the edges. The spatial correlation between the adjacent frames depends upon the speed of motion. In the abrupt transition, there may be a complete scene change between the adjacent frames and they are highly uncorrelated. The histogram H_i for i^{th} frame is calculated as:

$$H_i(r_j) = n_j \tag{6.4}$$

r_j is the j^{th} intensity level and

n_j is the number of pixels in the frame i having intensity value r_j.

The coefficient of correlation ($coeffcorr$) between H_i and H_{i-1} can be calculated as:

$$coefcorr(H_i, H_{i-1}) = \frac{\sum_{m=1}^{n}(H_i(m) - h_i)(H_{i-1}(m) - h_{i-1})}{\sum_{m=1}^{n}(H_i(m) - h_i)^2 \sum_{m=1}^{n}(H_{i-1}(m) - h_{i-1})^2} \tag{6.5}$$

n is the number of gray level r_j,

h_i, h_{i-1} are the average values of H_i, H_{i-1} respectively.

Radwan *et al.* plotted graphs by finding a correlation between all the pairs of adjacent frames to show various types of transitions. However in our work, some sort of threshold is required as, in real time, it is not possible that all the frames are initially available. Also, there may not be any threshold, which can certainly define the

(a) (b)

Figure 6.3: Video Scene Change in "Hazeroad.avi" video- 10 input video frames. (Frame 245, 250, 255, 260, 265, 270, 275, 280, 285, 290. (From left-right, top-bottom.))

correlation type between the neighboring frames. Therefore, in this work, instead of calculating any threshold, we have compared the two adjacent correlation coefficients *i.e.* $coefcorr_{i,k}$ *and* $coefcorr_{i-1,k}$ for scene change detection. The logic behind comparing two correlation coefficients is that, when frames $i-1$ and k are highly correlated, and frames i and k are also highly correlated, then there is a high probability that the difference between coefficient of correlations $coefcorr_{i,k}$ and $coefcorr_{i-1,k}$ is very less. The comparison between correlations for

scene change has been explained in next section.

6.2.3 Video De-fogging

The aim of video enhancement is to improve the visual appearance of a video, or to provide a better transform representation for future automated video processing such as analysis, detection, segmentation, recognition, surveillance, traffic and criminal justice systems. Carrying out video enhancement understanding under low quality video is a challenging problem due to low contrast and quality. With the same image processing, a lot of video enhancement techniques have been proposed. However, in all of these techniques, there still are no general standards, which could be used as a design criterion of video enhancement techniques.

6.3 Proposed Video De-fogging Technique

The minimum preserving subsampling based image de-fogging technique provides good results on almost all kind of foggy images. However, when applied to each frame of a foggy video independently, it may break the temporal coherence and yields a restored video with severe flicking artifacts. However, its low computational complexity makes it suitable to work with real-time applications. But for videos with higher frame rate, the time complexity needs to be reduced more. In this section, a fast and efficient video de-fogging technique has been proposed which is an extension of single image de-fogging technique of Kansal *et al.* [56].

6.3.1 Frame Extraction From a Video

Generally, video is a massive volume object with high redundancy and insensitive information. It has complex structure consisting of scene, shot, frame. Temporally adjacent frames in a video sequence contain slightly different, but unique, information. Therefore, video processing is a challenging task which generally involves the following steps:

i Reading the video

ii Processing the video

iii Writing the video

Video frame extraction is an important part of the large data processing. The tool used for video frame extraction or reading the video in this thesis is $MATLAB$. $MATLAB$ provides different algorithms that let us view, analyze, read, and write videos. For obtaining video frames, $VideoReader$ method is used which returns an object. This object contains information about the video file and enables us to read data from the video. After obtaining the video frames, de-fogging is applied on frames. In the end, $VideoWriter$ function is used to obtain the processed videos by using the processed frames.

6.3.2 Frame Atmospheric Light Estimation

According to physical model (1.11), the scene point value of a foggy image approaches to global atmospheric light in regions of infinite depth. Such regions generally lie at the top of the image. Therefore, in this work, to save the computational time, approximately 25% top image rows are extracted and their corresponding dark channel is estimated by upsampling (3.3). According to He *et al.* [33], bright pixels in the dark channel represent most fog opaque region, but it may contain some bright light objects which may cause the value of global atmospheric light to become too dark or bright. Such objects are filtered by applying 3-σ rule on YUV color space corresponding to RGB image I. Y in YUV color space represents luminance information whereas U and V represents the respective color information. According to Kansal *et al.* [55], for illuminated regions, any of the Y, U and V channels or all of them together have very high values. With the help of this fact, such regions can be filtered prior to atmospheric light estimation. After identifying the brighter pixels from the selected foggy image portion, their corresponding dark channel values are set equal to zero, so that they must not be selected as the candidates of atmospheric light. Finally, the values in R, G, B color channels corresponding to top 0.1% brightest pixels in dark channel are selected as global atmospheric light L_A.

6.3.3 Frame Transmission Map Estimation and Refinement

In this de-fogging technique, depth map is estimated by using dark channel. Initial transmission map (t) is obtained by reversing depth map and then the refined transmission map (t') is obtained by applying fast guided filter on t. Following are the procedural steps for estimating fast dark channel:

- Normalized foggy Image ($\frac{I^c}{L_A^c}$) having size $M \times N \times 3$, is divided into non overlapping s_b blocks (B_1, B_2.., B_i.....B_{s_b}) of size $5 \times 5 \times 3$ each.

- Then, a down sampled depth image d_{ds} is created in such a way that each pixel in d_{ds} is obtained from each block B_i by taking the minimum in the respective block as

$$d_{ds}(x) = min(B_i(x)), \quad i = 1, 2, 3, ...s\_b \tag{6.6}$$

  The number of pixels in d_{ds} is equal to s_b. Here min specifies the mathematical operation to find the minimum depth value in a block B_i.

- After obtaining d_{ds}, its window based dark image d_{ds}^{dark} is estimated as

$$d_{ds}^{dark}(x) = min_{y \in \Omega(x)}(d_{ds}(y)) \tag{6.7}$$

  Here Ω is the window of size 3×3.

- After this, nearest neighbor up sampling of d_{ds}^{dark} is performed to obtain the equivalent window based depth map I^{dark}. Now, this depth map will be further refined as described in the next section for depth map estimation.

After estimating the dark channel map I^{dark}, initial transmission map is estimated by using (1.31). Since the dark channel is a patch wise constant value which produces blocking artifacts around the edges [33], [109] *etc*. In this work, guided filter is used for transmission refinement which performs smoothening in almost $O(N)$ time. This filter can shift the structure of input foggy image I to filtering transmission map t. The guided filter effectively suppresses gradient reversal artifacts [34] and produces visually appealing edge profiles. In this work, fast implementation of guided filter [35] is chosen which improves the speed of guided filter by performing the operations on down sampled input images with scaling parameter s. With fast guided filter, the transmission map t, and the guidance input image I_g are subsampled (nearest-neighbor or bilinear) with scaling factor s. All the window based filters are performed on the subsampled maps. The two coefficient maps $\bar{a}$ and $\bar{b}$ are upsampled (bilinear) to the original size. Finally, the filtered transmission map t' is computed using (3.7) with upsampled coefficients and the guidance image.

6.3.4 Recovering Frame Scene Radiance and Post Processing

After obtaining the global atmospheric light L_A and the refined transmission map t', the de-fogged image L_0 is recovered by using (1.32) from the foggy image I. In addition to this, since the foggy image is affected by environment lightening, some parts of the de-fogged image may suffer from low brightness and due to DCP based image restoration, de-fogged images will be even more darker. Therefore, in this work, a combined color channel transmission map is used to identify under exposed regions and an adaptive technique is used to enhance such regions. Since, the low and high intensity values of each color channel represent darker and brighter regions respectively of an image [46] for that color channel. To identify the overall darker regions in a colorful frame, the combined color channel darkness effect C^d is estimated by using

$$C^d(x) = (1 - \frac{L_0^R(x)}{max(L_0^R)}) \times (1 - \frac{L_0^G(x)}{max(L_0^G)}) \times (1 - \frac{L_0^B(x)}{max(L_0^B)}) \tag{6.8}$$

Here L_0 is the de-fogged frame, max is the mathematical operator to find the maximum value in each color channel RGB. Now, C^d is normalized in the range $[0, 1]$ to obtain normalized combined color channel darkness effect as:

$$C_n^d(x) = \frac{C^d(x) - min(C^d)}{max(C^d) - min(C^d)} \tag{6.9}$$

The value of C_n^d is highest in the darkest region, which helps to enhance those regions more. Finally the processed de-fogged frame L_0' is obtained by using

$$L_0'(x) = L_0(x) \times exp^{(C_n^d(x) \times v)} \tag{6.10}$$

Here v is the scaling factor to adjust the image brightness. By experimenting with number of images/frames, it has been found that the post processing results are better for values of v near 0.5. Therefore, to show the results, we have chosen the value $v = 0.5$. However the frames can be made more bright by increasing v. exp is the exponential operator which abruptly increases C_n^d values of darker regions while keeping the brighter region's low. The effect of post processing has been shown in Chapter 3 in Figure 3.11. Figure 3.11(a) shows the input image, Figure 3.11(b) shows the restoration without post processing. Under enhanced region is shown in yellow box. Figure 3.11(c) shows the restoration with post processing and the improved region is shown in yellow box.

6.3.5 Video De-fogging Approach

As described above, estimating transmission map and the atmospheric light for each frame individually during video de-fogging is computationally very expensive. It may also generate some unexpected flickers as described above. Therefore, it is always better to use information from the previous frames and use it again for processing upcoming frames. It improves computational performance and also removes unwanted flickers. Therefore, the parameters L_A and t and not required to be calculated for each video frame. In this technique, a background frame (reference frame) is selected to estimate de-fogging parameters which represents number of upcoming frames. A histogram based scene change detection is applied to check whether there is a need to update the background frame (k). In this approach, initially, the first frame is selected as the background frame. All the parameters, ***i.e.***, L_A, t and t' are estimated using this frame and the de-fogged frame is obtained. Second frame is selected as i^{th} frame. The histogram based coefficient of correlation $coefcorr$ is estimated between the $(i-1)^{th}$, k^{th} frames ($coefcorr_{i,k}$) and i^{th}, k^{th} frames ($coefcorr_{(i-1),k}$). To decide whether there is a need to re-estimate frame de-fogging parameters, a threshold is required. But in this work, rather than taking a threshold, each $coefcorr$ is rounded off to three decimal places. Then, the three decimal places of $coefcorr_{(i-1),k}$ and $coefcorr_{i,k}$ are checked. When both the coefficients are different at first decimal place, it is considered that, current frame i and the background frame k are uncorrelated. In this case, L_A, t and t' are estimated using i^{th} frame and the same frame is now set as new background frame. If the coefficients are same at first decimal place, then the second decimal place is checked. If they are differencing at this place, it is considered that two frames are weakly correlated. In this case, L_A and t are taken from previous frames. The refined transmission map t' is calculated by applying guided filter on t with current frame taking as reference frame.

Finally, the difference in the third decimal place is considered insignificant. In this case all the parameters are taken from the previous frames and the current frame is restored using those. In this way, the flickering artifacts cant be reduced among the frames along with lowering the computational complexity.

6.3.6 Algorithm of the Video De-fogging

The procedural steps of the proposed video de-fogging are described in Algorithm 6.1:

Algorithm 6.1: Minimum Preserving Sampling based Video De-fogging Technique.

---

i Extract the first Video frame f_1 and estimate its histogram H_1. Set this frame as a background frame B_k. Initially, set $k = 1$ and estimate initial and refined transmissions *i.e.* t_k and t'_k using the background frame. Similarly estimate global atmospheric light from this frame *i.e.* L_{A_k}.

ii Repeat the following steps for $i = 2\ to\ N$:

ii.a Extract the i^{th} frame and estimate its histogram H_i. Find the coefficient of correlation $coefcorr_{i,k}$ between the histogram of current frame H_i and the background frame H_k, where $0 \leq coefcorr \leq 1$. Round off $coefcorr_{i,k}$ to three decimal places. If $coefcorr_{i,k} = 1$, set $coefcorr_{i,k} = 0.999$.

ii.b Now the de-fogging parameters t_i and L_{A_i} for current frame i are estimated according to the following:

ii.b.1. Compare the coefficient of correlation $coefcorr_{i,k}$ and $coefcorr_{i-1,k}$. If both the coefficients are not same at first decimal place, then estimate the initial, refined transmission map and the atmospheric light from the current frame i itself. Update the background frame as i^{th} frame as $B_k = f_k$ and set $k = i$. De-fogged frame f_{r_i} is then obtained by using (1.32). Apply post processing on the restored frame by using (6.10). Go back to Step (ii). If both the coefficients are same at first decimal place, then compare second decimal place according to next step.

ii.b.2. If they not same, the initial estimate of transmission is taken from the background frame and refined transmission map is calculated by applying guided filter on initial transmission map with current frame f_i as the reference frame. De-fogged frame f_{r_i} is then obtained by using (1.32). Apply post processing on the restored frame by using (6.10). Go to Step (ii). If both the coefficients are same at second decimal place also, then go to next step.

ii.b.3. In this case, transmission and atmospheric light need not to be calculated for the current frame. Directly using the previous parameters, de-fogged frame f_{r_i} is then obtained by using (1.32). Apply post processing on the restored frame by using (6.10).

6.4 Experimental Results and Analysis

The video de-fogging technique has been applied on three foggy videos including “cross”, “bali” and “riverside”. Visual results of the de-fogged videos are shown in Figures 6.4, 6.5 and 6.6 for minimum preserving subsampling based image de-fogging technique [56], Cai *et al's* [16] technique and the proposed video de-fogging technique.

The objective parameters for the videos of the given techniques have also been compared in the next subsections to prove the validity of quality of our video de-fogging technique in terms of temporal/spatial coherence and computational time.

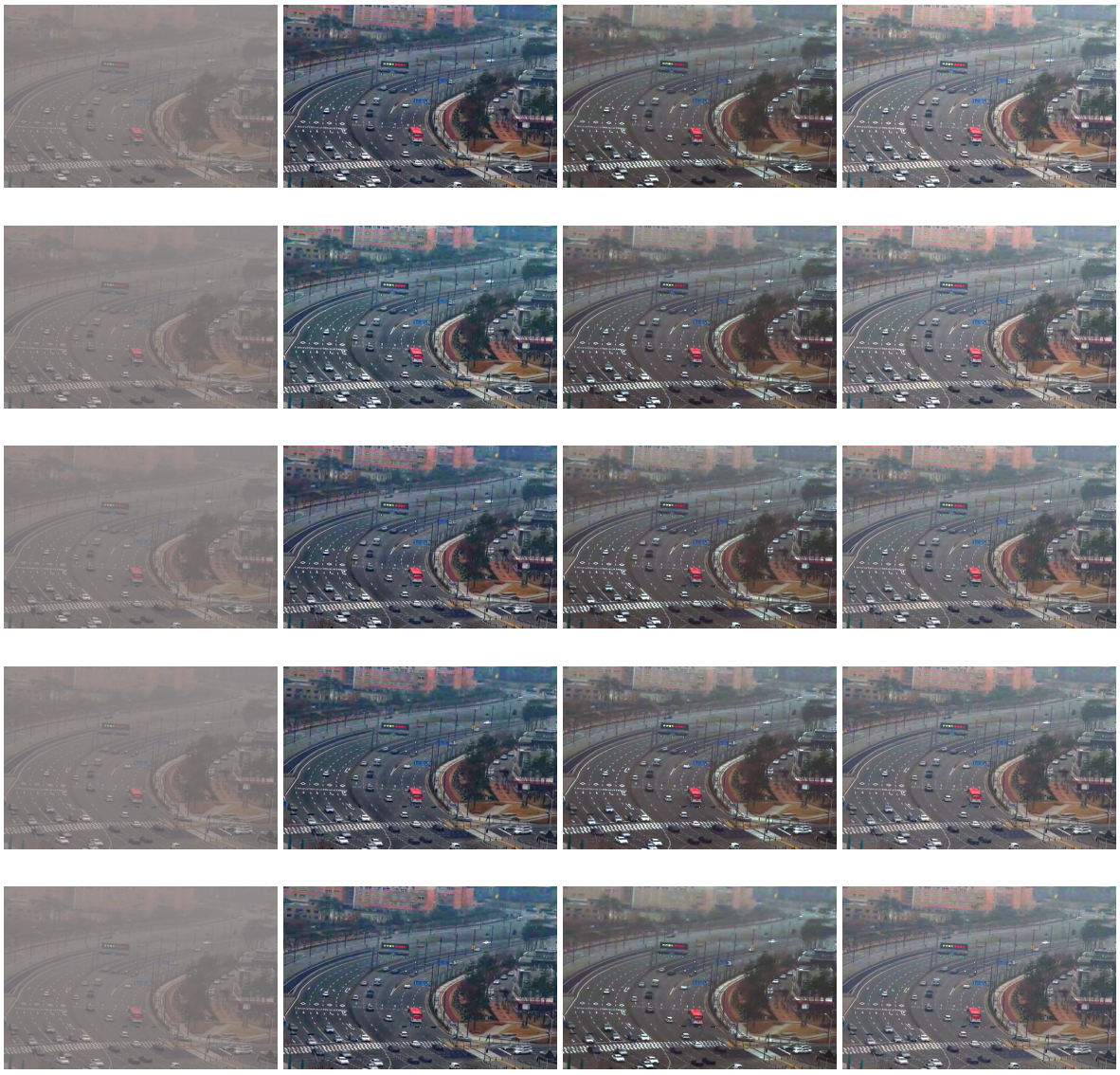

(a) (b) (c) (d)

Figure 6.4: Video De-fogging Results on "Cross.avi". (a) 5 consecutive input video frames. Corresponding video frames generated by (b) Minimum preserving sampling based image de-fogging technique (c) Cai *et al's* technique (d) Proposed Video De-fogging technique.

6.4.1 Temporal Coherence Analysis

Since human visualization system is very sensitive to temporal inconsistencies presented in video sequences, applying image de-fogging technique naively on frame by frame often results in visual flicker and does not maintain homogeneities between neighboring frames and thus make video looks inconsistent. Therefore to validate the proposed de-fogging technique in terms of temporal coherence, average Histogram Correlation Coefficient $coefficorr(H_i, H_{i-1})$ between two adjacent frames $i-1$ and i is estimated for the whole video frames and is

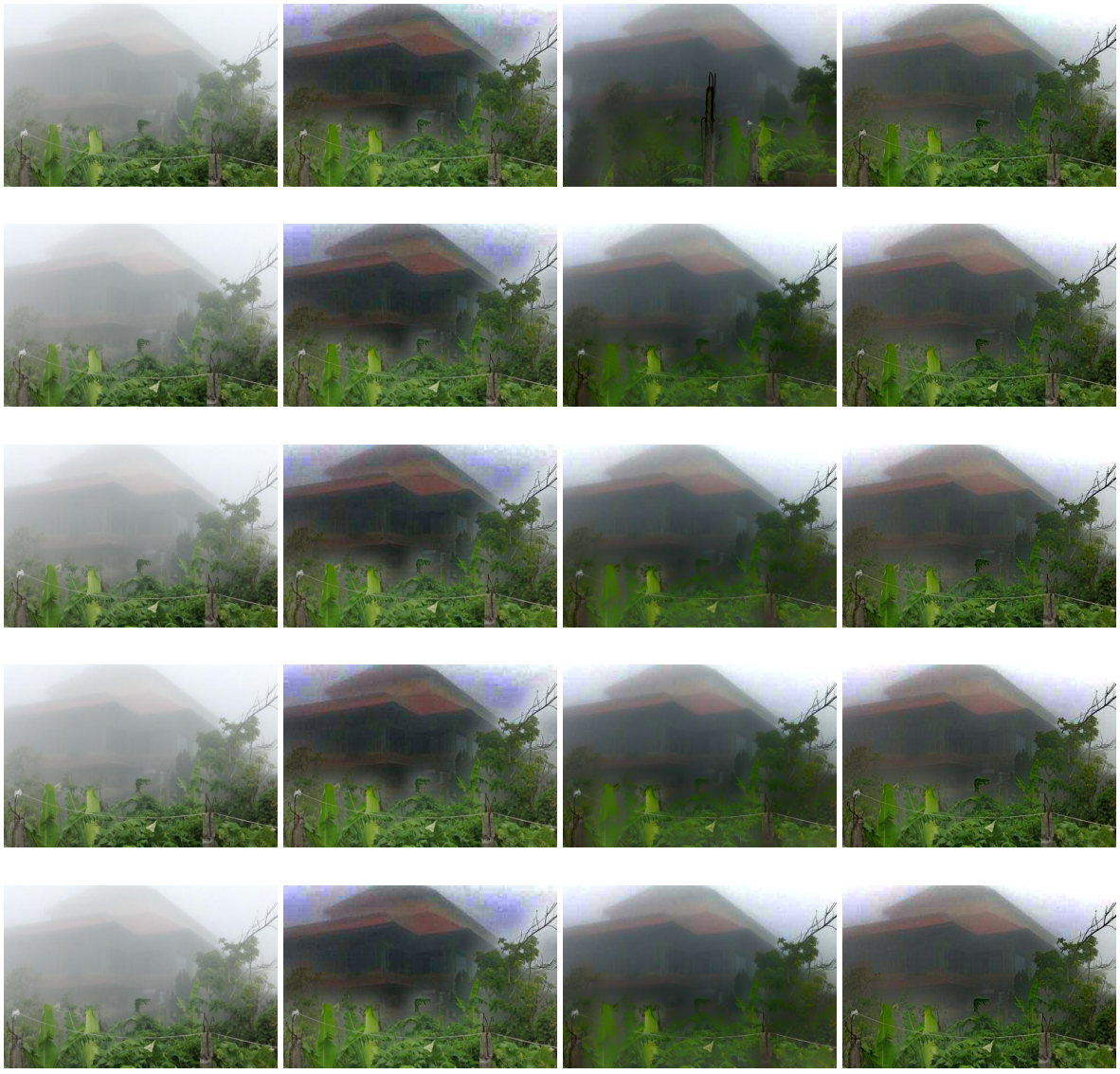

(a) (b) (c) (d)

Figure 6.5: Video De-fogging Results on "Bali.avi".Corresponding video frames generated by (b) Minimum preserving sampling based image de-fogging technique [56] (c) Cai *et al's* technique [16] (d) Proposed Video De-fogging technique.

shown in Table 6.1. It consists the data of three videos, "cross","bali" and "riverside" for the proposed video de-fogging technique, minimum preserving subsampling based image de-fogging technique and Cai *et al's* technique. It can be seen from Table 6.1 that average $coef corr$ of our de-fogging technique is slightly lesser than that of Cai *et al's* technique but it is better than that of naive minimum preserving subsampling based image de-fogging technique.

From Table 6.1, it can be concluded that the video de-fogging technique is better than naive image de-fogging technique by 0.72% in terms of temporal coherence. However, the performance of the de-fogging technique is 1.12% less in comparison to Cai *et al's* [16] technique.

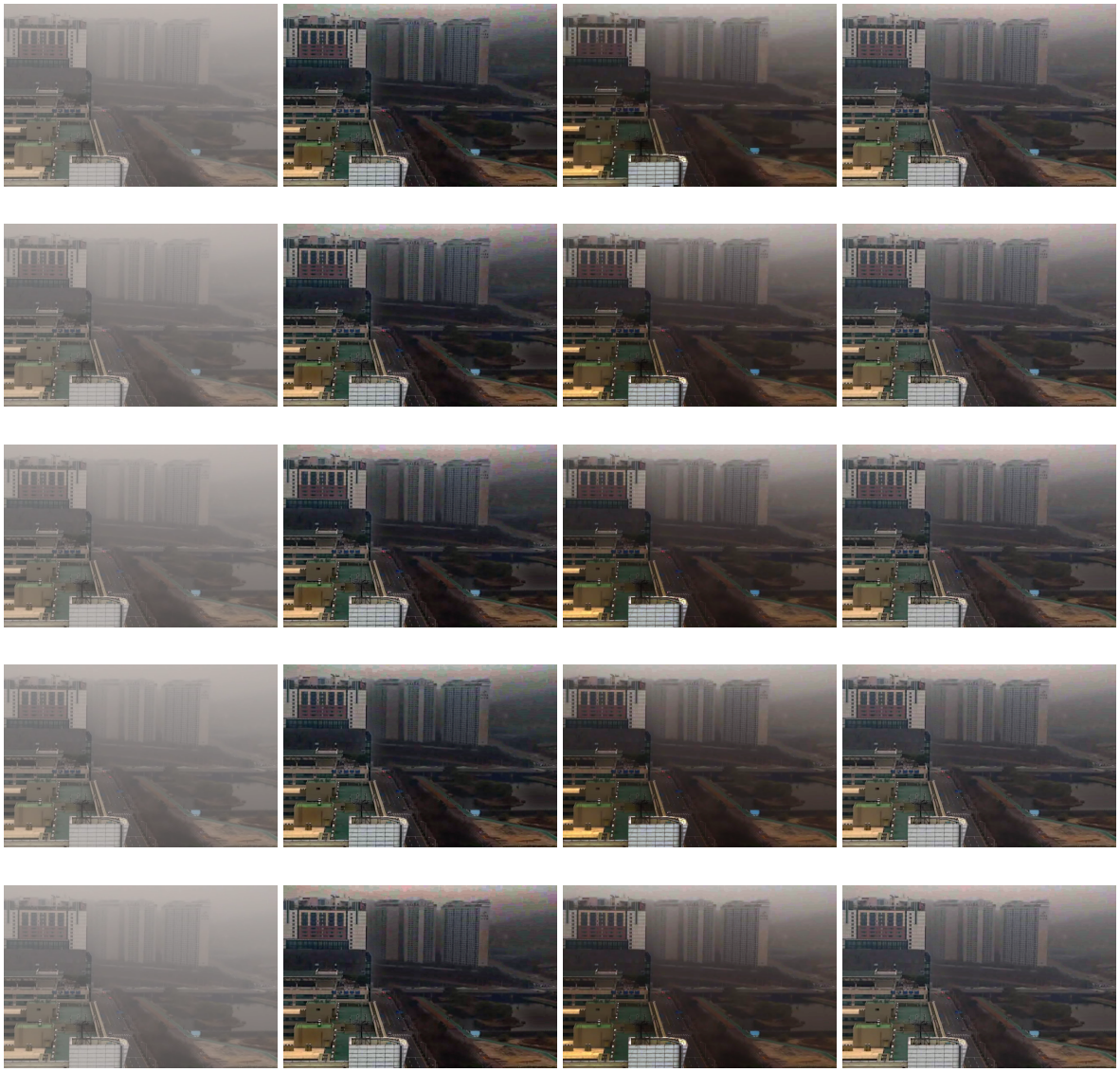

(a) (b) (c) (d)

Figure 6.6: Video De-fogging Results on "Riverside.avi". Corresponding video frames generated by (b) Minimum preserving sampling based image de-fogging technique (c) Cai *et al's* technique (d) Proposed Video De-fogging technique.

Table 6.1: Comparison of the proposed video de-fogging technique with the existing techniques on the basis of Histogram Correlation Coefficient.

	Original Video	Kansal *et al.* [56] (Image)	Cai *et al.* [16]	Proposed (Video)
Cross	0.995	0.969	0.985	0.970
Bali	0.972	0.961	0.959	0.944
Riverside	0.991	0.948	0.981	0.984
Average	**0.986**	**0.959**	**0.975**	**0.966**

6.4.2 Spatial Coherence Analysis

In this section, the Average evaluation parameters r, CNI, FRF, VCM, CI and CIE are estimated between the foggy and the de-fogged frames for the proposed technique, minimum preserving subsampling based image de-fogging technique and Cai *et al's* technique. The results are shown in Table 6.2. It can be seen that almost all the parameters of the proposed video de-fogging technique are better than that of minimum preserving subsampling based image de-fogging technique and Cai *et al's* technique. Although, in some videos, *e.g.* in Figure 6.4, results in column (b) appear better than that of our technique for "cross" video. But at the same time, it can be observed that in this case false bluish color appears in the recovered frames which makes them look unnatural. Moreover in some portions over darkness causes the fine details to become vague in column (b) images which can be even observed from evaluation parameters in Table 6.2. Therefore, it can be concluded that the video de-fogging technique maintains the spatial coherence along with maintaining the temporal coherence in the output de-fogged frames.

From Table 6.2, it can be concluded that the the percentage improvement achieved by proposed video de-fogging technique with respect to naive minimum preserving subsampling based image de-fogging technique is 4.03% in r, 1.96% in CNI, 5.07% in FRF, 4.89% in VCM, 2.54% in CI, 1.26% in CIE and with respect to Cai *et al's* technique [16] is 21.36% in r, 22.88% in FRF, 66.41% in VCM, 32.18% in CI, 4.46% in CIE. However, there is a decrease in CNI by 8.77% which is less in comparison to improvement in other parameters.

Table 6.2: Comparison of the proposed video de-fogging technique with the existing techniques on the basis of r, CNI, FRF, VCM, CI and CIE.

Kansal *et al.* [56]						
	r	CNI	FRF	VCM	CI	CIE
Bali	1.30	0.53	2.02	53.65	27.40	7.25
Cross	3.42	0.46	2.81	82.46	27.05	7.26
Riverside	2.04	0.56	2.70	32.81	16.29	7.09
Average	**2.73**	**0.51**	**2.76**	**57.64**	**21.67**	**7.17**
Cai *et al.* [16]						
Bali	0.65	0.52	1.74	30.25	22.25	7.39
Cross	3.13	0.51	2.33	48.23	16.14	6.80
Riverside	1.55	0.64	2.39	24.43	17.48	7.10
Average	**2.34**	**0.57**	**2.36**	**36.33**	**16.81**	**6.95**
Proposed Technique						
Bali	1.31	0.54	2.33	50.89	25.80	7.02
Cross	3.60	0.47	3.05	87.95	27.76	7.42
Riverside	2.07	0.57	2.74	32.97	16.68	7.11
Average	**2.84**	**0.52**	**2.90**	**60.46**	**22.22**	**7.26**

The results in this section justifies the spatial coherence achieved by the proposed de-fogging technique.

6.4.3 Computational Time Analysis

Apart from improving the quality, frame rate *i.e.*, the number of frames processed per second during de-fogging is another parameter to judge the performance of a video de-fogging process. In this section, frame rate of the proposed video de-fogging technique is compared with the existing image de-fogging technique based upon minimum preserving subsampling based de-fogging as this technique is extended to videos and also with Cai *et al's* technique and the results are shown in Table 6.3 (In this table, the results are shown with guided filter implementation provided in [36]). In the table, size of video frame is mentioned as $M \times N \times V$. Here $M \times N$ is the frame size and V is total number of frames in a video. As shown in Table 6.3, the proposed video de-fogging technique obtains higher frame rate in comparison to Cai *et al's* technique in case of "Cross" and "Riverside" videos whereas the frame rate is lesser for "Bali" video. Overall, the proposed technique outperforms the technique of Cai *et al.*.

Table 6.3: Comparison of Frame Rate of the proposed video de-fogging with frame by frame de-fogging (Guided Filter [36] implementation).

	Cross $480 \times 640 \times 657$	Bali $270 \times 480 \times 220$	Riverside $480 \times 640 \times 489$
Kansal *et al.* [56]	8.78 frames/sec	17.71 frames/sec	9.22 frames/sec
Cai *et al.* [16]	24.18 frames/sec	58.56 frames/sec	23.89 frames/sec
Proposed Technique	33.73 frames/sec	40.84 frames/sec	27.36 frames/sec

From Table 6.3, it can be observed that the percentage improvement achieved by the proposed video de-fogging technique with respect to naive minimum preserving subsampling based image de-fogging technique is 284.17% for "Cross", 130.60% for "Bali" and 196.74% for "Riverside" videos and the improvement with respect to Cai *et al's* technique is 39.49% for "Cross" and 14.52% for "Riverside" videos respectively. However, there is decrease by 30.26% for "Bali" video, but overall the performance of the proposed video de-fogging technique is better in comparison to others.

6.5 Conclusion of the Chapter

In this Chapter, minimum preserving subsampling based image de-fogging technique is extended to videos which improves the visual performance in terms of spatial/temporal coherence, and also reduces the execution time. First video frame is extracted and considered as a reference frame. Parameters of physical model are calculated using reference frame and for further frames, the histogram based correlation is checked between upcoming and the reference frames. If they are correlated, the previous parameters are used to de-fog the upcoming frames, otherwise, parameters are estimated for the upcoming frame 0and then the reference frame is updated. This maintains the spatial/temporal coherence in the videos and also improves the computational complexity. The percentage improvement achieved by the video de-fogging technique with respect to minimum preserving subsampling based image de-fogging technique is 4.03% in r, 1.96% in CNI, 5.07% in FRF, 4.89% in VCM, 2.54% in CI, 1.26% in CIE and with respect to Cai *et al's* technique is 21.36% in r, 22.88% in FRF, 66.41% in VCM, 32.18% in CI, 4.46% in CIE. The percentage improvement achieved by the video de-fogging technique with respect to naive minimum preserving subsampling based image de-fogging technique is 284.17% for "Cross", 130.60% for "Bali" and 196.74% for "Riverside" videos and the improvement with respect to Cai *et al's* technique is 39.49% for "Cross" and 14.52% for "Riverside" videos respectively. The overall results justifies the spatial/temporal coherence and computational speedup achieved by the de-fogging technique. 00

Chapter 7

Conclusions and Future Scope

7.1 Conclusions

To solve the issues like de-fogging in case of images containing one or more light sources other than the natural light present in the atmosphere in the existing de-fogging techniques, computational complexity of de-fogging techniques *etc.*, in this thesis, efficient techniques for image/video de-fogging have been developed on the basis of DCP and CAP based theories. Based upn DCP, a novel image subsampling approach to preserve local minima in a patch of an input image is proposed. The subsampled image is further used for dark channel estimation. Using this mechanism, the dark channel of a given image is found approximately 15 times faster than that of normal dark channel without causing any visible degradation in visual quality of the de-fogged images. To further accelerate the de-fogging process, atmospheric light has been found from upper region of the foggy image after filtering out bright light sources or regions. The experimental results show that proposed technique performs well for various image types by adaptively estimating atmospheric light. It is shown that the de-fogging technique is capable of performing the task in a real-time fashion on modern standard computer hardware. The maximum percentage improvement achieved by proposed technique with respect to compared existing techniques is 74.79% in r, 14.51% CNI, 76.69% in FRF, 16.70% VCM, 88.51% CI, 6.05% in CIE and the minimum percentage improvement is 28.39% in r, 4.41% CNI, 0.55% in FRF, 5.13% VCM, 28.16% CI, 0.82% in CIE. For $FRIDA$ database, the maximum percentage improvement achieved by proposed technique with respect to existing techniques is 60.81% in r, 14.29% CNI, 177.42% in FRF, 25.96% VCM, 7.09% CI, 2.26% in CIE and the minimum percentage improvement is 1.28% in r, 5.66% CNI, 2.69% in FRF, 4.75% in VCM, 3.19% in CI, 0.17% in CIE.

Since machine learning applications have been gaining lot of attention in recent years with their increasing demand, growing usage and a scope of improvement. Such techniques can lead to produce better de-fogging results in the future. Therefore, the next de-fogging technique is based upon CAP theory. CAP uses a linear model for estimating the scene depth of a foggy image and learns the parameters of model with a supervised

learning method to obtain the depth map of a foggy image. Using CAP, depth from a foggy image at each pixel is estimated based on difference between saturation and brightness for the respective pixel. Local window based minimum operation is applied to optimize the estimation time of the depth map. Depth map is further refined using gradient domain guided image filter which recovers fine edge details. For avoiding the problem caused due to error in estimation of global atmospheric light and a constant value of β, we present a novel strategy to post process the de-fogged image. It causes simultaneous dynamic range modification, color consistency, and lightness rendition without having the artifacts in a time efficient manner. The maximum percentage improvement achieved by proposed technique with respect to other compared techniques for standard foggy images is 80.67% in r, 22.58% in CNI, 73.10% in FRF, 13.22% in VCM, 37.07% in CI, 7.20% in CIE, whereas the minimum percentage improvement is 1.89% in r, 1.33% in CNI, 11.95% in FRF, 1.98% in VCM, 3.30% in CI, 1.09% in CIE. For $FRIDA$ database, the maximum percentage improvement achieved by proposed technique with respect to existing techniques is 242.84% in r, 70.32% CNI, 334.47% in FRF, 59.91% VCM, 203.36% CI, 9.90% in CIE and the minimum percentage improvement is 69.00% in r, 3.70% in CNI, 13.29% in FRF, 23.43% VCM, 25.09% CI, 3.35% in CIE. Experimental results show that the proposed technique achieves high efficiency and better de-fogging effect. It can be also be applied to real time applications due to its low computational cost.

The next technique is based upon fusion based foggy image restoration by using DCP and $DTCWT$. However the proposed minimum preserving subsampling based image de-fogging technique significantly reduces the cost of dark channel estimation, but due to taking constant dark channel patch size, the de-fogging results may suffer from color and edge distortion problems. Color distortion generally occurs due to a smaller patch size while an edge distortion happens due to a larger patch. To solve these problems, transmission map is further improved by fusing wavelet sub-bands of dark channels with two different patch sizes. The wavelet chosen is $DTCWT$ which ensures the perfect reconstruction of image details in the transmission map due to its shift invariance property. $DTCWT$ is also rich in directional selectivity of an input signal and hence obtains high quality edges in the de-fogging results. The processing time is reduced by estimating the dark channel with minimum preserving downsampling approach. In addition to this, de-fogging results are further enhanced by using an adaptive post processing technique. The maximum percentage improvement achieved by proposed technique with respect to other compared techniques for standard foggy images is 80.67% in r, 17.74% in CNI, 131.07% in FRF, 41.38% in VCM, 39.72% in CI, 7.06% in CIE and the minimum percentage improvement is 24.33% in r, 2.81% in CNI, 12.76% in FRF, 13.10% in VCM, 1.94% in CI, 9.51% in CIE. For $FRIDA$ database, the maximum percentage improvement achieved by proposed technique with respect to existing techniques is 113.38% in r, 12.60% CNI, 211.00% in FRF, 37.33% VCM, 6.69% CI, 0.89% in CIE and the minimum percentage is 5.19% in r, 4.13% in CNI, 7.25% in FRF, 6.01% VCM, 2.79% CI, 0.89% in CIE. For the sake of application orientation, many sets of parameters have been tested which are best usable for de-fogging based applications.

Existing de-fogging techniques produce impressive and realistic image de-fogging results but their major lim-

itation is high computational cost. Finally in this thesis, the minimum preserving sub-sampling based image de-fogging technique is extended to videos as this is proved to be competent for improving all considered image types and also in terms of time complexity. A scene change detection algorithm is used to simultaneously manage the temporal coherence and computational cost in the proposed video de-fogging technique as demonstrated in experiments. Therefore, the proposed de-fogging technique can process large number of frames in real time by using faster processing tool and higher system configuration. The percentage improvement achieved by the proposed video de-fogging technique with respect to naive minimum preserving subsampling based image de-fogging technique is 284.17% for "Cross", 130.60% for "Bali" and 196.74% for "Riverside" videos and the improvement with respect to Cai *et al's* technique is 39.49% for "Cross" and 14.52% for "Riverside" videos respectively. The overall results justifies the spatial/temporal coherence and computational speedup achieved by the proposed de-fogging technique.

The main innovations of our de-fogging techniques include calculating a transmission map, estimating the atmospheric light and to recover a high quality de-fogged image by using a single foggy image. The results of various foggy images demonstrate that our techniques can significantly improve the visual effect, recover vivid colors, gain contrast and increase the scene visibility of a foggy image. There is no additional optimization required when using the estimated transmission map, thus reducing the computational time. Compared with previous de-fogging techniques, the processing speed of the proposed techniques is much faster. Proven by experimental verification, this thesis forms a promising framework in achieving the proposed objectives of image and video de-fogging.

7.2 Future Scope

This work has proposed four de-fogging techniques applicable to digital images and videos but there is still a scope of further improvements in the implementation of proposed techniques. This section discusses some of the possible directions that can improve de-fogging techniques.

- More efficient optimization approaches can be applied to improve the transmission and atmospheric lights used in the de-fogging model.
- Proposed fusion based image de-fogging technique can be improved by using advanced transforms as well as patches of different window size.
- Proposed de-fogging techniques need to be extended for non-homogeneous environments. In order to do this, more sophisticated atmospheric scattering physical model is required.
- Patterns between image pixel values and transmittance can be explored in order to further improve the de-fogging performance.
- Proposed techniques can be extended to higher bands images like multi-spectral, hyper-spectral images *etc.* by using their different characteristics.

- There is also a need to obtain more parameters for benchmarking the results obtained by the de-fogging techniques.

The above research directions might help to strengthen the efficiency and robustness of the proposed background modeling and the de-fogging techniques though some of the suggestions require computational intensive processes which may not be able to perform in real-time.

References

[1] Aggarwal R. K., "Study of single image fog removal techniques in low visibility foggy images", in Proceedings of IEEE International Conference on Computing, Communication and Automation, pp. 1114-1118, Greater Noida, India, May 2017.

[2] Alwani M. and Tiwari A. K., "A constrast enhancement based algorithm to improve visibility of colored foggy images", in Proceedings of 4^{th} WSEAS International Converence on Business Administration, pp. 26-30, 2010.

[3] Ancuti C. O., Ancuti C., Hermans C. and Bekaert P., "A fast semi-inverse approach to detect and remove the haze from a single image", in Proceedings of Asian Conference on Computer Vision, Springer, pp. 501-514, Berlin, Heidelberg, November 2010.

[4] Ancuti C. O., Ancuti C. and Bekaert P., "Effective single image dehazing by fusion", in Proceedings of 17^{th} IEEE International Conference on Image Processing, pp. 3541-3544, Hong Kong, China, September 2010.

[5] Ancuti C., Ancuti C. O., Haber T. and Bekaert P., "Enhancing underwater images and videos by fusion", in Proceedings of IEEE Conference on Computer Vision and Pattern Recognition, pp. 81-88, Providence, RI, USA, June 2012.

[6] Ancuti C. O. and Ancuti C., "Single image dehazing by multi-scale fusion", IEEE Transactions on Image Processing, Vol. 22, No. 8, pp. 3271-3282, 2013.

[7] Antani S., Kasturi R. and Jain R., "A survey on the use of pattern recognition methods for abstraction, indexing and retrieval of images and video", Journal of Pattern recognition, Vol. 35, No. 4, pp. 945-965, 2002.

[8] Anwar M. I., Khosla A. and Singh G., " Visibility enhancement with single image fog removal scheme using a post-processing technique", in Proceedings of 4^{th} IEEE International Conference on Signal Processing and Integrated Network, pp. 280-285, Noida, India, February 2017.

[9] Anwar M. I. and Khosla A., "Vision enhancement through single image fog removal", Journal of Engineering Science and Technology, Vol. 20, No. 3, pp. 1075-1083, 2017.

[10] Archa S. and Abdul A., "A novel method for video dehazing by multi-scale fusion", International Journal Scientific Engineering and Technology Research, Vol. 3, pp. 4808-4813, 2014.

[11] Arya S, Pratap N and Bhatia K., "Future of face recognition: A review", Journal of Procedia Computer Science, Vol. 58, pp. 578-585, 2015.

[12] Baskaran J and Subban R., "Compressive object tracking-A review and analysis", in Proceedings of IEEE International Conference on Computational Intelligence and Computing Research, pp. 1-7, December 2014.

[13] Bedagkar-Gala A. and Shah S. K., "A survey of approaches and trends in person re-identification", Journal of Image and Vision Computing, Vol. 32, No. 4, pp. 270-286, 2014.

[14] Bhatnagar G., Wu J. and Raman B., "Fractional dual tree complex wavelet transform and its application to biometric security during communication and transmission", Journal of Future Generation Computer Systems, Vol. 28, No. 1, pp. 254-267, 2012.

[15] Busch C. and Debes E., "Wavelet transform for analyzing fog visibility", Journal of IEEE Intelligent Systems and their Applications, Vol. 13, No. 6, pp. 66-71, 1998.

[16] Cai B., Xu X. and Tao D., "Real-time video dehazing based on spatio-temporal mrf", in Proceedings of Pacific Rim Conference on Multimedia, pp. 315-325, Springer, Cham, September 2016.

[17] Cai B., Xu X. Jia, K., Qing C. and Tao, D., "Dehazenet: An end-to-end system for single image haze removal", IEEE Transactions on Image Processing, Vol. 25, No. 11, pp. 5187-5198, 2016.

[18] Choi L. K., You J. and Bovik A. C., "Referenceless prediction of perceptual fog density and perceptual image defogging", IEEE Transactions on Image Processing, Vol. 24, No. 11, pp. 3888-3901, 2015.

[19] Choi L. K., You J. and Bovik A. C., "$http://live.ece.utexas.edu/research/fog/fade_defade.html$",, accessed February 2, 2018.

[20] Codes M. O., "International Codes-WMO No. 306", Geneva - Switzerland: World Meteorological, 1995.

[21] Dippel S., Stahl M., Wiemker R. and Blaffert T., "Multiscale contrast enhancement for radiographies: Laplacian pyramid versus fast wavelet transform", IEEE Transactions on Medical Imaging, Vol. 21, No. 4, pp.343-353, 2002.

[22] Fang S., Zhan J., Cao Y. and Rao R., "Improved single image dehazing using segmentation", in Proceedings of 17^{th} IEEE International Conference on Image Processing, pp. 3589-3592, Hong Kong, China, September 2010.

[23] Fattal R., "Single image dehazing", ACM Transactions on Graphics, Vol. 27, No. 3, pp. 1-9, 2008.

[24] Feng C., Zhuo S., Zhang X., Shen L. and Susstrunk S., "Near-infrared guided color image dehazing", in Proceedings of 20^{th} IEEE International Conference on Image Processing, No. EPFL-CONF-188639, pp. 2363-2367, Melbourne, Australia, September 2013.

[25] Fu X., Huang Y., Zeng D., Zhang X. P. and Ding X., "A fusion-based enhancing approach for single sandstorm image", in Proceedings of 16^{th} IEEE International Workshop on Multimedia Signal Processing, pp. 1-5, Jakarta, Indonesia, September 2014.

[26] Gao Y., Yun L., Shi J., Chen F. and Lei L., "Enhancement MSRCR algorithm of color fog image based on the adaptive scale", in Proceedings of 6^{th} International Conference on Digital Image Processing, International Society for Optics and Photonics, Vol. 9159, pp. 91591B, April 2014.

[27] Gibson K., Vo D. and Nguyen T., "An investigation in dehazing compressed images and video", in Proceedings of OCEANS 2010 MTS/IEEE SEATTLE, pp. 1-8, Seattle, WA, USA, September 2010.

[28] Gibson K. B. and Nguyen T. Q., "On the effectiveness of the dark channel prior for single image dehazing by approximating with minimum volume ellipsoids", in Proceedings of IEEE International Conference on Acoustics, Speech and Signal Processing, pp. 1253-1256, Prague, Czech Republic, May 2011.

[29] Gibson K. B., Vo D. T. and Nguyen T. Q., "An investigation of dehazing effects on image and video coding", IEEE Transactions on Image Processing, Vol. 21, No. 2, pp. 662-673, 2012.

[30] Gibson K. B. and Nguyen T. Q., "Fast single image fog removal using the adaptive wiener filter", in Proceedings of 20^{th} IEEE International Conference on Image Processing, pp. 714-718, Melbourne, VIC, Australia, September 2013.

[31] Gonzalez R. C. and Woods R. E., "Digital image processing", Prentice hall Upper Saddle River, NJ, 2002.

[32] Guo F., Peng H. and Tang J., "A New Restoration Algorithm for Single Image Defogging", in Proceedings of Chinese Conference on Pattern Recognition, Springer, pp. 169-178, , Berlin, Heidelberg, November 2014.

[33] He K., Sun J. and Tang X., "Single image haze removal using dark channel prior", IEEE Transactions on Pattern Analysis and Machine Intelligence, Vol. 33, No. 12, pp. 2341-2353, 2011.

[34] He K., Sun J. and Tang X., "Guided image filtering", IEEE Transactions on Pattern Analysis and Machine Intelligence, Vol. 6, pp. 1397-1409, 2013.

[35] He K. and Sun J., "Fast guided filter", CoRR abs/1505.00996, pp. 1-2, 2015.

[36] He K., "$https://github.com/accessify/fast-guided-filter/blob/master/fastguidedfilter.m$", Fast Guided Filter, accessed January 5, 2018.

[37] Hasler D. and Suesstrunk S. E., "$https://gist.github.com/zabela/8539116$", accessed March 10, 2018.

[38] Hautière N., Tarel J. P., Aubert D. and Dumont E., "Blind contrast enhancement assessment by gradient ratioing at visible edges", Journal of Image Analysis and Stereology, Vol. 27, No. 2, pp. 87-95, 2011.

[39] Hautiere N., Tarel J. P., Aubert D. and Dumont E., "http://perso.lcpc.fr/tarel.jean-philippe/publis/iasj08.html", accessed February 10, 2018.

[40] Hu W. W., Wang R. G., Fang S. and HU Q., "Retinex algorithm for image enhancement based on bilateral filtering", Journal of Engineering Graphics, Vol. 2, pp. 104-109, 2010.

[41] Huang K. Q., Wang Q. and Wu Z. Y., "Natural color image enhancement and evaluation algorithm based on human visual system", Journal of Computer Vision and Image Understanding, Vol. 103, No. 1, pp. 52-63, 2006.

[42] Huang S. C., Chen B. H. and Wang W. J., "Visibility restoration of single hazy images captured in real-world weather conditions", IEEE Transactions on Circuits and Systems for Video Technology, Vol. 24, No. 10, pp. 1814-1824, 2014.

[43] Huang K. Q., Wang Q. and Wu Z. Y., "$http : //openimaj.org/apidocs/src - html/org/openimaj/image/feature/global/Naturalness.html$", accessed April 20, 2018.

[44] Hulburt E. O., "Optics of atmospheric haze", Journal of the Optical Society of America, Vol. 31, No. 7, pp. 467-476, 1941.

[45] Hurlbert A., "Formal connections between lightness algorithms", Journal of the Optical Society of America A, Vol. 3, No. 10, pp. 1684-1693, 1986.

[46] Im J., Yoo Y. and Paik J., "Single image-based spatially adaptive dynamic range extension using combined color-channels transmission map", International Journal for Light and Electron Optics, Vol. 126, No. 9-10, pp. 912-916, 2015.

[47] Jia J. and Yue H., "A wavelet-based approach to improve foggy image clarity", Journal of IFAC Proceedings Volumes, Vol. 47, No. 3, pp. 930-935, 2014.

[48] Jobson D. J. and Woodell G. A., "Properties of a center/surround Retinex: Part 2", Surround design. NASA Technical Memorandum, pp. 1-15, 1995.

[49] Jobson D. J., Rahman Z. U. and Woodell G. A., "Retinex image processing: Improved fidelity to direct visual observation", in Proceedings of 4^{th} Color and Imaging Conference, Society for Imaging Science and Technology, Vol. 1996, No. 1, pp. 124-125, January 1996.

[50] Jobson D. J., Rahman Z. U. and Woodell G. A., "Properties and performance of a center/surround retinex", IEEE Iransactions on Image Processing, Vol. 6, No. 3, pp. 451-462, 1997.

[51] Jobson D. J., Rahman Z. U. and Woodell G. A., "A multiscale retinex for bridging the gap between color images and the human observation of scenes", IEEE Transactions on Image Processing, Vol. 6, No. 7, pp. 965-976, 1997.

[52] Jobson D. J., Rahman Z. U., Woodell G. A. and Hines G. D., "A comparison of visual statistics for the image enhancement of foresite aerial images with those of major image classes", in Proceedings of Visual Information Processing XV, International Society for Optics and Photonics, Vol. 6246, pp. 624601/1-624601/8, Florida, United States, May 2006.

[53] John J. and Wilscy M., "Enhancement of weather degraded video sequences using wavelet fusion", in Proceedings of 7^{th} IEEE International Conference on Cybernetic Intelligent Systems, pp. 1-6, London, UK, September 2008.

[54] Moore A., Allman, J. and Goodman R. M., "A real-time neural system for color constancy", IEEE Transactions on Neural networks, Vol. 2, No. 2, pp. 237-247, 1991.

[55] Kansal I. and Kasana S. S., "Weighted image de-fogging using luminance dark prior", Journal of Modern Optics, Vol. 64, No. 19, pp. 2023-2034, 2017.

[56] Kansal I. and Kasana S. S., "Minimum preserving subsampling-based fast image de-fogging", Journal of Modern Optics, Vol. 65, No. 18, pp. 2103-2123, 2018.

[57] Kim T. K., Paik J. K. and Kang B. S., "Contrast enhancement system using spatially adaptive histogram equalization with temporal filtering", IEEE Transactions on Consumer Electronics, Vol. 44, No. 1, pp. 82-87, 1998.

[58] Kim J. Y., Kim L. S. and Hwang S. H., "An advanced contrast enhancement using partially overlapped sub-block histogram equalization", IEEE Transactions on Circuits and Systems for Video Technology, Vol. 11, No. 4, pp. 475-484, 2001.

[59] Kim M. and Chung M. G., "Recursively separated and weighted histogram equalization for brightness preservation and contrast enhancement", IEEE Transactions on Consumer Electronics, Vol. 54, No. 3, pp. 1389-1397, 2008.

[60] Kim J. H., Jang W. D., Sim J. Y. and Kim C. S., "Optimized contrast enhancement for real-time image and video dehazing", Journal of Visual Communication and Image Representation, Vol. 24, No. 3, pp. 410-425, 2013.

[61] Kim Y. M., Park K. T., Lee D. S., Choi W. and Moon Y. S., "Video dehazing without flicker artifacts using adaptive temporal average", in Proceedings of 18^{th} IEEE International Symposium on Consumer Electronics, pp. 1-2, JeJu Island, South Korea, June 2014.

[62] Kingsbury N., "The dual-tree complex wavelet transform: a new efficient tool for image restoration and enhancement", in Proceedings of 9^{th} European IEEE Signal Processing Conference, pp. 1-4, Rhodes, Greece, September 1998.

[63] Kingsbury N., "A dual-tree complex wavelet transform with improved orthogonality and symmetry properties", in Proceedings of International Conference on Image Processing, Vol. 2, pp. 375-378, Vancouver, BC, Canada, September 2000.

[64] Kou F., Chen W., Wen C. and Li Z., "Gradient domain guided image filtering", IEEE Transactions on Image Processing, Vol. 24, No. 11, pp. 4528-4539, 2015.

[65] Kratz L. and Nishino K., "Factorizing scene albedo and depth from a single foggy image", in Proceedings of 12^{th} IEEE International Conference on Computer Vision, pp. 1701-1708, Kyoto, Japan, September 2009.

[66] Kumar A., Chourasia B. and Kurmi Y., "Image defogging by multiscale depth fusion and hybrid scattering model", International Journal of Computer Applications, Vol. 155, No. 11, pp. 34-38, 2016.

[67] Land E. H. and McCann J. J., "Lightness and retinex theory", Journal of the Optical Society of America, Vol. 61, No. 1, pp. 1-11, 1971.

[68] Land E. H., "Recent advances in retinex theory and some implications for cortical computations: color vision and the natural image", in Proceedings of National Academy of Sciences of the United States of America, Vol. 80, No. 16, pp. 5163-5170, 1983.

[69] Lee Y., Gibson K. B., Lee Z. and Nguyen T. Q., "Stereo image defogging", in Proceedings of IEEE International Conference on Image Processing, pp. 5427-5431, Paris, France, October 2014.

[70] Lee S., Yun S., Nam J. H., Won C. S. and Jung S. W., "A review on dark channel prior based image dehazing algorithms", EURASIP Journal on Image and Video Processing, Vol. 2016, No. 1, pp. 1-24, 2016.

[71] Li Y., You S., Brown M. S. and Tan R. T., "Haze visibility enhancement: A survey and quantitative benchmarking", Journal of Computer Vision and Image Understanding, Vol. 165, pp. 1-16, 2017.

[72] Lin Z. and Wang X., "Dehazing for image and video using guided filter", Open Journal of Applied Sciences, Vol. 2, No. 4B, pp. 123-127, 2012.

[73] Liu X., Zhang H., Cheung Y. M., You X. and Tang Y. Y., "Efficient single image dehazing and denoising: An efficient multi-scale correlated wavelet approach", Journal of Computer Vision and Image Understanding, Vol. 162, pp. 23-33, 2017.

[74] Ma K., Liu W. and Wang Z., "$http://ivc.uwaterloo.ca/database/Dehaze/$", IVC Dehazing Dataset, accessed January 5, 2018.

[75] Maheshwari S, Heda S., "A Review on Crowd Behavior Analysis Methods for Video Surveillance", IEEE International Conference on second International Conference on Information and Communication Technology for Competitive Strategies, pp. 1-5, March 2016.

[76] McCann J., "Lessons learned from mondrians applied to real images and color gamuts", in Proceedings of Color and Imaging Conference, Society for Imaging Science and Technology, Vol. 1999, No. 1, pp. 1-8, Janauary 1999.

[77] McCartney E. J., "Optics of the atmosphere: scattering by molecules and particles", New York, John Wiley and Sons, Inc. 421, 1976.

[78] Minnaert M. G. J., "The Nature of Light and Colour in the Open Air Courier", Corporation, 2013.

[79] Meng G., Wang Y., Duan J., Xiang S. and Pan C., " Efficient image dehazing with boundary constraint and contextual regularization", in Proceedings of IEEE International Conference on Computer Vision, pp. 617-624, 2013.

[80] Nandal S. and Kumar S., "Single image fog removal algorithm in spatial domain using fractional order anisotropic diffusion", Journal of Multimedia Tools and Applications, Vol. 78, pp. 10717-10732. 2018.

[81] Narasimhan S. G. and Nayar S. K., "Chromatic framework for vision in bad weather", in Proceedings of IEEE Conference on Computer Vision and Pattern Recognition, Vol. 1, pp. 598-605, 2000.

[82] Narasimhan S. G. and Nayar S. K., "Removing weather effects from monochrome images", in Proceedings of IEEE Computer Society Conference on Computer Vision and Pattern Recognition, Vol. 2, pp. II-II, 2001.

[83] Narasimhan S. G. and Nayar S. K., "Vision and the atmosphere", Journal of Computer Vision, Vol. 48, No. 3, pp. 233-254, 2002.

[84] Narasimhan S. G., Wang C. and Nayar S. K., "All the images of an outdoor scene", in Proceedings of Springer European conference on Computer Vision, pp. 148-162, Berlin, Heidelberg, May 2002.

[85] Narasimhan S. G. and Nayar S. K., "Contrast restoration of weather degraded images", IEEE transactions on Pattern Analysis and Machine Intelligence, Vol. 25, No. 6, pp. 713-724, 2003.

[86] Narasimhan S. G. and Nayar S. K., "Interactive (de) weathering of an image using physical models", in Proceedings of IEEE Workshop on Color and Photometric Methods in Computer Vision, Vol. 6, No. 6.4, pp. 1-8, France, October 2003.

[87] Nayar S. K. and Narasimhan S. G., "Vision in bad weather", in Proceedings of 7^{th} IEEE International Conference on Computer Vision, Vol. 2, pp. 820-827, Kerkyra, Greece, Greece, September 1999.

[88] Nishino K., Kratz L. and Lombardi S., "Bayesian defogging", International Journal of Computer Vision, Vol. 98, No. 3, pp. 263-278.

[89] Nousheen S. and Kumar S. P., “Novel fog-removing method for the traffic monitoring image”, International Journal of Innovative Technology and Research, Vol. 4, No. 5, pp. 4159-4162, 2016.

[90] Otsu N., “A threshold selection method from gray-level histograms”, IEEE Transactions on Systems, Man, and Cybernetics, Vol. 9, No. 1, pp. 62-66, 1979.

[91] Parthasarathy S. and Sankaran P., “A RETINEX based haze removal method”, in Proceedings of 7^{th} IEEE International Conference on Industrial and Information Systems, pp. 1-6, Chennai, India, August 2012.

[92] Pal C., Chakrabarti A. and Ghosh R., “A brief survey of recent edge-preserving smoothing algorithms on digital images”, arXiv preprint arXiv:1503.07297. 2015.

[93] Pei S. C. and Lee T. Y., “Nighttime haze removal using color transfer pre-processing and dark channel prior”, in Proceedings of 19^{th} IEEE International Conference on Image Processing, pp. 957-960, Orlando, FL, USA, September 2012.

[94] Petro A. B., Sbert C. and Morel J. M., “Multiscale retinex”, Journal of Image Processing On Line, pp. 71-88, 2014.

[95] Radke R. J., Andra S., Al-Kofahi O. and Roysam B., “Image change detection algorithms: a systematic survey”, IEEE Transactions on Image Processing, Vol. 14, No. 3, pp. 294-307, 2005.

[96] Radwan N. I., Salem N. M. and El Adawy M. I., “Histogram correlation for video scene change detection”, in Advances in Computer Science, Engineering and Applications, Springer, pp. 765-773, Berlin, Heidelberg. 2012.

[97] Rahman Z. U., Jobson D. J. and Woodell G. A., “Multiscale retinex for color rendition and dynamic range compression”, In Applications of Digital Image Processing XIX, International Society for Optics and Photonics, Vol. 2847, pp. 183-192, November 1996.

[98] Rahman Z. U., Jobson D. J. and Woodell G. A., “Retinex processing for automatic image enhancement”, Journal of Electronic Imaging, Vol. 13, No. 1, pp. 100-111, 2004.

[99] Rahman Z. U., Jobson D. J., Woodell G. A. and Hines G. D., “Automated, on-board terrain analysis for precision landings”, in Proceedings of SPIE 6246, Visual Information Processing XV, 62460J (12 May 2006); doi: 10.1117/12.664605.

[100] Ramya C. and Rani D. S. S., “Contrast enhancement for fog degraded video sequences using BPDFHE”, International Journal of Computer Science and Information Technologies, Vol. 3, No. 2, pp. 3463-3468, 2012.

[101] Rajput G. S. and Rahman Z. U., “Hazard detection on runways using image processing techniques”, in Enhanced and Synthetic Vision 2008, International Society for Optics and Photonics, Vol. 6957, pp. 69570D/1-69570D/12, 2008.

[102] Ren W., Liu S., Zhang H., Pan J., Cao X. and Yang M. H., "Single image dehazing via multi-scale convolutional neural networks", in Proceedings of European Conference on Computer Vision, Springer, pp. 154-169, October 2016.

[103] Rong Z. and Jun W. L., "Improved wavelet transform algorithm for single image dehazing", International Journal for Light and Electron Optics, Vol. 125, No. 13, pp. 3064-3066, 2014.

[104] Salazar-Colores S., Cruz-Aceves I. and Ramos-Arreguin J. M., "Single image dehazing using a multilayer perceptron", Journal of Electronic Imaging, Vol. 27, No. 4, pp. 043022, 2018.

[105] Schaul L., Fredembach C. and Süsstrunk S., "Color image dehazing using the near-infrared", in Proceedings of IEEE International Conference on Image Processing, No. LCAV-CONF-2009-026, Cairo, Egypt, pp. 1629-1632, November 2009.

[106] Schechner Y. Y., Narasimhan S. G. and Nayar S. K., "Instant dehazing of images using polarization", in Proceedings of IEEE Conference on Computer Vision and Pattern Recognition, Vol. 1, pp. 325-332, December 2001.

[107] Seow M. J. and Asari V. K., "Ratio rule and homomorphic filter for enhancement of digital colour image", Journal of Neurocomputing, Vol. 69, No. 7-9, pp. 954-958, 2006.

[108] Shi Z., Zhu M., Xia Z. and Zhao M., "Fast single-image dehazing method based on luminance dark prior", International Journal of Pattern Recognition and Artificial Intelligence, Vol. 31, No. 2, pp. 1754003, 2017.

[109] Shiau Y. H., Chen P. Y., Yang H. Y., Chen C. H. and Wang S. S., "Weighted haze removal method with halo prevention", Journal of Visual Communication and Image Representation, Vol. 25, No. 2, pp. 445-453, 2014.

[110] Shwartz S., Namer E. and Schechner Y. Y., "Blind haze separation", in Proceedings of IEEE Computer Society Conference on Computer Vision and Pattern Recognition, Vol. 2, pp. 1984-1991, New York, NY, USA, USA, pp. 1984-1991, June 2006.

[111] Sun W., Han L., Guo B., Jia W. and Sun M., "A fast color image enhancement algorithm based on Max Intensity Channel", Journal of Modern Optics, Vol. 61, No. 6, pp. 466-477, 2014.

[112] Tan R. T., "Visibility in bad weather from a single image", in Proceedings of IEEE Conference on Computer Vision and Pattern Recognition, pp. 1-8, 2008.

[113] Tang K., Yang J. and Wang J., "Investigating haze-relevant features in a learning framework for image dehazing", in Proceedings of IEEE Conference on Computer Vision and Pattern Recognition, pp. 2995-3000, Columbus, OH, USA, June 2014.

[114] Tarel J. P. and Hautiere N., "Fast visibility restoration from a single color or gray level image", in Proceedings of 12^{th} IEEE International Conference on Computer Vision, Kyoto, Japan, pp. 2201-2208, September 2009.

[115] Tarel J. P., Hautiere N., Cord A., Gruyer D. and Halmaoui H., "$http : //www.sciweavers.org/read/frida - foggy - road - image - database - evaluation - database - for - visibility - restoration - algorithms - 184350$", Foggy Road Image Database, accessed April 3, 2018.

[116] Treibitz T. and Schechner Y. Y., "Polarization: Beneficial for visibility enhancement", in Proceedings of IEEE Conference on Computer Vision and Pattern Recognition, pp. 525-532, Miami, FL, USA, June 2009.

[117] Wang Z., Bovik A. C., Sheikh H. R. and Simoncelli E. P., "Image quality assessment: from error visibility to structural similarity", IEEE Transactions on Image Processing, Vol. 13, No. 4, pp. 600-612, 2004.

[118] Wang M. and Zhou S. D., "The study of color image defogging based on wavelet transform and single scale retinex", in Proceedings of International Symposium on Photoelectronic Detection and Imaging, Vol. 8194, pp. 81940F, August 2011.

[119] Wang Y. K. and Fan C. T., "Single image defogging by multiscale depth fusion", IEEE Transactions on Image Processing, Vol. 23, No. 11, pp. 4826-4837, 2014.

[120] Wang Z. and Feng Y., "Fast single haze image enhancement", Journal of Computers and electrical engineering, Vol. 40, No. 3, pp. 785-795, 2014.

[121] Wang S., Lu S., Dong Z., Yang J., Yang M. and Zhang Y., "Dual-tree complex wavelet transform and twin support vector machine for pathological brain detection", Journal of Applied Sciences, Vol. 6, No. 6, pp. 1-18, 2016.

[122] Wanting Y., Ronggui W., Shuai F. and Xuan Z., "Variable filter Retinex algorithm for foggy image enhancement", Journal of Computer-Aided Design and Computer Graphics, Vol. 6, No. 10, pp. 965-971, 2010.

[123] Xiao C. and Gan J., "Fast image dehazing using guided joint bilateral filter", Journal of The Visual Computer, Vol. 28, No. 6-8, pp. 713-721, 2012.

[124] Xie B., Guo F. and Cai Z., "Improved single image dehazing using dark channel prior and multi-scale retinex", in Proceedings of International Conference on Intelligent System Design and Engineering Application, Vol. 1, pp. 848-851, Changsha, Hunan China, October 2010.

[125] Xie B., Guo F. and Cai Z., "Universal strategy for surveillance video defogging", Journal of Optical Engineering, Vol. 51, No. 10, pp. 1-8, 2012.

[126] Xu Z., Liu X. and Chen X., "Fog removal from video sequences using contrast limited adaptive histogram equalization", in Proceedings of International Conference on Computational Intelligence and Software Engineering, pp. 1-4, Wuhan, China, December 2009.

[127] Xu Y., Wen J., Fei L. and Zhang Z., "Review of video and image defogging algorithms and related studies on image restoration and enhancement", Journal of IEEE Access, Vol. 4, pp. 165-188, 2016.

[128] Xu Y., Wen J., Fei L. and Zhang Z., "$http://www.yongxu.org/lunwen.html$", , accessed May 15, 2018.

[129] Yang D. and Sun J., "Proximal Dehaze-Net: A Prior Learning-Based Deep Network for Single Image Dehazing", in Proceedings of European Conference on Computer Vision, pp. 702-717, September 2018.

[130] Yadav R. and Alwani M., "Enhancement of fog degraded images on the basis of histogram classification", in Proceedings of the 14^{th} WSEAS International Conference on Computers, World Scientific and Engineering Academy and Society, pp. 549-554, 2010.

[131] Yoon I., Kim S., Kim D., Hayes M.H. and Paik J., "Adaptive defogging with color correction in the HSV color space for consumer surveillance system", IEEE Transactions on Consumer Electronics, Vol. 58, No. 1, pp. 111-116, 2012.

[132] Yu J., Xiao C. and Li D., "Physics-based fast single image fog removal", in Proceedings of 10^{th} International Conference on Signal Processing, pp. 1048-1052, Beijing, China, October 2010.

[133] Zhang J., Li L., Zhang Y., Yang G., Cao X. and Sun J., "Video dehazing with spatial and temporal coherence", Journal of The Visual Computer, Vol. 27, No. 6-8, pp. 749-757, 2011.

[134] Zhao X., Wang R. and Qiu Y., "An enhancement method of fog-degraded images", in Proceedings of 2^{nd} International Conference on Digital Image Processing, International Society for Optics and Photonics, Vol. 7546, pp. 75461S, February 2010 .

[135] Zhongli M. and Jie W., "Single-scale Retinex sea fog removal algo-rithm fused the edge information", Journal of Computer-Aided Design and Computer Graphics, Vol. 27, No. 2, pp. 217-225, 2015.

[136] Zhu Q., Mai J. and Shao L., "A Fast Single Image Haze Removal Algorithm Using Color Attenuation Prior", IEEE Transactions on Image Processing, Vol. 24, No. 11, pp. 3522-3533, 2015.

[137] Zuiderveld K., "Contrast limited adaptive histogram equalization", Journal of Graphics Gems, pp. 474-485, 1994.